

Electronic magnetism and magnetic shielding in metal-organic frameworks

D I S S E R T A T I O N

zur Erlangung des akademischen Grades

Doctor rerum naturalium

(Dr. rer. nat.)

vorgelegt

der Fakultät Mathematik und Naturwissenschaften
der Technischen Universität Dresden

von

M. Sc. Kai Trepte

geboren am 08.09.1987 in Plauen.

Eingereicht am



**TECHNISCHE
UNIVERSITÄT
DRESDEN**

Faculty of Mathematics and Natural Sciences Department of Chemistry and Food Chemistry
Institute for Physical Chemistry, Chair for Theoretical Chemistry

ELECTRONIC MAGNETISM AND MAGNETIC SHIELDING IN METAL-ORGANIC FRAMEWORKS

Kai Trepte

DISSERTATION

to achieve the academic degree

DOCTOR RERUM NATURALIUM (DR. RER. NAT.)

Submitted on:

CONTENTS

I. Introduction	7
II. Theoretical background	12
2.1. Density functional theory (DFT)	15
2.2. Current density and magnetic shielding	17
2.3. Exchange-correlation functionals	20
2.4. Basis sets and pseudopotentials	21
2.5. Electronic magnetism	25
2.5.1. Heisenberg-Dirac-Van Vleck Hamiltonian	25
2.5.2. Exchange mechanisms	29
2.6. Magnetic shielding	32
2.6.1. Basics of nuclear magnetic resonance (NMR)	32
2.6.2. Chemical shift	33
2.7. Computational details	35
III. Electronic magnetism in DUT-8(Ni)	36
3.1. Structural considerations	37
3.2. Electronic structure - Density of states	38
3.3. Magnetic ground state investigations	40
3.4. Supercell calculations	42
3.5. Model systems	44
3.5.1. Influence of chemical environments on J_{ij}	46
3.5.2. Influence of defects on J_{ij}	51
3.5.3. Influence of long-range magnetic interactions on J_{ij}	53
IV. Magnetic shielding of ^{129}Xe in UiO-66/UiO-67	57
4.1. Structural considerations	58
4.2. ^1H and ^{13}C NMR investigations	59
4.3. Model systems	60
4.3.1. ^{129}Xe reference δ_0	60
4.3.2. Influence of Xe-Xe interactions $\delta_{\text{Xe-Xe}}$	62
4.3.3. Influence of Xe-surface interactions δ_{S}	65
4.4. Chemical shift of Xe in UiO-66 and UiO-67	69
V. Conclusion and Outlook	76
VI. Appendices	80
Bibliography	120

ABBREVIATIONS, UNITS AND CONSTANTS

r	used vector notation, here \vec{r}
AFM	antiferromagnetic
a.u.	arbitrary units
c	speed of light in vacuum
DFT	density functional theory
DOS	density of states
DUT	Dresden University of Technology
ϵ_F	Fermi energy
E_g	band gap
E_{tot}	total energy
ELF	electron localization function
FM	ferromagnetic
GGA	generalized gradient approximation
HOMO	highest occupied molecular orbital
HS	high-spin state
LS	low-spin state
LSDA	local spin density approximation
LUMO	lowest unoccupied molecular orbital
M_{abs}	absolute magnetization
M_{tot}	total magnetization
MOF	metal-organic framework
PBE	Perdew-Burke-Ernzerhof (GGA) [1]
PDOS	partial density of states
SBU	secondary building unit
UiO	University of Oslo
vc	structure obtained from variable cell optimization
vdW	van der Waals correction (by Grimme [2])

\AA 1 Angström = 0.1 nm = 10^{-10} m

QE Quantum ESPRESSO [3]
 FPLO Full-potential local-orbital minimum-basis code [4]

Unit conversion factors.

	eV	Ry	Ha	cm^{-1}	K	J
eV	1	0.074	0.037	8064.896	11600.659	$1.602 \cdot 10^{-19}$
Ry	13.606	1	0.500	109782.554	157835.085	$2.179 \cdot 10^{-18}$
Ha	27.211	2	1	219484.319	315670.169	$4.359 \cdot 10^{-18}$
cm^{-1}	$1.239 \cdot 10^{-4}$	$9.109 \cdot 10^{-6}$	$4.556 \cdot 10^{-6}$	1	1.438	$1.987 \cdot 10^{-23}$
K	$8.620 \cdot 10^{-5}$	$6.336 \cdot 10^{-6}$	$3.168 \cdot 10^{-6}$	0.695	1	$1.381 \cdot 10^{-23}$
J	$6.241 \cdot 10^{18}$	$4.587 \cdot 10^{17}$	$2.294 \cdot 10^{17}$	$5.034 \cdot 10^{22}$	$7.241 \cdot 10^{22}$	1

Electronic configurations of specific elements which were used within this thesis.

${}^1_1\text{H}$	Hydrogen	$1s^1$
${}^{12}_6\text{C}$	Carbon	$[\text{He}] 2s^2 2p^2$
${}^{14}_7\text{N}$	Nitrogen	$[\text{He}] 2s^2 2p^3$
${}^{16}_8\text{O}$	Oxygen	$[\text{He}] 2s^2 2p^4$
${}^{56}_{26}\text{Fe}$	Iron	$[\text{Ar}] 4s^2 3d^6$
${}^{59}_{27}\text{Co}$	Cobalt	$[\text{Ar}] 4s^2 3d^7$
${}^{58}_{28}\text{Ni}$	Nickel	$[\text{Ar}] 4s^2 3d^8$
${}^{63}_{29}\text{Cu}$	Copper	$[\text{Ar}] 3d^{10} 4s^1$
${}^{91}_{40}\text{Zr}$	Zirconium	$[\text{Kr}] 4d^2 5s^2$
${}^{129}_{54}\text{Xe}$	Xenon	$[\text{Kr}] 4d^{10} 5s^2 5p^6$

Relevant constants.

π	3.14159265358979323846	
ϵ_0	$8.854187817 \cdot 10^{-12}$	$\frac{\text{A}^2\text{s}^4}{\text{kgm}^3}$
μ_0	$1.256637061 \cdot 10^{-6}$	$\frac{\text{Vs}}{\text{Am}}$
e	$1.602176621 \cdot 10^{-19}$	As
h	$6.626070041 \cdot 10^{-34}$	$\frac{\text{kgm}^2}{\text{s}}$
\hbar	$1.054571800 \cdot 10^{-34}$	$\frac{\text{kgm}^2}{\text{s}}$
c	299792458	$\frac{\text{m}}{\text{s}}$



PART I.

INTRODUCTION

The class of metal-organic frameworks (MOFs) is in the focus of many research fields. This interest stems from the highly porous, crystalline nature of MOFs, making them ideal for e.g. gas adsorption and gas storage applications. As their name indicates, MOFs consist of metal clusters, which usually contain transition metals. These metal clusters are called secondary building units (SBUs). They are interconnected with a specific set or sets of organic linkers to generate three dimensional networks [5, 6, 7].

These linkers are rather large in comparison to the size of the SBU, creating a significant separation of the metal clusters. This leads to large pores and high porosities. Given these facts, the potential applications of MOFs are mainly based on their resulting large pore volumes and surface areas [8, 9]. Application fields include gas adsorption [8, 9, 7], gas storage [10], adsorption based gas/vapor separation [11] and the possibility for spintronic devices based on intrinsic magnetic properties [12, 13].

Due to the fact that the SBUs contain transition metals, a certain number of unpaired electrons per metal ion can occur. This gives rise to a magnetic coupling between them. In this context, Ni^{2+} complexes have been studied in the last years [14, 15], even with respect to molecular magnetism [16, 17]. A combination of molecular magnetism with MOFs can open new possibilities in their application, considering a localized magnetic structure repeating itself in three dimensions [12, 13].

Furthermore, MOFs influence intrinsic properties of adsorbed species/molecules, like the magnetic shielding, which can be calculated by theoretical methods [18, 19, 20]. Changes in the magnetic shielding are referred to as chemical shift. This quantity can be correlated to the structure of the MOFs, because different structural elements will influence the magnetic shielding differently. Furthermore, the large pores of MOFs allow several species to be adsorbed. This leads to a change in the magnetic shielding due to interactions with the surface of the MOF as well as interactions with other adsorbed species. Therefore, a full analysis of the effects of the surface and adjacent molecules on such properties can provide a thorough understanding of the magnetic shielding inside a porous material [21].

Carrying out theoretical investigations by taking into account the atomic structure of a material (e.g. MOFs) can fundamentally provide information about its properties. Using theoretical methods enables to describe these properties from an experiment-independent point of view. Applying state-of-the-art density functional theory (DFT) [22, 23] to a given problem can help to understand measured phenomena. This can further provide an explanation for trends of physical properties which might be inaccessible from experiments.

Additionally, DFT can be employed to predict new and previously unknown properties of a system. These predictions might include the determination of the geometrical structure, the calculation of electronic and magnetic properties (like the spin-spin coupling between two magnetic centers) as well as the evaluation of the magnetic shielding and the resulting chemical shift, making the theoretical predictions comparable to measurements.

Within this thesis, DFT is used on the one hand to describe the electronic magnetism as an intrinsic property of the MOF DUT-8(Ni) (DUT – Dresden University of Technology) and on the other hand to analyze the magnetic shielding of adsorbed Xe atoms inside the MOFs UiO-66 and UiO-67 (UiO – University of Oslo).

DUT-8(Ni) The first part of this thesis is concerned with the magnetic ground state of the MOF DUT-8(Ni). As it remains unclear from the experimental side, an analysis of the intrinsic magnetic properties has been carried out.

Because this MOF exists in two structures (DUT-8(Ni)_{open} and DUT-8(Ni)_{closed}), a subsequent question occurs, i.e. whether the magnetic ground state changes when this phase transition takes place. Based on these initial results, another question arises.

Considering the secondary building units of the MOF (Ni dimers), influences of their chemical environment might play a crucial role in the formation of the magnetic ground state. Thus, alterations of the chemical environment have been implied to analyze their influence on the magnetic behavior. Further, variations of the magnetic ground state due to a metal exchange might induce a different magnetic ground state as well. Consequently, exchanges of metal centers within the MOF were investigated.

As a condition for the theoretical investigation, it is mandatory that the magnetism is localized on the SBUs. This is important because magnetic interactions between SBUs could affect the magnetic ordering within the periodic structure. Thus, it was analyzed how different SBUs interact magnetically.

The metal-organic framework DUT-8(Ni) is a so-called flexible MOF [24, 25, 26, 27], thus it can exist in two different crystal structures (DUT-8(Ni)_{open} and DUT-8(Ni)_{closed}). It is generated by Ni dimer SBUs, which are connected along one direction with the linker shown in figure 1.1 (a) (dabco unit) and along the other two directions with a second type of linker displayed in figure 1.1 (b) (acidic linker). This interconnection creates the two different three-dimensional framework (DUT-8(Ni)_{open}, see figure 1.2 (a,b) and DUT-8(Ni)_{closed}, see figure 1.2 (c)-(e)).

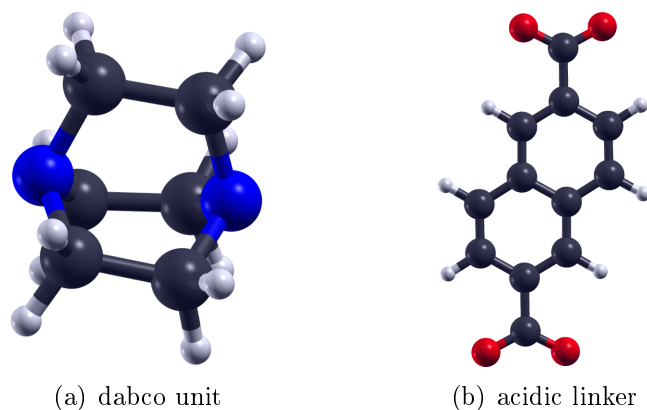


Figure 1.1.: The organic building blocks of DUT-8(Ni). In (a) the dabco unit is shown while in (b) the acidic linker is displayed.

The color code is: H - white, C - dark gray, N - blue, O - red.

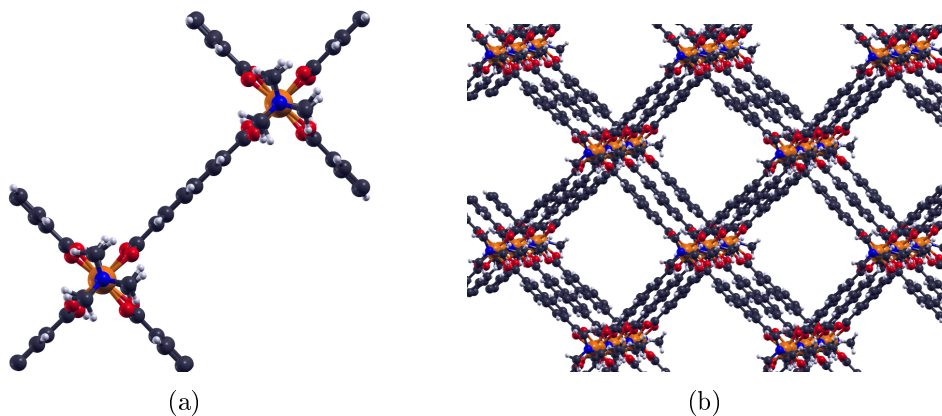


Figure 1.2.: The crystal structure of DUT-8(Ni)_{open} (along **c**) is shown in (a). A slightly tilted view is presented in (b) to visualize the porosity of the system. In addition to the color code of figure 1.1, Ni is orange.

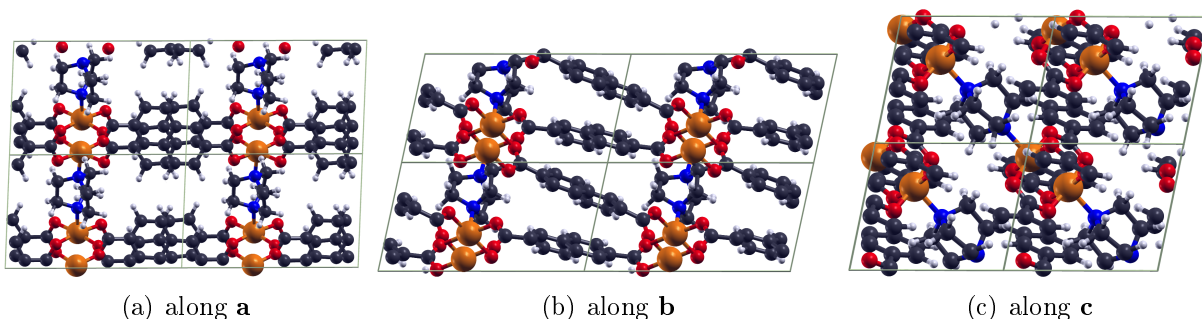


Figure 1.3.: Crystal structure of DUT-8(Ni)_{closed} (along its crystallographic directions).

UiO-66 and UiO-67 For the second part of this thesis, a theoretical analysis of the magnetic shielding of Xe within the MOFs UiO-66 and UiO-67 was carried out. This investigation is based on measurements, which revealed a decrease of the ^{129}Xe chemical shift from the smaller (UiO-66) to the larger (UiO-67) structure. To explain this decrease at an atomistic level, theoretical investigations have been performed. With that, influences on the chemical shift were analyzed in detail. A thorough theoretical analysis allows an individual treatment of different contributions to the chemical shift. These contributions include Xe-Xe as well as Xe-surface interactions.

From the theoretical analysis, the chemical shift within the different pores of the two MOFs can be investigated individually. This allows a description of the total chemical shift as obtained in experiments. Thus, with the theoretical approach an explanation of the observed behavior has been carried out at an atomistic level, which is inaccessible from measurements.

The isostructural MOFs UiO-66 and UiO-67 are found in face-centered-cubic (fcc) lattices, with a space group of $F\bar{4}3m$ for UiO-66 and $F23$ for UiO-67 [28, 29, 30]. Both MOFs have the same SBU (a $\text{Zr}_6\text{O}_4(\text{OH})_4^{12+}$ cluster, see figure 1.4 (a)). The connections between the Zr atoms are characterized as $\mu_3\text{-O}$, where three Zr atoms are connected with an oxygen atom and $\mu_3\text{-OH}$, where three Zr atoms are connected with a single hydroxy group. Such SBUs are interconnected with twelve organic linkers, see figure 1.4 (b) and (c).

Given this interconnection, two types of pores are formed, namely octahedral (O_p) and tetrahedral (T_p) ones. There are two kinds of T_p pores, which for further investigations are denoted as $T_{p,1}$ and $T_{p,2}$. The difference between them is the composition of their corners. In the $T_{p,1}$ pore, the corners are generated by a $\mu_3\text{-O}$ of the SBU while in the $T_{p,2}$ pore it is a $\mu_3\text{-OH}$. Even though this difference is rather small and could usually be neglected, the influence of those corners on the ^{129}Xe chemical shift may significantly differ. Consequently, they have to be distinguished¹. Furthermore, the difference between the two MOFs is the length of their organic linkers, which increases from UiO-66 to UiO-67 due to an additional carbon ring (see figure 1.4 (b) and (c) as well as figure 1.5).

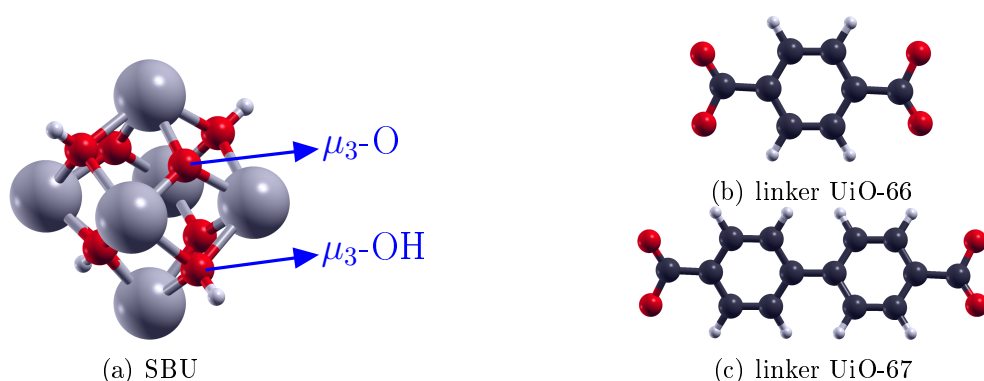


Figure 1.4.: SBU of both MOFs, a $\text{Zr}_6\text{O}_4(\text{OH})_4^{12+}$ cluster. Further, the organic linkers for UiO-66 and UiO-67 are displayed.

The color code is: H - white, O - red, C - dark gray, Zr - gray.

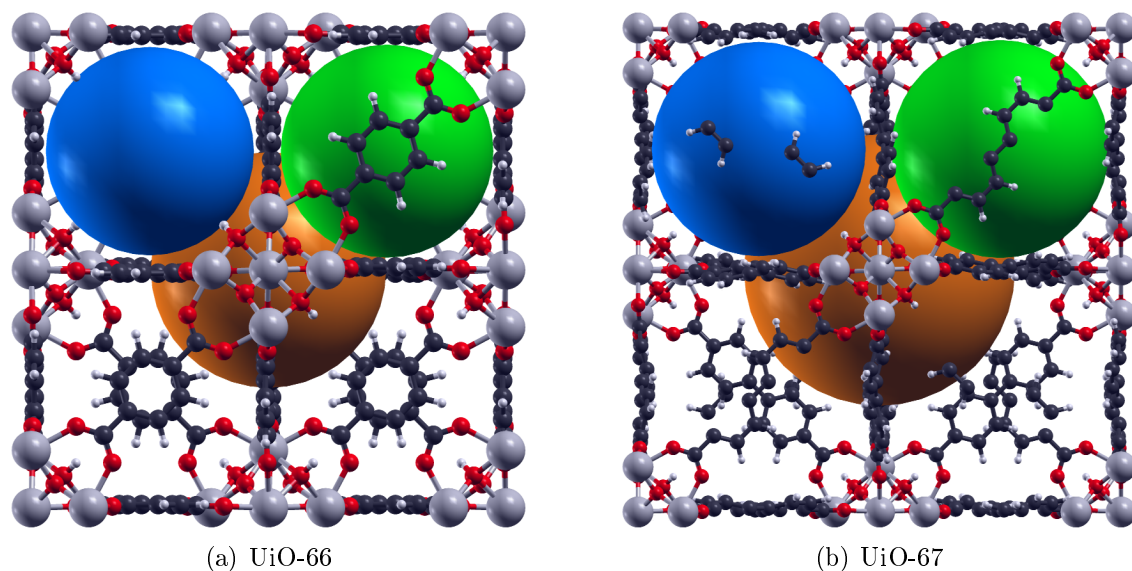


Figure 1.5.: Crystal structures of UiO-66 and UiO-67. Additionally, the pores are visualized by colored spheres, where orange stands for the O_p pore, green for the $T_{p,1}$ pore and blue for the $T_{p,2}$ pore. Both structures are scaled differently such that the pores appear to have the same size.

¹Further visualization can be found in Appendix 1, where the pores in UiO-67 are displayed.



PART II.

THEORETICAL BACKGROUND

Quantum mechanics enables an accurate description of any system which cannot be provided by classical physics. For example, properties of atoms cannot be explained by classical physics, but only by the concepts of quantum theory. Additionally, observations from e.g. the double slit experiment contradicted common sense. Electrons interfere with each other and with themselves like waves, although they were believed to be particles. Furthermore, in case an observer wants to determine through which slit a single electron moves, the interference pattern was lost and only a double slit pattern emerges. Thus, the measurement itself disturbs the properties of the electron. The corresponding wave function 'collapses' to give one, distinct value.

Further, as shown by the Bohr- van Leeuwen theorem, magnetism is a property which cannot be described with classical physics, as it is only possible to explain this phenomenon with quantum mechanics. From a classical physics point of view, the thermal average of the magnetization is always zero. Consequently, quantum mechanics can explain this behavior by the introduction of the electron spin. Another famous example is the photoelectric effect, for which Albert Einstein was awarded the Nobel prize. The consensus of this theoretical description is that quantum objects behave like particles and waves simultaneously (particle-wave duality).

Max Planck introduced the quantization of energy, such that every energy which is emitted or absorbed has a minimum value $h\nu$, explaining for example the spectrum of black-body radiation.

Another theoretical concept was proposed by Niels Bohr, the so-called Copenhagen interpretation of quantum theory, which is nowadays the most common interpretation of quantum mechanics. It was famously described by the gedankenexperiment 'Schrödinger's cat'. This interpretation states that a system, described by a wave function, does not have definite properties until it is being measured. The measurement itself disturbs the system, resulting in a 'collapse' of the wave function which generates one discrete value for a specific property. However, without the measurement there are various possibilities for different final values of each physical property, each having a certain probability. Further, this interpretation includes Heisenberg's uncertainty principle, stating that certain properties cannot be known precisely for the same system at the same time.

With that, quantum mechanics is an important research field which has been developed for more than 100 years. In the following, the well known Schrödinger equation, as proposed in 1926 by Erwin Schrödinger, shall be discussed further. To get an exact description of a quantum mechanical problem, the time-dependent Schrödinger equation has to be solved

$$\hat{H}\Psi(\mathbf{r}, t) = i\hbar \frac{\partial}{\partial t} \Psi(\mathbf{r}, t), \quad (2.1)$$

with \hat{H} being the Hamiltonian, $\Psi(\mathbf{r}, t)$ being the time- and space-dependent wave function, \hbar being the reduced Planck constant and i being the imaginary unit. If only static solutions are of interest, the time-independent Schrödinger equation can be used instead [31]

$$\hat{H}\Psi(\mathbf{r}) = \epsilon\Psi(\mathbf{r}), \quad (2.2)$$

where ϵ is the energy eigenvalue of the time-independent wave function $\Psi(\mathbf{r})$.

The Hamiltonian \hat{H} contains the kinetic energy operator \hat{T} and the potential energy operator \hat{V} . Considering a system of electrons and nuclei, the kinetic energy operator \hat{T} can be expressed as

$$\hat{T} = \sum_i \frac{\hat{p}_i^2}{2m_i} + \sum_I \frac{\hat{p}_I^2}{2m_I} \quad (2.3)$$

$$\text{with } \hat{p}_{i/I} = -i\hbar \nabla_{i/I}. \quad (2.4)$$

Here, $\hat{p}_{i/I}$ are the momentum operators for the electrons and the nuclei, respectively. The variables i and I are running over the number of electrons and nuclei, $m_i = m_e$ and m_I are the masses of the electron and the nuclei of species I while ∇ denotes the Nabla operator.

The Born-Oppenheimer (BO) approximation [32] allows to separate the electronic and the nuclear degrees of freedom. This approximation uses the fact that the nuclei are static with respect to the electrons, as they are much heavier ($m_{\text{proton}} \approx 1836 m_e$). With that, the electrons are always in their ground state as they can follow changes in the nuclear motion almost instantaneously. The BO approximation leads to the cancellation of the kinetic energy of the nuclei in equation (2.3). Taking a look at the potential energy on the other hand gives

$$\hat{V} = \underbrace{-\frac{e^2}{4\pi\epsilon_0} \sum_{i,I} \frac{Z_I}{|\mathbf{r}_i - \mathbf{R}_I|}}_{\text{electron-nuclear}} + \underbrace{\frac{1}{2} \frac{e^2}{4\pi\epsilon_0} \sum_{i \neq j} \frac{1}{|\mathbf{r}_i - \mathbf{r}_j|}}_{\text{electron-electron}} + \underbrace{\frac{1}{2} \frac{e^2}{4\pi\epsilon_0} \sum_{I \neq J} \frac{Z_I Z_J}{|\mathbf{R}_I - \mathbf{R}_J|}}_{\text{nuclear-nuclear}}. \quad (2.5)$$

In equation (2.5) i, j, I and J are running variables for the electrons (small letters) and the nuclei (capital letters), respectively. Further, the space vector of an electron is given by \mathbf{r}_i and the respective vector for the nuclei by \mathbf{R}_I while e represents the elementary charge, ϵ_0 the vacuum permittivity and Z_I the nuclear charge of species I .

The first term describes the attractive interaction between the electrons and the nuclei, where the \mathbf{R}_I 's are constant due to BO. In the second term the repulsive interaction of the electrons is given via the Coulomb potential. The last term, which represents the repulsive interaction of the nuclei, becomes constant within BO. Double counting is accounted for in the last two terms by the prefactor 1/2.

Given realistic systems ($N \propto 10^{23}$) the Hamiltonian becomes very large. As the Schrödinger equation contains all information about the system within the many-body wave functions $\Psi^\sigma(\mathbf{r}_1^\sigma, \mathbf{r}_2^\sigma, \dots, \mathbf{r}_N^\sigma)$ (with $4N$ dimension, including 3 dimensions for the spatial variables and one dimension for the scalar spin variable per particle), an analytic solution can only be obtained for very simple systems (e.g. H_2^+). Thus, it becomes increasingly challenging to obtain a solution of this equation for bigger systems like molecules. This is why approximations (next to BO) have to be applied to calculate the properties of such systems. One such approximation is density functional theory.

2.1. DENSITY FUNCTIONAL THEORY (DFT)

Hohenberg and Kohn Formulating DFT as an exact many-body theory was proposed by Hohenberg and Kohn (HK) in 1964 [22]. This approach can be used for any system of interacting particles in an external potential and is the theoretical foundation of DFT.

It is based on two major theorems. The first theorem states that the external potential $V_{\text{ext}}(\mathbf{r})$ for any system of interacting particles within a given potential is uniquely determined by the non-degenerated ground state density $n_0(\mathbf{r})$. This fully determines the Hamiltonian \hat{H} and with that the many-body wave functions for all states, ground and excited ones. With that, the knowledge of the ground state density completely determines all properties of a system. Consequently, there cannot be two external potentials which differ in more than a constant leading to the same ground state density.

The second theorem introduces a universal energy functional $E[n(\mathbf{r})]$ with respect to the density $n(\mathbf{r})$, which is defined for any external potential. For any particular potential $V_{\text{ext}}(\mathbf{r})$, the global minimum of this functional provides the exact ground state energy and with that the exact ground state density. The term 'universal' means that this functional can be used for any electronic system independently of $V_{\text{ext}}(\mathbf{r})$. Writing the total energy functional gives

$$E_{\text{HK}}[n(\mathbf{r})] = F_{\text{HK}}[n(\mathbf{r})] + \int V_{\text{ext}}(\mathbf{r})n(\mathbf{r})d^3r, \quad (2.6)$$

where the last term introduces the interaction of the density with the external potential and

$$F_{\text{HK}}[n(\mathbf{r})] = T[n(\mathbf{r})] + E_{\text{inter}}[n(\mathbf{r})] \quad (2.7)$$

describes the kinetic energy T and the electron-electron interaction E_{inter} . In summary, the energy as described by the HK functional in equation (2.6) for the correct ground state density is lower than for any other density. Consequently, the exact ground state energy and density could be obtained by minimizing equation (2.6) with respect to variations of the density (if the functional $F_{\text{HK}}[n(\mathbf{r})]$ would be known). With that, the explicit treatment of the wave function $\Psi^\sigma(\mathbf{r}_1^\sigma, \mathbf{r}_2^\sigma, \dots, \mathbf{r}_N^\sigma)$, depending on $4N$ variables, can be replaced by the treatment of the electron density $n^\sigma(\mathbf{r})$, depending on only four variables.

Kohn and Sham The theorems of HK provide a theoretical foundation of DFT, but are not concerned with its realization. Kohn and Sham (KS) [23] solved this issue by proposing their equations in 1965. Those equations can be considered as the most important theoretical foundation of density functional theory next to HK.

Within their ansatz, they face the problem that a quantum mechanical system is represented by many-body wave functions of an interacting many-particle system. To deal with such systems, Kohn and Sham replaced the complicated system with a non-interacting single particle system. The idea is that the exact ground state density is equal to the density of this properly chosen auxiliary system.

With that, the system can be described by single particle wave functions $\phi(\mathbf{r})$ instead of the many-body wave functions $\Psi(\mathbf{r})$ (see figure 2.1). The interactions are implemented into an exchange-correlation functional $E_{\text{xc}}[n]$. This allows the use this functional instead of explicitly considering all many-body interactions to solve the problem. If such a functional would be known exactly, DFT could be implemented as an exact theory.

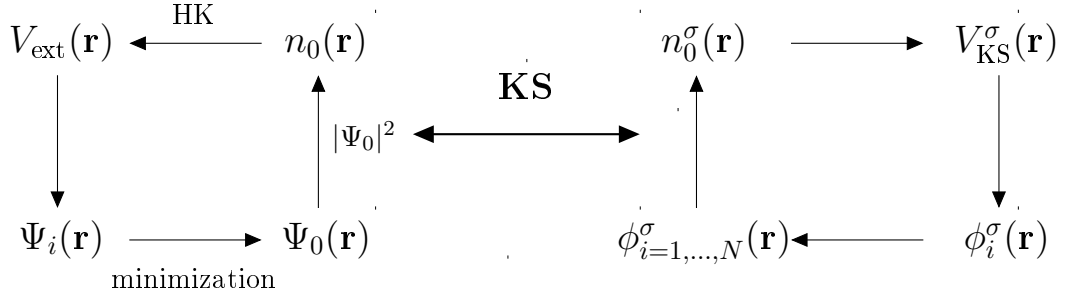


Figure 2.1.: Visualization of the ansatz introduced by Kohn and Sham. The many-body interacting system (left side) is transformed into a single particle non-interacting auxiliary system (right side).

The Kohn-Sham equations read [33]²

$$\frac{\partial T_S}{\partial \phi_i^{\sigma*}(\mathbf{r})} = -\frac{\hbar^2}{2m_e} \nabla^2 \phi_i^\sigma(\mathbf{r}), \quad (2.8)$$

$$\frac{\partial n^\sigma(\mathbf{r})}{\partial \phi_i^{\sigma*}(\mathbf{r})} = \phi_i^\sigma(\mathbf{r}), \quad (2.9)$$

$$V_{\text{KS}}^\sigma(\mathbf{r}) = V_{\text{ext}}(\mathbf{r}) + \frac{\partial E_{\text{Hartree}}}{\partial n^\sigma(\mathbf{r})} + \frac{\partial E_{\text{xc}}}{\partial n^\sigma(\mathbf{r})}, \quad (2.10)$$

where T_S is the kinetic energy, $V_{\text{ext}}(\mathbf{r})$ is the external potential, E_{Hartree} is the Hartree energy term and E_{xc} is the exchange-correlation energy term.

Considering these expressions, a Schrödinger-like equation can be written like

$$\hat{H}_{\text{KS}}^\sigma(\mathbf{r}) \phi_i^\sigma(\mathbf{r}) = \left[-\frac{\hbar^2}{2m_e} \nabla^2 + V_{\text{KS}}^\sigma(\mathbf{r}) \right] \phi_i^\sigma(\mathbf{r}) = \epsilon_i^\sigma \phi_i^\sigma(\mathbf{r}), \quad (2.11)$$

with the eigenvalues ϵ_i^σ and the effective Hamiltonian $\hat{H}_{\text{KS}}^\sigma(\mathbf{r})$. Those equations can now be used to obtain properties of a given system using a self-consistent cycle (see figure 2.2).

² The treatment of the spin variable σ is a formal extension of the original KS ansatz, where the spin was not explicitly treated. However, the derivation remains unchanged. With that, the spin variable is displayed here.

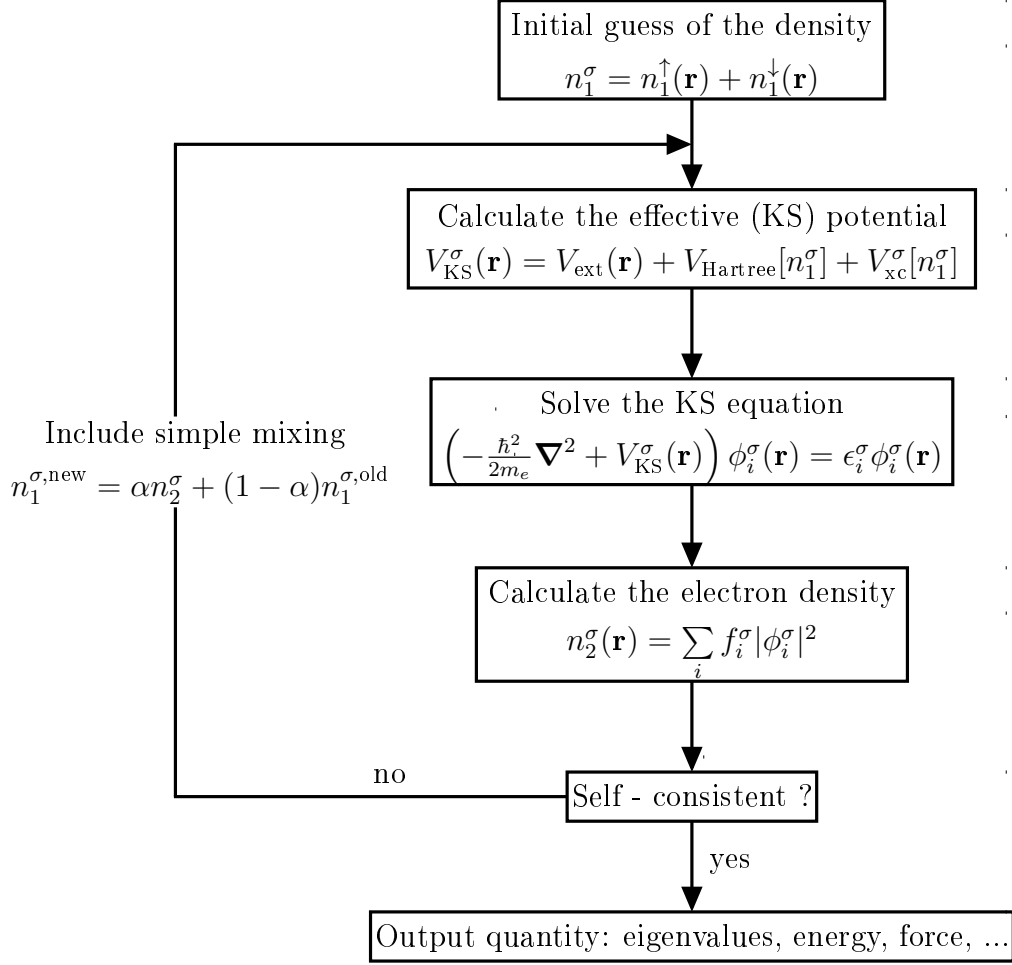


Figure 2.2.: Self-consistent cycle using the Kohn-Sham equations. The f_i^σ are weight functions for the respective spin orientation σ (\uparrow or \downarrow) and α is the mixing factor (only a simple mixing procedure is visualized).

2.2. CURRENT DENSITY AND MAGNETIC SHIELDING

Current density Considering that HK is only formulated for a spin-paired electron density without the inclusion of an external magnetic field, extensions to the original formulation of DFT are needed. Spin interactions were already introduced by Kohn and Sham [23] to describe the spin susceptibility. Another extension considering quantum electrodynamics was introduced by Rajagopal and Callaway [18]. There, the dependence of the energy functional was changed from the charge density to the current density $\mathbf{J}(\mathbf{r})$

$$E[\mathbf{J}] = F[\mathbf{J}] - \int J_\mu(\mathbf{r}) A_{\text{ext}}^\mu(\mathbf{r}) d^3r, \quad (2.12)$$

with the external nonquantized electromagnetic field $A_{\text{ext}}^\mu(r) = (V_{\text{ext}}, \mathbf{A}_{\text{ext}})$, a four vector potential containing the scalar external potential V_{ext} and the external vector potential \mathbf{A}_{ext} . The term $F[\mathbf{J}]$ contains

$$F[\mathbf{J}] = \langle \Psi_0 | H_0 + H_C + H_I | \Psi_0 \rangle, \quad (2.13)$$

where Ψ_0 is the ground state wave function. H_0 describes noninteracting Dirac and electromagnetic fields, H_C refers to the Coulomb interaction between electrons and H_I is the interaction between matter and the transverse portion of the radiation field. The four current density can be defined as

$$J_\mu(\mathbf{r}) = \langle \Psi_0 | j_\mu(\mathbf{r}) | \Psi_0 \rangle, \quad (2.14)$$

which has to obey the equation of continuity $\partial_\mu J^\mu(\mathbf{r}) = 0$. Further extension included the spin of the system, leading to

$$E[\mathbf{J}] = F[\mathbf{J}] + \int \left(en(\mathbf{r})V(\mathbf{r}) + \frac{e}{2m_e} \mathbf{s}(\mathbf{r}) \cdot \mathbf{B}(\mathbf{r}) + \frac{ei}{2m_e} \frac{\partial}{\partial t} \mathbf{g} \cdot \mathbf{A} - \mathbf{J}(\mathbf{r}) \cdot \mathbf{A}(\mathbf{r}) \right) d^3r, \quad (2.15)$$

where $\mathbf{B} = \nabla \times \mathbf{A}_{\text{ext}}$. Consequently, the energy is a functional of the current density consisting of four terms, the charge density, the spin density, the ordinary current (which vanishes in stationary problems) and the polarization current. The components are independent besides the restrictions from the continuity equation.

This extension allows the analysis of the spin and the current of a system within DFT. These properties are necessary to describe the magnetism as well as the NMR magnetic shielding, which are both investigated within this thesis.

An implementation of the four current density within DFT to calculate NMR shieldings was proposed in 1985 by Bieger et al. [19]. There, the zero spin density case (diamagnetic systems) was approached by rewriting equation (2.12) in terms of the non-relativistic charge density $n(\mathbf{r})$ and the current density $\mathbf{J}(\mathbf{r})$ like

$$E[n, \mathbf{J}] = F[n, \mathbf{J}] + \int [n(\mathbf{r})V_{\text{ext}}(\mathbf{r}) - \frac{1}{c} \mathbf{J}(\mathbf{r}) \cdot \mathbf{A}_{\text{ext}}(\mathbf{r})] d^3r. \quad (2.16)$$

Using this equation as a starting point, with

$$n(\mathbf{r}) = \sum_k^{\text{occ}} \Psi_k^* \Psi_k \quad (2.17)$$

and

$$\mathbf{J}(\mathbf{r}) = \sum_k^{\text{occ}} \left[\frac{1}{2} i (\Psi_k \nabla \Psi_k^* - \Psi_k^* \nabla \Psi_k) - \frac{1}{c} \mathbf{A}_{\text{ext}} \Psi_k \Psi_k^* \right], \quad (2.18)$$

a generalization of the Kohn-Sham equations including an external vector potential can be defined like

$$\left(\left[-\frac{1}{2} \nabla^2 - \frac{1}{c} i (\mathbf{A}_{\text{ext}} + \mathbf{A}_{\text{xc}}) \nabla + \frac{1}{c^2} (\mathbf{A}_{\text{ext}} - \mathbf{A}_{\text{xc}})^2 \right] + (V_{\text{ext}} + V_{\text{xc}}) + V_{\text{H}} \right) \Psi_k = \epsilon_k \Psi_k, \quad (2.19)$$

where $V_{\text{xc}} = \partial E_{\text{xc}} / \partial n$, $\mathbf{A}_{\text{xc}} = \partial E_{\text{xc}} / \partial \mathbf{J}$, V_{H} is the Hartree term and E_{xc} is the exchange-correlation energy depending on the current \mathbf{J} .

Considering that the magnetic shielding is a linear response quantity, it is possible to expand \mathbf{J} , Ψ_k and the one-particle Hamiltonian \hat{h} up to first order of \mathbf{B}_{ext} .

With this ansatz, one can solve the unperturbed problem, i.e. the Kohn-Sham equations for the system, and afterwards evaluate the perturbed wave function $\Psi_k^{(1)}$. This wave function influences the exchange-correlation potential as well as the exchange-correlation contribution to the vector potential. Finally, this new potential leads to a new $\Psi_k^{(1)}$. As the correct expression for the exchange-correlation contribution is unknown, further assumptions are made. In specific, \mathbf{A}_{xc} and the contribution of $\mathbf{J}(\mathbf{r})$ to V_{xc} are neglected. This yields the magnetic shielding as [19, 20]

$$\sigma_{uv} = \underbrace{\frac{1}{2c^2} \sum_k^{\text{occ}} \langle \Psi_k^{(0)} | \frac{\partial}{\partial B_\nu} ((\mathbf{B} \times \mathbf{r}) \times (\mathbf{r} - \mathbf{R}))_\nu | \Psi_k^{(0)} \rangle}_{\sigma_{\text{dia}}} - \underbrace{\frac{2}{c} \sum_k^{\text{occ}} \langle \Psi_k^{(0)} | \frac{(L_R)_u}{|\mathbf{r} - \mathbf{R}|^3} | (\Psi_k^{(1)})_\nu \rangle}_{\sigma_{\text{para}}}, \quad (2.20)$$

with $\mathbf{L}_R = \frac{1}{i}(\mathbf{r} - \mathbf{R}) \times \nabla$ being the angular momentum operator. The first term describes the diamagnetic term σ_{dia} and only depends on the unperturbed wave functions, while the second term is the paramagnetic term σ_{para} and depends on the perturbed wave function. An excellent review on the topic was given by Heine et al. [20].

Magnetic shielding One quantity that is related to NMR experiments is the magnetic shielding (see section 2.6). The interaction between a magnetic field \mathbf{B} and a nuclear spin 1/2 nucleus with spin angular momentum $\hbar \mathbf{I}_s$ can be expressed by [34]

$$\hat{H} = - \sum_s \gamma_s \mathbf{I}_s \cdot \mathbf{B}_{\text{tot}} = - \sum_s \gamma_s \mathbf{I}_s (1 - \sigma_{\alpha\beta}(\mathbf{r}_s)) \mathbf{B}_{\text{ext}}. \quad (2.21)$$

Here, the sum runs over all nuclei at sites s , γ_s is the magnetogyric ratio for the nuclei under observation and \mathbf{I}_s is the spin of nucleus s . In this consideration the magnetic field \mathbf{B}_{tot} is the field at the nucleus caused by an applied external field \mathbf{B}_{ext} and an induced field \mathbf{B}_{ind} . Further, $\sigma_{\alpha\beta}(\mathbf{r}_s)$ is the magnetic shielding tensor at site s ($\alpha, \beta \dots$ cartesian coordinates).

The first term on the right hand side in equation (2.21) defines the interaction of the bare nucleus with the applied field while the second term accounts for the response of the electronic structure to the external field. The external field induces a current in the system, which changes the influence of the external field on the nucleus. This is described by the magnetic shielding tensor as

$$B_{\text{ind},\alpha}(\mathbf{r}_s) = -\sigma_{\alpha\beta}(\mathbf{r}_s) B_{\text{ext},\beta}. \quad (2.22)$$

The minus sign denotes the tendency for electrons to align antiparallel to an applied field. For diamagnets, the induced field arises from orbital currents $\mathbf{J}(\mathbf{r})$ at any position \mathbf{r} as described by the Biot-Savart law [35]

$$\mathbf{B}_{\text{ind}}(\mathbf{r}) = \frac{1}{c} \int \mathbf{J}(\mathbf{r}') \times \frac{\mathbf{r} - \mathbf{r}'}{|\mathbf{r} - \mathbf{r}'|^3} d^3 r'. \quad (2.23)$$

Thus, it is necessary to calculate the currents (see section 2.4) to evaluate the induced field and consequently the magnetic shielding.

For closed shell atoms (e.g. ^{129}Xe) the so-called Lamb shift [36, 37, 38] describes the diamagnetic shielding σ_{dia} , as there is no paramagnetic contribution if the gauge origin lies within the center of the atom. It uses a $1/r$ dependence of the shielding with respect to all occupied orbitals such as

$$\sigma_{\text{dia}} = \frac{e^2}{3mc^2} \sum_i \langle \Psi_{i,0} | \frac{1}{r_i} | \Psi_{i,0} \rangle, \quad (2.24)$$

with $\Psi_{i,0}$ being the ground state wave function of orbital i with radius r_i . Thus, the summation over all contributions of the occupied orbitals gives access to the diamagnetic shielding term. The prefactor is evaluated in atomic units ($e = m = 1$) and becomes $1/(3c^2) \approx 1.78 \cdot 10^{-5}$, with $c = 137.036$ being the inverse of the fine-structure constant α^3 .

2.3. EXCHANGE-CORRELATION FUNCTIONALS

Because the exchange-correlation functional is not known exactly (see section 2.1), approximations are needed to enable calculations in the framework of DFT. One approximation is the local density approximation (LDA) as proposed by Kohn and Sham [23]. The LDA is based on the fact that a system can be described within the limit of the homogeneous electron gas. Effects of exchange and correlation are then local in character. Consequently, the density of the homogeneous electron gas is taken as a starting point.

With that, the exchange-correlation functional can be expressed as an integral over space with the exchange-correlation energy density ϵ_{xc} at each point r being the same as the homogeneous electron gas at this density

$$E_{\text{xc}}^{\text{LDA}}[n(\mathbf{r})] = \int n(\mathbf{r}) \epsilon_{\text{xc}}(n(\mathbf{r})) d^3r. \quad (2.25)$$

A formal extension of the LDA is the so-called local spin density approximation (LSDA), where the density is divided into two spin densities $n(\mathbf{r}) = n^\uparrow(\mathbf{r}) + n^\downarrow(\mathbf{r})$ [33], leading to the following expression for the exchange-correlation functional

$$E_{\text{xc}}^{\text{LSDA}}[n^\uparrow(\mathbf{r}), n^\downarrow(\mathbf{r})] = \int n(\mathbf{r}) \epsilon_{\text{xc}}^{\text{hom}}(n^\uparrow(\mathbf{r}), n^\downarrow(\mathbf{r})) d^3r, \quad (2.26)$$

with $\epsilon_{\text{xc}}^{\text{hom}} = \epsilon_{\text{x}}^{\text{hom}} + \epsilon_{\text{c}}^{\text{hom}}$. By introducing the fractional spin polarization $\xi(\mathbf{r})$

$$\xi(\mathbf{r}) = \frac{n^\uparrow(\mathbf{r}) - n^\downarrow(\mathbf{r})}{n^\uparrow(\mathbf{r}) + n^\downarrow(\mathbf{r})} \quad (2.27)$$

an analytic expression for the exchange part [33] can be derived. Similar expressions for the correlation energy do not exist and have to be approximated (e.g. using Quantum Monte Carlo simulations for different densities). In general the LSDA delivers reasonable results, but has some drawbacks like a consistent overbinding.

³ $\alpha = \frac{1}{4\pi\epsilon_0} \frac{e^2}{\hbar c} = 7.29735256 \cdot 10^{-3}$ using the values given in Abbreviations, units and constants.

Other approximations next to LSDA are the so-called generalized gradient approximations (GGAs). In contrast to LSDA, in GGAs not only the value of the density at each point r is taken into account, but the gradient of the density $|\nabla n^\sigma|$ is considered as well [39]

$$E_{\text{xc}}^{\text{GGA}}[n^\uparrow, n^\downarrow] = \int n(\mathbf{r}) \epsilon_{\text{xc}}(n^\uparrow, n^\downarrow, |\nabla n^\uparrow|, |\nabla n^\downarrow|) d^3r \quad (2.28)$$

$$= \int n(\mathbf{r}) \epsilon_{\text{x}}^{\text{hom}}(n) F_{\text{xc}}(n^\uparrow, n^\downarrow, |\nabla n^\uparrow|, |\nabla n^\downarrow|) d^3r. \quad (2.29)$$

Here, $\epsilon_{\text{x}}^{\text{hom}}(n)$ is the exchange energy per particle in a homogeneous electron gas and F_{xc} denotes an enhancement factor over the local exchange. One of the most famous and widely used GGAs has been introduced by Perdew, Burke and Ernzerhof (PBE) in 1996 [1], which is mainly employed in this thesis. The robustness of the PBE functional stems from the usage of as few free parameters as possible, making this GGA almost independent of the considered system and easily transferable.

To treat long-range dispersion corrections (van der Waals (vdW) interactions), the approach of Grimme [2] has been used. This semiempirical ansatz is based on a dispersion correction to the total KS-DFT energy given by

$$E_{\text{disp}} = -s_6 \sum_{i=1}^{N_{\text{atom}}-1} \sum_{j=i+1}^{N_{\text{atom}}} \frac{C_6^{ij}}{R_{ij}^6} f_{\text{dmp}}(R_{ij}), \quad (2.30)$$

where s_6 is a global scaling factor depending on the employed functional, N_{atom} is the number of atoms, C_6^{ij} is the pair dispersion coefficient and R_{ij} the interatomic distance between i and j . To avoid singularities for $R_{ij} \rightarrow 0$, a damping function is introduced such as

$$f_{\text{dmp}}(R_{ij}) = \frac{1}{1 + e^{-d(R_{ij}/R_{\text{vdW}}-1)}}, \quad (2.31)$$

with R_{vdW} being the sum of the vdW radii and d is a scaling parameter. The pair dispersion coefficient can be obtained from the atomic coefficients via a geometric mean

$$C_6^{ij} = \sqrt{C_6^i C_6^j}. \quad (2.32)$$

Further, the atomic coefficient for atom i is defined as

$$C_6^i = 0.05 N I_{\text{p}}^i \alpha^i, \quad (2.33)$$

using $N = 2, 10, 18, 36, 54$ for atoms of row 1-5 of the periodic table, I_{p} as the atomic ionization potential and α as the static dipole polarizability. All required values were derived in the work of Grimme to provide dispersion corrections for elements up to Xe.

2.4. BASIS SETS AND PSEUDOPOTENTIALS

In general, the KS-orbitals Ψ can be expressed as a linear combination of basis functions ϕ

$$\Psi = \sum_i c_i \phi_i, \quad (2.34)$$

with c_i being the corresponding coefficients for the respective basis function. There are two major classes of basis functions. The first class are non-localized functions like plane waves, which are widely employed due to their ability to treat periodic boundary conditions (PBCs). The second class are localized atomic-like orbitals (e.g. linearized muffin-tin orbitals [40], Slater- [41] or Gaussian-type orbitals [42]), usually treating finite systems. The wave function of an infinite system can be expressed as a sum of wave functions at reciprocal lattice vectors using non-localized plane waves [43]

$$\Psi_i = e^{i\mathbf{k}\mathbf{r}} \sum_{\mathbf{G}} c_{i,\mathbf{G}} e^{i\mathbf{G}\mathbf{r}} = e^{i\mathbf{k}\mathbf{r}} \phi_{\mathbf{G}}(\mathbf{r}), \quad (2.35)$$

with \mathbf{k} being a reciprocal space vector and \mathbf{G} being a reciprocal lattice vector. The reciprocal lattice is given by

$$\mathbf{b}_i = 2\pi \frac{\mathbf{a}_j \times \mathbf{a}_k}{\mathbf{a}_i \cdot (\mathbf{a}_j \times \mathbf{a}_k)} \quad (2.36)$$

and cyclic permutations (\mathbf{a} are the conventional lattice vectors). The first term in equation (2.35) describes the wave part while the second term denotes the periodicity part. With that, each wave function can be written as a sum of plane waves

$$\Psi_i = \sum_{\mathbf{G}} c_{i,\mathbf{k}+\mathbf{G}} e^{i(\mathbf{k}+\mathbf{G})\mathbf{r}}. \quad (2.37)$$

The more plane waves are taken into account, the more accurate the description of the given periodic system. Considering the kinetic energy per plane wave

$$-\frac{\hbar^2}{2m_e} \Delta \phi_{\mathbf{G}}(\mathbf{r}) = \frac{\hbar^2}{2m_e} |\mathbf{k} + \mathbf{G}|^2 \phi_{\mathbf{G}}(\mathbf{r}) \quad (2.38)$$

allows an evaluation of how many plane waves should be taken into account. As plane waves with a smaller kinetic energy usually play a more important role than the ones with higher kinetic energy, a kinetic energy cutoff can be introduced by

$$E_{\text{cutoff}} \geq \frac{\hbar^2}{2m_e} |\mathbf{k} + \mathbf{G}_{\text{max}}|^2, \quad (2.39)$$

restricting the basis set to plane waves with a kinetic energy smaller than E_{cutoff} . A plane wave basis set is easy to implement and obtains good convergence in accordance to the size of the basis set ($\hat{=}$ reasonably large energy cutoffs). For the description of pseudopotentials in combination with plane waves, several methods like the orthogonalized plane wave (OPW) method by Herring [44] and the augmented plane wave (APW) method by Slater [45] were developed. Another approach proposed by Phillips and Kleinman [46] states that an effective potential (which eigenstates are pseudo wave functions based on plane waves) could be derived from all-electron potentials and wave functions.

The general idea of pseudopotentials is to replace the real (Coulomb) potential which acts on all electrons with an effective potential acting on the valence electrons only [47]. As core electrons usually play a minor role considering bond formation and other physical properties, their effect can be included in the effective potential (see figure 2.3). This reduces computational time while preserving the quality of most resulting properties.

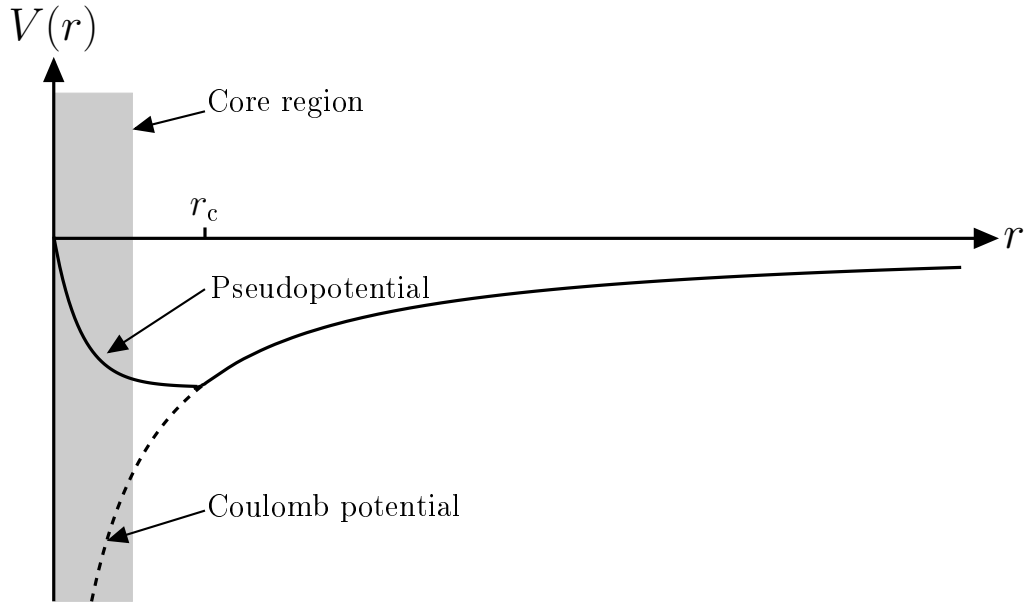


Figure 2.3.: Sketch of a pseudopotential in comparison with the real ionic potential (Coulomb potential). The two potential differ for distances smaller than a cutoff radius r_c and are the same for any larger distances [47].

The resulting wave functions do not have a nodal structure like the correct wave functions, which is however of less relevance for most properties [47] (see figure 2.4 ⁴).

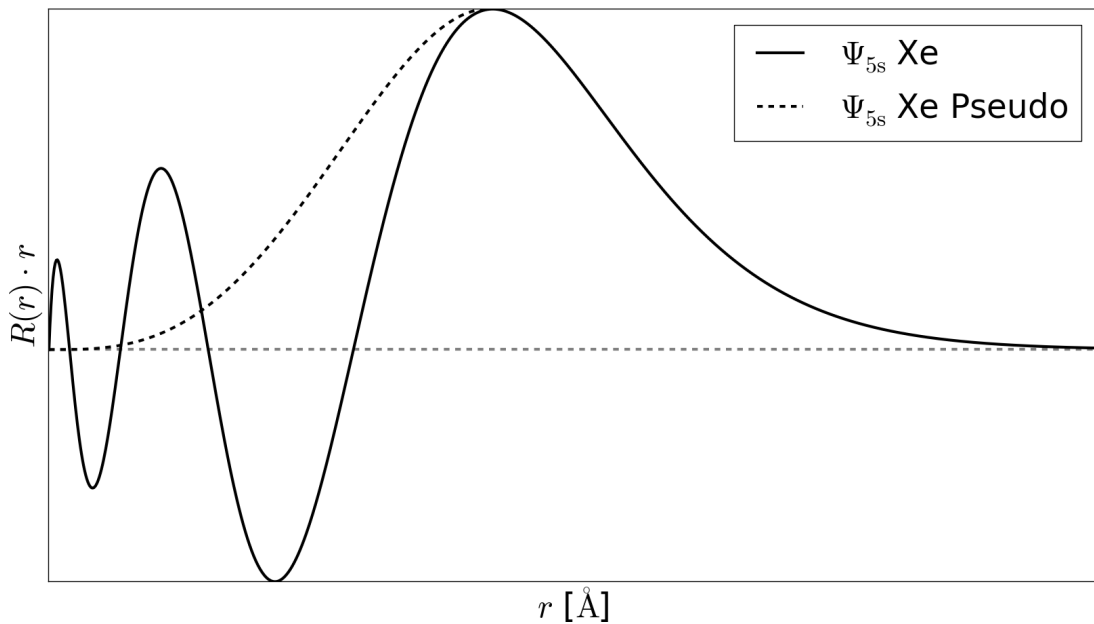


Figure 2.4.: Illustration of the radial part of the 5s wave function of Xe. The correct nodal behavior is plotted alongside a pseudo wave function, which has no nodal behavior (compare with e.g. [48]).

⁴ $R_{5s}(r) = \frac{8}{187500\sqrt{5}} \left(\frac{Z}{a_B}\right)^{\frac{3}{2}} \left(9375 - 7500\frac{Zr}{a_B} + 1500\left(\frac{Zr}{a_B}\right)^2 - 100\left(\frac{Zr}{a_B}\right)^3 + 2\left(\frac{Zr}{a_B}\right)^4\right) e^{-\frac{Zr}{5a_B}}$.
 Z is the effective nuclear charge and a_B is the Bohr radius with $a_B = 0.529177 \text{ \AA}$.

Projector-augmented wave method A special type of pseudopotentials is based on the so-called projector-augmented wave (PAW) method [49], which has been used for all electronic structure calculations in this thesis. Within this method, a linear operator \mathcal{T} maps the valence pseudo wave function $|\tilde{\Psi}\rangle$ onto the corresponding all-electron wave function like $|\Psi\rangle = \mathcal{T}|\tilde{\Psi}\rangle$. A set of target all-electron partial waves $|\phi_{\mathbf{R},n}\rangle$ can be obtained by applying \mathcal{T} on a set of pseudo partial waves $|\tilde{\phi}_{\mathbf{R},n}\rangle$ with

$$\mathcal{T} = \mathbf{1} + \sum_{\mathbf{R},n} \left[|\phi_{\mathbf{R},n}\rangle - |\tilde{\phi}_{\mathbf{R},n}\rangle \right] \langle \tilde{p}_{\mathbf{R},n}|, \quad (2.40)$$

where $\langle \tilde{p}_{\mathbf{R},n}|$ is a set of projectors which obey $\langle \tilde{p}_{\mathbf{R},n}|\tilde{\phi}_{\mathbf{R}',m}\rangle = \delta_{\mathbf{R},\mathbf{R}'}\delta_{n,m}$. Each partial wave and projector is an atomic like function centered on atomic site \mathbf{R} . The index n refers to the angular momentum quantum number and an additional number which is used if there is more than one projector per angular momentum. The expectation value of any operator \mathcal{O} corresponding to the all-electron wave functions can be obtained by a pseudo operator $\tilde{\mathcal{O}} = \mathcal{T}^+\mathcal{O}\mathcal{T}$ related to the corresponding pseudo wave functions. Given a set of assumptions, Blöchl [49] has shown that if \mathcal{O} is a local or semilocal operator (e.g. \mathbf{p} or p^2)⁵ the pseudo operator can be written as

$$\tilde{\mathcal{O}} = \mathcal{O} + \sum_{\mathbf{R},n,m} |\tilde{p}_{\mathbf{R},n}\rangle \left[\langle \phi_{\mathbf{R},n}|\mathcal{O}|\phi_{\mathbf{R},m}\rangle - \langle \tilde{\phi}_{\mathbf{R},n}|\mathcal{O}|\tilde{\phi}_{\mathbf{R},m}\rangle \right] \times \langle \tilde{p}_{\mathbf{R},m}|. \quad (2.41)$$

Applying this method in an electronic structure calculation allows to describe all-electron properties based on pseudo wave functions, making it accurate as well as numerically feasible.

Gauge-including PAW method An extension to the PAW method was introduced by Pickard and Mauri [50]. Their ansatz is based on the problem that the exact translational invariance within an external field cannot be ensured by the original PAW method. The pseudo wave functions constructed with \mathcal{T} do not transform according to

$$\langle \mathbf{r}|\Psi'_n\rangle = e^{(i/2c)\mathbf{r}\cdot\mathbf{t}\times\mathbf{B}} \langle \mathbf{r} - \mathbf{t}|\Psi_n\rangle, \quad (2.42)$$

where \mathbf{t} is a translation vector. To account for this problem and to restore the translational invariance within a PAW-like approach, a field dependent transformation operator $\mathcal{T}_{\mathbf{B}}$ can be defined, which imposes the translational invariance exactly

$$\mathcal{T}_{\mathbf{B}} = \mathbf{1} + \sum_{\mathbf{R},n} e^{(i/2c)\mathbf{r}\cdot\mathbf{R}\times\mathbf{B}} \left[|\phi_{\mathbf{R},n}\rangle - |\tilde{\phi}_{\mathbf{R},n}\rangle \right] \langle \tilde{p}_{\mathbf{R},n}| e^{-(i/2c)\mathbf{r}\cdot\mathbf{R}\times\mathbf{B}}. \quad (2.43)$$

This new operator is the basis of a new approach called the gauge-including projector-augmented wave (GIPAW). The GIPAW pseudo operator $\bar{\mathcal{O}} = \mathcal{T}_{\mathbf{B}}^+\mathcal{O}\mathcal{T}_{\mathbf{B}}$ corresponding to a local or semilocal operator \mathcal{O} can be defined as

⁵ In this section, \mathbf{p} instead of \hat{p} will be used for the momentum operator to avoid confusion with between this operator and the projector functions.

$$\begin{aligned}
\bar{\mathcal{O}} = & \mathcal{O} + \sum_{\mathbf{R},n,m} e^{(i/2c)\mathbf{r}\cdot\mathbf{R}\times\mathbf{B}} |\tilde{p}_{\mathbf{R},n}\rangle \\
& \times \left[\langle \phi_{\mathbf{R},n} | e^{-(i/2c)\mathbf{r}\cdot\mathbf{R}\times\mathbf{B}} \mathcal{O} e^{(i/2c)\mathbf{r}\cdot\mathbf{R}\times\mathbf{B}} | \phi_{\mathbf{R},m} \rangle \right. \\
& \left. - \langle \tilde{\phi}_{\mathbf{R},n} | e^{-(i/2c)\mathbf{r}\cdot\mathbf{R}\times\mathbf{B}} \mathcal{O} e^{(i/2c)\mathbf{r}\cdot\mathbf{R}\times\mathbf{B}} | \tilde{\phi}_{\mathbf{R},m} \rangle \right] \\
& \times \langle \tilde{p}_{\mathbf{R},m} | e^{-(i/2c)\mathbf{r}\cdot\mathbf{R}\times\mathbf{B}} .
\end{aligned} \tag{2.44}$$

This method can be connected to the widely used gauge-including atomic orbitals (GIAO) [51] and the independent gauge for localized orbitals (IGLO) [52] methods. However, in GIPAW the phase required to maintain the translational invariance is carried by the operator, while in GIAO and IGLO the field dependent phase is attached to the basis functions. The GIPAW method allows the calculation of the current, which is necessary for the evaluation of the magnetic shielding. Within the GIPAW method, the current is splitted into several terms [50]

$$\mathbf{j}^{(1)}(\mathbf{r}') = \mathbf{j}_{\text{bare}}^{(1)}(\mathbf{r}') + \mathbf{j}_{\Delta\text{p}}^{(1)}(\mathbf{r}') + \mathbf{j}_{\Delta\text{d}}^{(1)}(\mathbf{r}'), \tag{2.45}$$

where $\mathbf{j}_{\text{bare}}^{(1)}(\mathbf{r}')$ is the bare contribution to the current, $\mathbf{j}_{\Delta\text{p}}^{(1)}(\mathbf{r}')$ denotes the paramagnetic correction to the current and $\mathbf{j}_{\Delta\text{d}}^{(1)}(\mathbf{r}')$ describes the diamagnetic correction to the current. All three terms are gauge invariant. With the knowledge of the current, one can evaluate the induced current by means of the Biot-Savart law (see section 2.2) and with that the magnetic shielding σ .

2.5. ELECTRONIC MAGNETISM

The first part of this thesis deals with the magnetism as introduced by spin-spin interaction of electrons. The Heisenberg-Dirac-Van Vleck Hamiltonian will be introduced as a model Hamiltonian. This model Hamiltonian will be used to describe the magnetic coupling between magnetic centers. As will be shown in the corresponding section, the calculation of the coupling constant is based on energy differences. The energies can be taken from spin-polarized KS-DFT calculations. Consequently, the previously mentioned extensions to standard KS-DFT (see section 2.2) are used to enable the description of spin polarization.

In the last part of this section, an introduction to the exchange mechanisms which are responsible for magnetic interactions will be briefly discussed.

2.5.1. HEISENBERG-DIRAC-VAN VLECK HAMILTONIAN

As already mentioned in the last chapter, accurate descriptions of complex systems are difficult to evaluate. This is why model Hamiltonians are introduced to make such descriptions possible. In case of magnetism, the Heisenberg Hamiltonian is such a model Hamiltonian. Within its formalism, the coordinates of all orbitals are replaced by spin operators. For this Hamiltonian it is assumed that the spins are independent and localized on their respective magnetic centers.

Taking those restrictions into account the Heisenberg-Dirac-Van Vleck (HDVV) Hamiltonian [53, 54, 55] can be defined as

$$\hat{H}_{\text{HDVV}} = -2 \sum_{i>j} J_{ij} \mathbf{S}_i \cdot \mathbf{S}_j, \quad (2.46)$$

where J_{ij} is the coupling constant between two spins i and j and $\mathbf{S}_{i,j}$ are spin operators/vectors of neighboring spins with $\mathbf{S}_i = (S_{i,x}, S_{i,y}, S_{i,z})^T$. A positive value of J_{ij} is described by a high-spin (ferromagnetic (FM)) coupling while a low-spin (antiferromagnetic (AFM)) coupling provides a negative value (see figure 2.5).

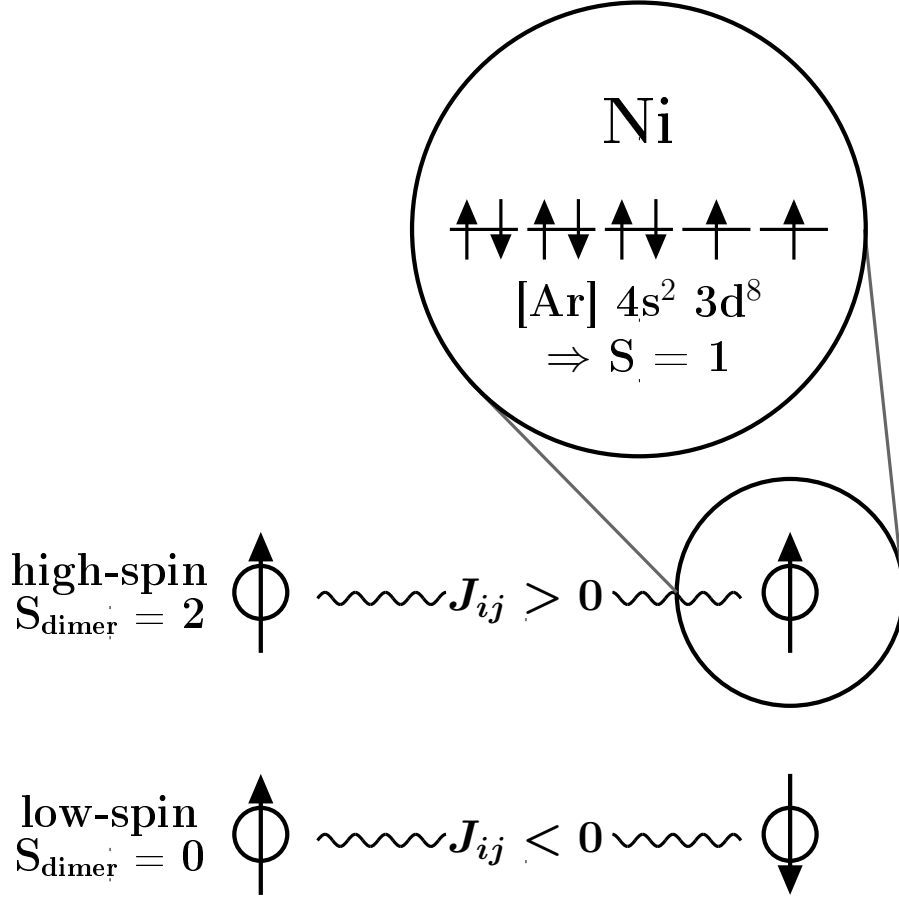


Figure 2.5.: Illustration of the magnetic interaction described by the coupling constant J_{ij} for a Ni dimer. A clarification of the spin contribution to the Ni d-states is additionally given.

In equation (2.46) double counting of the spins is excluded due to the restriction $i > j$. The minus sign is not always used in literature, changing the definition of the sign of J_{ij} referring to a magnetic ordering. As can be easily seen, the given Hamiltonian only describes isotropic media, as only relative orientations of the spins are taken into account. To evaluate anisotropic media as well, the orientation of the spins concerning the coordinates x , y and z have to be included using the following Hamiltonian

$$\hat{H}_{\text{anisotropic}} = -2 \sum_{i>j} J_{ij} [S_{i,z} S_{j,z} + \gamma (S_{i,x} S_{j,x} + S_{i,y} S_{j,y})], \quad (2.47)$$

with γ being a constant. Different values of this constant lead to several models. For $\gamma = 0$ the Ising model occurs, for $\gamma = 1$ one arrives at the Heisenberg model and $\gamma \gg 1$ leads to a two-dimensional interaction with negligible S_z values. A comparison between the Ising and the Heisenberg model is given in Appendix 2.

As the coupling constant J_{ij} is of interest considering magnetic properties, its derivation will be carried out next. For that purpose, the energies of a high-spin state and a low-spin state of neighboring spins i and j are compared. With that, the favourable magnetic orientation is determined. The energy difference between those two orderings can be expressed using the Heisenberg-Dirac-Van Vleck formalism⁶

$$\Delta E = E_{\text{high-spin}} - E_{\text{low-spin}} \quad (2.48)$$

$$\begin{aligned} &= -2J_{ij} \left[\langle \mathbf{S}_i \cdot \mathbf{S}_j \rangle_{\text{high-spin}} - \langle \mathbf{S}_i \cdot \mathbf{S}_j \rangle_{\text{low-spin}} \right] \\ \Delta E' = E_{\text{low-spin}} - E_{\text{high-spin}} &= 2J_{ij} \left[\langle \mathbf{S}_i \cdot \mathbf{S}_j \rangle_{\text{high-spin}} - \langle \mathbf{S}_i \cdot \mathbf{S}_j \rangle_{\text{low-spin}} \right]. \end{aligned} \quad (2.49)$$

For all further discussion, HS will be used for the high-spin state and LS for the low-spin state. Using equation (2.49) leads to the coupling constant J_{ij}

$$J_{ij} = \frac{\Delta E'}{2 \left[\langle \mathbf{S}_i \cdot \mathbf{S}_j \rangle_{\text{HS}} - \langle \mathbf{S}_i \cdot \mathbf{S}_j \rangle_{\text{LS}} \right]}. \quad (2.50)$$

As the expectation value for the term $\mathbf{S}_i \cdot \mathbf{S}_j$ is not known, the total spin \mathbf{S}_{tot} is introduced

$$\mathbf{S}_{\text{tot}} = \mathbf{S}_i + \mathbf{S}_j. \quad (2.51)$$

By squaring the last expression

$$\mathbf{S}_{\text{tot}}^2 = (\mathbf{S}_i + \mathbf{S}_j)^2 = \mathbf{S}_i^2 + 2\mathbf{S}_i \cdot \mathbf{S}_j + \mathbf{S}_j^2, \quad (2.52)$$

with the known expectation value $\langle \mathbf{S}^2 \rangle \rightarrow S(S+1)$, the following expression is obtained

$$\begin{aligned} \mathbf{S}_i \cdot \mathbf{S}_j &= \frac{\mathbf{S}_{\text{tot}}^2 - \mathbf{S}_i^2 - \mathbf{S}_j^2}{2} \\ \Rightarrow \langle \mathbf{S}_i \cdot \mathbf{S}_j \rangle &= \frac{\langle \mathbf{S}_{\text{tot}}^2 \rangle - \langle \mathbf{S}_i^2 \rangle - \langle \mathbf{S}_j^2 \rangle}{2}. \end{aligned} \quad (2.53)$$

For further simplifications, only dimers will be taken into account, i.e. $i = 1$ and $j = 2$. In equation (2.50) the expressions for $\langle \mathbf{S}_i \cdot \mathbf{S}_j \rangle_{\text{HS}}$ and $\langle \mathbf{S}_i \cdot \mathbf{S}_j \rangle_{\text{LS}}$ can be obtained using equation (2.53)

⁶ The notation high-spin (HS) and low-spin (LS) will be used instead of ferromagnetic and antiferromagnetic, denoting a parallel as well as an antiparallel alignment of the spins. This is done because the terms FM and AFM might not hold in their basic definition, e.g. in mixed dimers, where there is no strict AFM.

$$\langle \mathbf{S}_1 \cdot \mathbf{S}_2 \rangle_{\text{HS}} = \frac{\langle \mathbf{S}_{\text{tot}}^2 \rangle_{\text{HS}} - \langle \mathbf{S}_1^2 \rangle_{\text{HS}} - \langle \mathbf{S}_2^2 \rangle_{\text{HS}}}{2} \quad (2.54)$$

$$\langle \mathbf{S}_1 \cdot \mathbf{S}_2 \rangle_{\text{LS}} = \frac{\langle \mathbf{S}_{\text{tot}}^2 \rangle_{\text{LS}} - \langle \mathbf{S}_1^2 \rangle_{\text{LS}} - \langle \mathbf{S}_2^2 \rangle_{\text{LS}}}{2}. \quad (2.55)$$

Thus, the spin configurations of the whole dimers (\mathbf{S}_{tot}) and its constituents ($\mathbf{S}_1, \mathbf{S}_2$) are needed. Replacing the last two expressions in equation (2.50) leads to

$$\begin{aligned} J_{12,\text{general}} &= \frac{\Delta E'}{2 \left[\frac{\langle \mathbf{S}_{\text{tot}}^2 \rangle_{\text{HS}} - \langle \mathbf{S}_1^2 \rangle_{\text{HS}} - \langle \mathbf{S}_2^2 \rangle_{\text{HS}}}{2} - \frac{\langle \mathbf{S}_{\text{tot}}^2 \rangle_{\text{LS}} - \langle \mathbf{S}_1^2 \rangle_{\text{LS}} - \langle \mathbf{S}_2^2 \rangle_{\text{LS}}}{2} \right]} \\ &= \frac{\Delta E'}{\left[\langle \mathbf{S}_{\text{tot}}^2 \rangle_{\text{HS}} - (\langle \mathbf{S}_1^2 \rangle_{\text{HS}} + \langle \mathbf{S}_2^2 \rangle_{\text{HS}}) - \langle \mathbf{S}_{\text{tot}}^2 \rangle_{\text{LS}} + (\langle \mathbf{S}_1^2 \rangle_{\text{LS}} + \langle \mathbf{S}_2^2 \rangle_{\text{LS}}) \right]} \\ &= \frac{\Delta E'}{\left[\langle \mathbf{S}_{\text{tot}}^2 \rangle_{\text{HS}} - \langle \mathbf{S}_{\text{tot}}^2 \rangle_{\text{LS}} - (\langle \mathbf{S}_1^2 \rangle_{\text{HS}} + \langle \mathbf{S}_2^2 \rangle_{\text{HS}}) + (\langle \mathbf{S}_1^2 \rangle_{\text{LS}} + \langle \mathbf{S}_2^2 \rangle_{\text{LS}}) \right]} \\ J_{12,\text{general}} &= \frac{\Delta E'}{\left[\langle \mathbf{S}_{\text{tot}}^2 \rangle_{\text{HS}} - \langle \mathbf{S}_{\text{tot}}^2 \rangle_{\text{LS}} + \langle \mathbf{S}_1^2 \rangle_{\text{LS}} - \langle \mathbf{S}_1^2 \rangle_{\text{HS}} + \langle \mathbf{S}_2^2 \rangle_{\text{LS}} - \langle \mathbf{S}_2^2 \rangle_{\text{HS}} \right]}. \end{aligned} \quad (2.56)$$

With that, the general form of J_{ij} is obtained. This allows the evaluation of the coupling constant in systems where the spins on the specific centers \mathbf{S}_1 and \mathbf{S}_2 are different for the HS and LS state. However, the number of unpaired electrons usually does not change when comparing the HS and the LS state, simplifying equation (2.56) to

$$J_{12} = \frac{\Delta E'}{\left[\langle \mathbf{S}_{\text{tot}}^2 \rangle_{\text{HS}} - \langle \mathbf{S}_{\text{tot}}^2 \rangle_{\text{LS}} \right]}. \quad (2.57)$$

For equal atoms the term $\langle \mathbf{S}_{\text{tot}}^2 \rangle_{\text{LS}}$ might be 0 and equation (2.57) further simplifies to

$$J_{12} = \frac{\Delta E'}{\langle \mathbf{S}_{\text{tot}}^2 \rangle_{\text{HS}}}. \quad (2.58)$$

The energies can be obtained from spin-polarized DFT calculations. Because only energy differences matter, some methodological DFT errors will cancel. The accuracy of the calculated coupling constants profits from this error cancellation.

For a Ni(II) dimer the spins are $S_1 = S_2 = 1$. Accordingly, the expressions for the expectation values of the total spin are

$$S_{\text{tot,HS}} = 2 \Rightarrow \langle \mathbf{S}_{\text{tot}}^2 \rangle_{\text{HS}} \rightarrow 6 \quad (2.59)$$

$$S_{\text{tot,LS}} = 0 \Rightarrow \langle \mathbf{S}_{\text{tot}}^2 \rangle_{\text{LS}} \rightarrow 0. \quad (2.60)$$

This leads to the coupling constant using equation (2.57) or equation (2.58)

$$J_{\text{Ni-Ni}} = \frac{\Delta E'}{6}. \quad (2.61)$$

For a Cu dimer the spins are $S_1 = S_2 = 0.5$. In such a case the high-spin state has a spin of $S_{\text{HS}} = 1$. Because the two atoms are equal, equation (2.58) can be used to obtain

$$J_{\text{Cu-Cu}} = \frac{\Delta E'}{2}. \quad (2.62)$$

In a mixed Ni-Cu dimer the spins are $S_1 = 1$ and $S_2 = 0.5$. With that, $\langle \mathbf{S}_{\text{tot}}^2 \rangle_{\text{HS}}$ accounts to 3.75 and $\langle \mathbf{S}_{\text{tot}}^2 \rangle_{\text{LS}}$ to 0.75. Correspondingly, the coupling constant using equation (2.57) becomes

$$J_{\text{Ni-Cu}} = \frac{\Delta E'}{3}. \quad (2.63)$$

This formalism can be applied to any mixture of two atoms.

2.5.2. EXCHANGE MECHANISMS

In the following, an introduction in the exchange mechanisms shall be briefly outlined. A purely qualitative discussion will be carried out to introduce the basic concepts⁷. First of all, exchange can occur between two electrons with the same spin. It is described by the exchange integral J_{ab} between two electrons a and b , which are represented by their respective single-particle wave functions ψ_a and ψ_b . The exchange occurs between positions \mathbf{r}_1 and \mathbf{r}_2

$$J_{ab} = - \int \int \psi_a^*(\mathbf{r}_1) \psi_b^*(\mathbf{r}_2) \frac{1}{|\mathbf{r}_1 - \mathbf{r}_2|} \psi_a(\mathbf{r}_2) \psi_b(\mathbf{r}_1) d^3r_1 d^3r_2. \quad (2.64)$$

In contrast, the Coulomb integral

$$\begin{aligned} C_{ab} &= \int \int \psi_a^*(\mathbf{r}_1) \psi_b^*(\mathbf{r}_2) \frac{1}{|\mathbf{r}_1 - \mathbf{r}_2|} \psi_a(\mathbf{r}_1) \psi_b(\mathbf{r}_2) d^3r_1 d^3r_2. \\ &= \int \int \psi_a^2(\mathbf{r}_1) \frac{1}{|\mathbf{r}_1 - \mathbf{r}_2|} \psi_b^2(\mathbf{r}_2) d^3r_1 d^3r_2 \end{aligned} \quad (2.65)$$

acts on all electrons independent of their spin orientation and originates from the electron charge. Thus, there is a competition between these two terms leading to a specific magnetic behavior. Different mechanisms for the exchange interaction are distinguished.

Direct exchange The most simple mechanism is the direct exchange between two magnetic centers. Once two magnetic centers are very close to each other, they occupy the same space at the same time. As known from Pauli's exclusion principle, this is only possible if the spins align antiparallel. Once the centers are separated, the situation changes. As seen in equation (2.64), a decrease in energy can be achieved by aligning the two spins parallel, allowing them to be exchanged. This exchange counter-weights the Coulomb interaction (equation 2.65) which is present for any pair of electrons, parallel or antiparallel aligned. This type of exchange mechanism is rarely observed in organic molecules or single molecule magnets, which are of interest in this thesis.

⁷ There is no direct connection to the already introduced KS-DFT. However, for this basic overview single-particle wave functions will be used. This is done for the purpose of explaining the mechanisms. No calculations in a wave function theory based ansatz, like Hartree-Fock, were carried out.

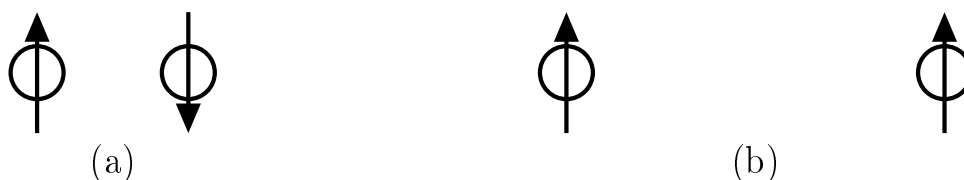


Figure 2.6.: Visualization of the direct exchange mechanism. In (a), the magnetic centers are very close to each other, resulting in an antiparallel alignment of the spins. Once the centers are separated the exchange integral becomes dominant, leading to a ferromagnetic coupling (b).

Within magnetic molecules, another mechanism determines the magnetic ground state, the so-called superexchange.

Superexchange Within organic/metal-organic systems, the exchange can be mediated through non-magnetic bridging atoms (superexchange [56]). Usually this kind of exchange results in an antiferromagnetic coupling. It occurs as soon as the involved transition metals have partially empty d-states ($d^1 - d^9$). Superexchange requires that the two species have the same occupation and that d-orbitals as well as fully occupied p-orbitals are energetically close together. As an example, two magnetic centers with a d^9 occupation are visualized in figure 2.7. For such occupations, the coupling is always antiferromagnetic. Considering other occupations ($d^1 - d^8$), different couplings can occur (see figure 2.8).

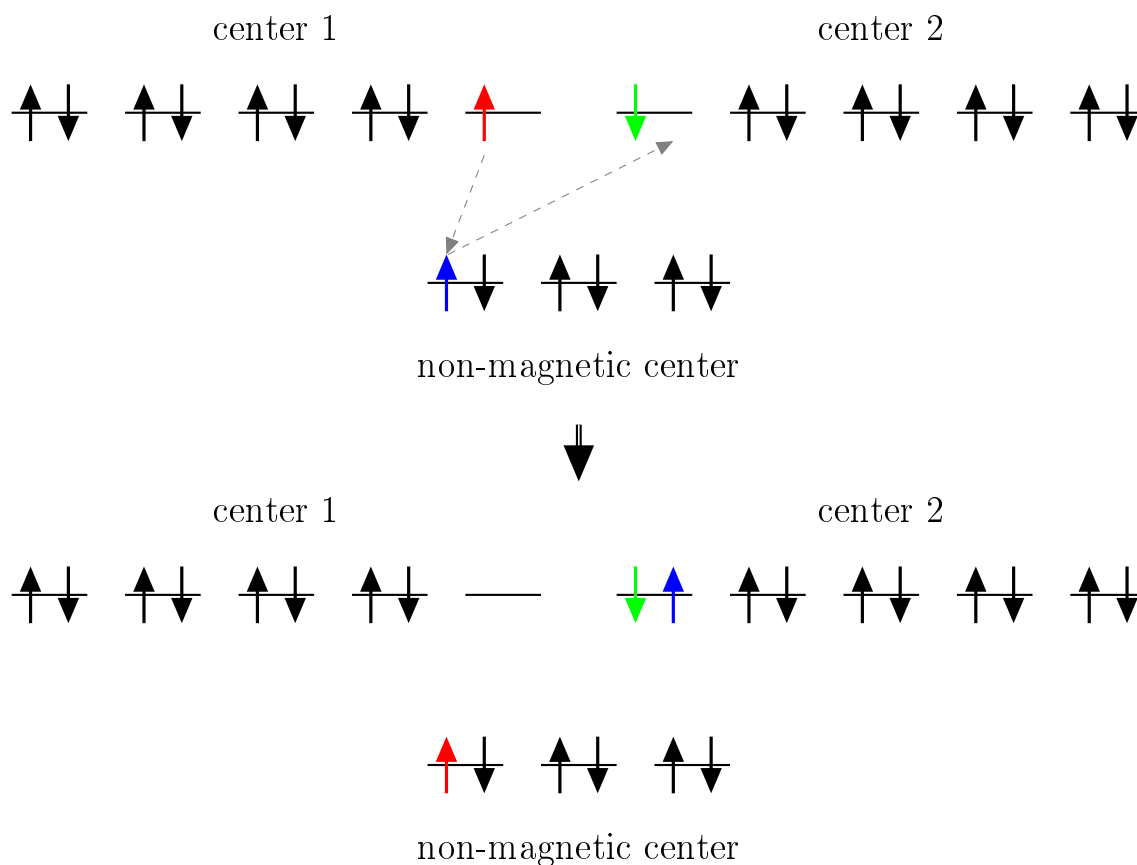


Figure 2.7.: Visualization of the superexchange for two d^9 centers with a fully occupied (non-magnetic) bridging atom. An antiferromagnetic coupling occurs.

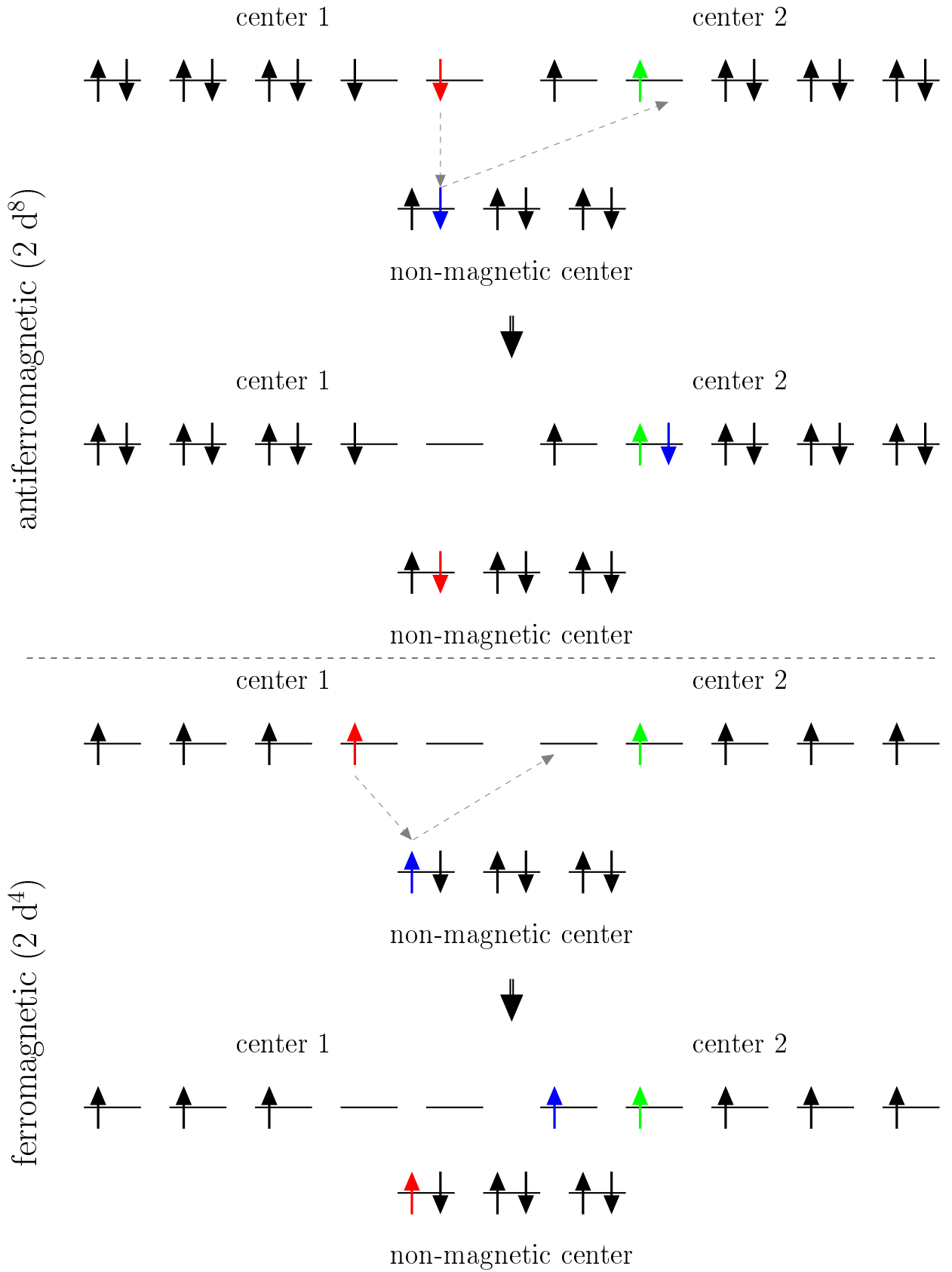


Figure 2.8.: Visualization of the superexchange for two d^8 and two d^4 centers with a fully occupied (non-magnetic) bridging atom. An antiferromagnetic and a ferromagnetic coupling occur.

Double exchange The last mechanism which shall be discussed is the so-called double exchange [57]. It occurs if the two magnetic centers obtain different valence configurations. Besides that, it is similar to the already discussed superexchange and results in a ferromagnetic coupling. The energy levels are splitted due to a crystal field (Jahn-Teller effect). From the center with more valence electrons an electron is exchanged to the center where empty orbitals are present. This only results in a ferromagnetic coupling due to Hund's first rule (maximizing the spin for a given electronic configuration) [58].

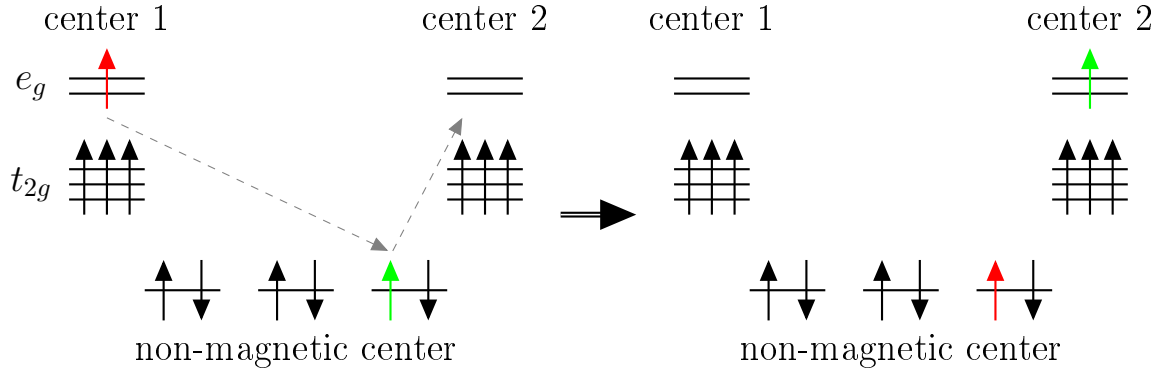


Figure 2.9.: Illustration of the double exchange between two differently occupied d-orbitals on centers 1 and 2. The levels are splitted due to an octahedral crystal field (thus the differentiation between e_g and t_{2g}). Again, the exchange is mediated by a non-magnetic p-orbital.

2.6. MAGNETIC SHIELDING

The second part of this thesis is concerned with the magnetic shielding and the chemical shift within nuclear magnetic resonance (NMR). Consequently, a brief review of the basics of NMR and an introduction into the chemical shift will be given next.

2.6.1. BASICS OF NUCLEAR MAGNETIC RESONANCE (NMR)

Nuclear magnetic resonance is a widely used technique for the determination of the structure of solids and liquids. In NMR experiments, the spin of the nucleus is of interest. A nucleus is NMR active if it is not comprised of an even number of protons and neutrons, as this would result in a nuclear spin of $I = 0$. Any further discussion will be restricted to $I = \frac{1}{2}$ particles, as those are used in later investigations (^{129}Xe).

Applying an external magnetic field \mathbf{B}_{ext} to a system leads to a splitting of the energy levels as described by the associated Zeeman energy (Zeeman effect)

$$E_{\text{Zeeman},i} = -m_i \gamma \hbar B_{\text{ext}}. \quad (2.66)$$

Here, m_i is the spin of the respective energy level, γ is the magnetogyric ratio specific for the nucleus depending on its composition ($N_{\text{proton}} + N_{\text{neutron}}$) and $B_{\text{ext}} = |\mathbf{B}_{\text{ext}}|$.

This splitting leads to $(2I + 1)$ different energy levels (multiplicity). With that, $I = 1/2$ particles are commonly investigated in NMR experiments as the Zeeman effect leads to only two different energy levels (see figure 2.10).

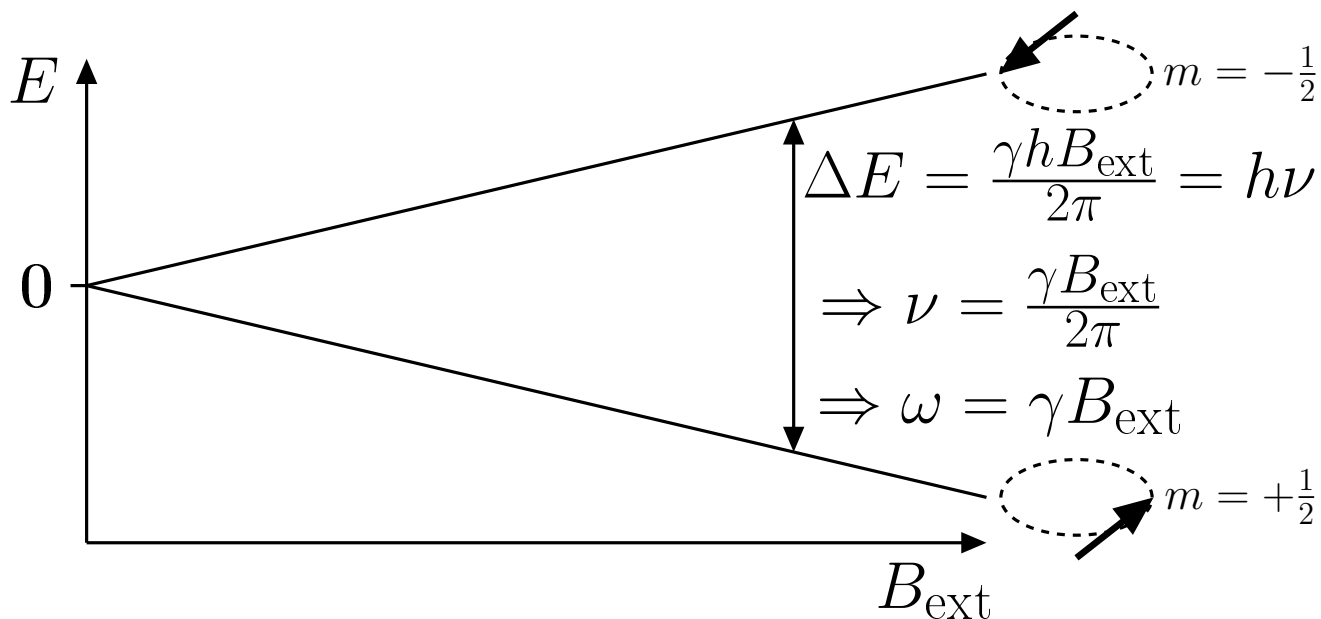


Figure 2.10.: Visualization of the energy splitting due to an applied magnetic field as described by the Zeeman effect. Additionally, the excitation energy for a $I = 1/2$ particle in the magnetic field is shown. The precession of the nuclear spins is sketched.

Due to the applied field, the nuclear spin starts precessing with a specific frequency that depends linearly on this field (the so-called the Larmor frequency ν_{Larmor}). This frequency can be excited by an applied radiation with an energy of $h\nu_{\text{Larmor}}$, where $\nu_{\text{Larmor}} = \gamma B_{\text{ext}}/(2\pi)$. Once the high energy state is excited, it will relax back to the low energy level leading to an emission of radiation. This radiation is in resonance to the applied radiation, leading to the experimentally measured NMR signal.

2.6.2. CHEMICAL SHIFT

The chemical shift is defined as a normalized change of resonance frequencies

$$\delta_i = \frac{\nu_i - \nu_{\text{ref}}}{\nu_0}, \quad (2.67)$$

with ν_i being the resonance frequency of the nucleus under observation, ν_{ref} being the resonance frequency of a reference substance for this nucleus and ν_0 being the operating frequency of the spectrometer (the frequency of the applied radiation). The chemical shift can be related to the magnetic shielding by employing the following equations

$$\begin{aligned} \mathbf{B}_{\text{ind}} &= -\sigma \mathbf{B}_{\text{ext}} \\ \mathbf{B}_{\text{tot}} &= \mathbf{B}_{\text{ext}} + \mathbf{B}_{\text{ind}} \\ &= (1 - \sigma) \mathbf{B}_{\text{ext}}, \end{aligned} \quad (2.68)$$

where \mathbf{B}_{tot} is the total field which is experienced by the nucleus due to the shielding⁸, as well as the resonance frequency

$$\nu = \frac{\gamma B_{\text{tot}}}{2\pi}. \quad (2.69)$$

The resonance frequencies of a nucleus i (ν_i) and the reference substance (ν_{ref}) can be written according to equations (2.68) and (2.69)

$$\nu_i = \frac{\gamma(1 - \sigma_i)B_{\text{ext}}}{2\pi} \quad \text{and} \quad \nu_{\text{ref}} = \frac{\gamma(1 - \sigma_{\text{ref}})B_{\text{ext}}}{2\pi}. \quad (2.70)$$

Combining those relations with equation (2.67) leads to an expression of the chemical shift

$$\begin{aligned} \delta_i &= \frac{\frac{\gamma(1-\sigma_i)B_{\text{ext}}}{2\pi} - \frac{\gamma(1-\sigma_{\text{ref}})B_{\text{ext}}}{2\pi}}{\frac{\gamma B_{\text{ext}}}{2\pi}} \\ &= \frac{((1 - \sigma_i) - (1 - \sigma_{\text{ref}}))\frac{\gamma B_{\text{ext}}}{2\pi}}{\frac{\gamma B_{\text{ext}}}{2\pi}} \\ \delta_i &= \sigma_{\text{ref}} - \sigma_i. \end{aligned} \quad (2.71)$$

For the special case of ^{129}Xe , the chemical shift can be divided into several contributions as shown by Ito and Fraissard [59] for zeolithes

$$\delta = \delta_0 + \delta_S + \delta_{\text{Xe-Xe}} + \delta_E + \delta_M + \delta_{\text{SAS}}, \quad (2.72)$$

with δ being the total shift of the Xe, δ_0 being a reference signal at zero pressure (which corresponds to the shielding of an isolated Xe atom), δ_S being the shift due to Xe-surface interactions (which is especially important in MOFs), $\delta_{\text{Xe-Xe}}$ being the shift due to Xe-Xe interactions, δ_E and δ_M being influences of electric and magnetic fields induced by surrounding ions and δ_{SAS} being the shift due to strong absorption sites. In this thesis, this equation can be simplified. Firstly one can neglect δ_E and δ_M , as there are no surrounding ions in the system, only Xe ($\delta_E = \delta_M = 0$). Further, δ_{SAS} can be included into δ_S to collectively describe all surface effects. Those simplifications lead to

$$\delta = \delta_0 + \delta_S + \delta_{\text{Xe-Xe}}. \quad (2.73)$$

The reference δ_0 has to be determined only once. Afterwards, the calculated shielding contributions will be referred to this value to evaluate the chemical shift (see equation (2.71)). With that, the Xe chemical shift as given by Xe-surface and Xe-Xe interactions has to be analyzed. The corresponding shielding values can be extracted using model systems as shown in section 4.3.

⁸ In further discussion, only the isotropic shielding is considered, thus $\sigma = \frac{1}{3}(\sigma_{11} + \sigma_{22} + \sigma_{33})$.

2.7. COMPUTATIONAL DETAILS

Quantum ESPRESSO Quantum ESPRESSO (opEn Source Package for Research in Electronic Structure, Simulation and Optimization) (QE) offers a large variety of possibilities to calculate properties of systems using pseudopotentials [3]. The employed plane wave basis set enables the treatment of periodic boundary conditions of systems with several hundred atoms. In detail, QE allows the calculation of total energies, the electronic density of states and can be further used for geometry optimizations.

For all calculations, the projector-augmented wave (PAW) method [49] was used (labelled [element].pbe-[spn]-kjpaw_psl.0.[1,2,3].[1,3].UPF, for more information see www.theo.srv1.epfl.ch/Main/Pseudopotentials). A kinetic energy cutoff of 90 Ry for the crystal structures of DUT-8(Ni) and 150 Ry for the respective model systems was used. The kinetic energy cutoff was adjusted to 80 Ry for the calculations of UiO-66 and UiO-67. For position and cell optimizations, the forces were reduced such that the differences were smaller than 10^{-6} Ry/ $a_0 \approx 2.57 \cdot 10^{-5}$ eV/Å. All reported values have been computed with QE if not stated otherwise.

Convergence test calculations concerning different numerical parameters were performed (see Appendix 3).

FPLO Additional calculations have been carried out with FPLO, a full potential local orbital [4] program. This allowed an evaluation of the pseudopotential treatment within QE using an all-electron treatment. FPLO uses a minimum basis set [4, 60].

SIESTA The molecular dynamics simulations within this thesis were performed with SIESTA [61]. It uses local orbitals within a small basis set and pseudopotentials. This makes it very suitable for the calculation of large systems (e.g. zeolites, MOFs, etc.) within reasonable computational effort.

XCrySDen X-window CRYstalline Structures and DENsities (XCrySDen) [62] has been used for the visualization of all structures (finite or periodic systems). Additionally, XcrySDen can read QE output files, which allows a straightforward display of many properties of interest (e.g. charge densities or structural changes during optimization).



PART III.

ELECTRONIC MAGNETISM IN DUT-8(NI)

3.1. STRUCTURAL CONSIDERATIONS

For structural considerations of DUT-8(Ni), optimizations of the atomic positions and the unit cell have been carried out. This ensures a consistent treatment of the systems considering the geometry as obtained in the used theoretical framework.

Additionally, one can evaluate any property for the unrelaxed (initial) structures as well as for the fully optimized ones. This will show how sensible the properties are to a given geometry. All optimizations included vdW corrections [2]. For DUT-8(Ni)_{open} two optimizations were carried out, where in one of them the angles of the unit cell were fixed to 90° (labelled Opt1, leaving the orthogonal geometry unchanged) while for the other one even the angles were allowed to change (labelled Opt2). After full geometry optimization of the initial structures, the unit cell vectors are described as follows

Opt1 DUT-8(Ni)_{open}:

$$\mathbf{a} = \begin{pmatrix} 18.66489 \\ 0.00000 \\ 0.00000 \end{pmatrix} \text{Å}, \mathbf{b} = \begin{pmatrix} 0.00000 \\ 18.41702 \\ 0.00000 \end{pmatrix} \text{Å}, \mathbf{c} = \begin{pmatrix} 0.00000 \\ 0.00000 \\ 9.16186 \end{pmatrix} \text{Å}.$$

Opt2 DUT-8(Ni)_{open}:

$$\mathbf{a} = \begin{pmatrix} 18.66123 \\ 0.00507 \\ 0.00352 \end{pmatrix} \text{Å}, \mathbf{b} = \begin{pmatrix} 0.00500 \\ 18.42435 \\ 0.00141 \end{pmatrix} \text{Å}, \mathbf{c} = \begin{pmatrix} 0.00175 \\ 0.00198 \\ 9.16385 \end{pmatrix} \text{Å}$$

Opt2 DUT-8(Ni)_{closed}:

$$\mathbf{a} = \begin{pmatrix} 6.66853 \\ 0.20297 \\ 0.10428 \end{pmatrix} \text{Å}, \mathbf{b} = \begin{pmatrix} -1.75441 \\ 7.57483 \\ 0.12651 \end{pmatrix} \text{Å}, \mathbf{c} = \begin{pmatrix} -2.68189 \\ -0.81445 \\ 11.82161 \end{pmatrix} \text{Å}$$

Table 3.1.: Cell parameters obtained from geometry optimization of the two phases of DUT-8(Ni).

		a [Å]	b [Å]	c [Å]	α [°]	β [°]	γ [°]
DUT-8(Ni) _{open}	Opt1	18.665	18.417	9.162	90	90	90
	Opt2	18.661	18.424	9.164	89.983	89.978	89.969
	initial	18.676	18.676	9.613	90	90	90
	exp [26]	18.431	18.431	9.391	90	90	90
DUT-8(Ni) _{closed}	Opt2	6.672	7.776	12.149	89.981	101.973	101.279
	initial	6.947	8.181	12.172	91.141	103.871	104.551
	exp [26]	6.947	8.181	12.172	91.141	103.871	104.551

For further discussions, Opt2 will be referred to as 'DUT-8(Ni)_{open,vc}' and 'DUT-(Ni)_{closed,vc}' for the respective structures of DUT-8(Ni) (vc stands for variable cell optimization). Further investigations including the calculation of the binding energies of all structures are summarized in Appendix 4.

In all optimizations, a contraction of the cell along the Ni-Ni axis occurs, resulting in a reduced Ni-Ni distance compared to the initial structures (along \mathbf{c} for DUT-8(Ni)_{open} and mainly along \mathbf{a} and \mathbf{b} for DUT-8(Ni)_{closed}). Based on this observation, model systems for both (initial, optimized) structures were generated. This allows to analyze the influence of different Ni-Ni distances on the magnetic properties using significantly less computational resources (see section 3.5). The contraction could be lifted in DUT-8(Ni)_{open}, as this structure only stabilizes upon adsorption. Any adsorbed species might apply a certain stress to the system, which could increase the Ni-Ni distance and the unit cell volume [26]. Thus, the obtained values in this thesis will serve as a theoretical limit.

3.2. ELECTRONIC STRUCTURE - DENSITY OF STATES

Considerations of the electronic structure can be based on the electronic density of states (DOS). The density of states is given by

$$\text{DOS}(\epsilon) \sim \sum_{n,\mathbf{k}} \delta(\epsilon - \epsilon_{n,\mathbf{k}}). \quad (3.1)$$

Here, n runs over all KS-orbitals in the considered energy range and \mathbf{k} represents a reciprocal space vectors at which the energy is evaluated. Additionally, by using a projection on the atoms and their corresponding KS-wave functions, a partial DOS (PDOS) can indicate the contribution of any orbital (s,p,d character) to the energy levels. This allows a qualitative analysis of the respective contributions especially considering two spin densities, one for spin up (\uparrow) and one for spin down (\downarrow). Taking the definition of the spin-polarization (see equation (2.27)), different magnetic orderings can be distinguished considering the DOS.

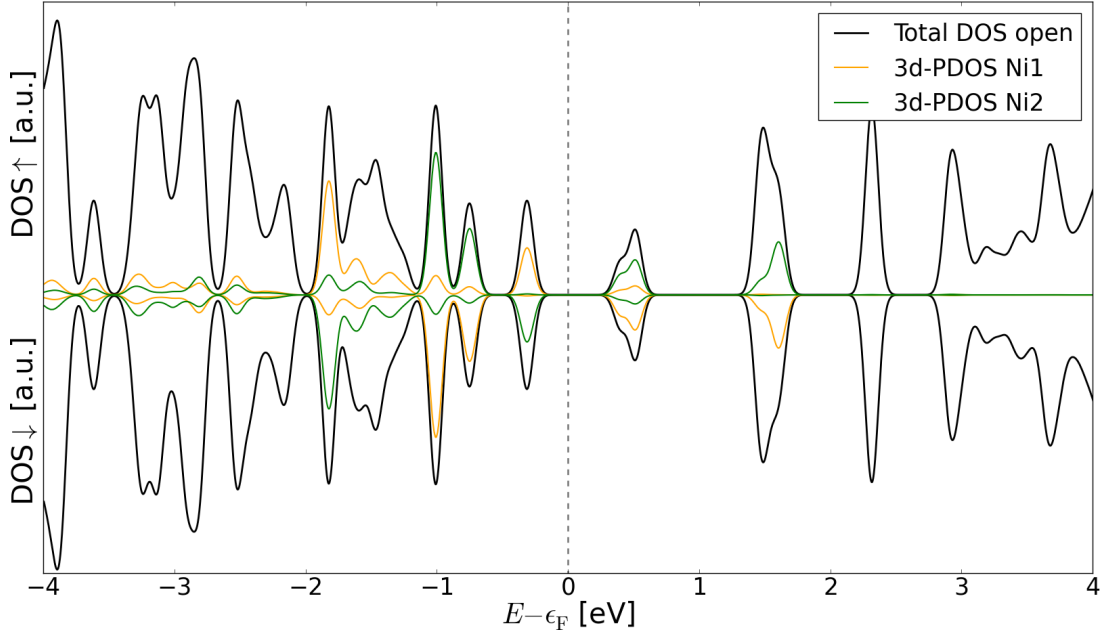
For closed shell systems, there is no differentiation between spin up and spin down electrons, i.e. energy levels are occupied by electrons of both spins originating at the same atoms. This leads to a spin-polarization of zero, and no magnetic interaction occurs.

On the other hand, for an open shell system the situation changes. Considering an antiferromagnetic (low-spin) ordering, \uparrow - and \downarrow -electrons will occupy states at the same energies. Again, the spin-polarization becomes zero. However, in contrast to a closed shell system not all \uparrow - and \downarrow -electrons are localized at the same atom. Thus, unpaired electrons at different centers occur. For the antiferromagnetic case an antiparallel alignment of the spins is present, which can be seen in the DOS as well.

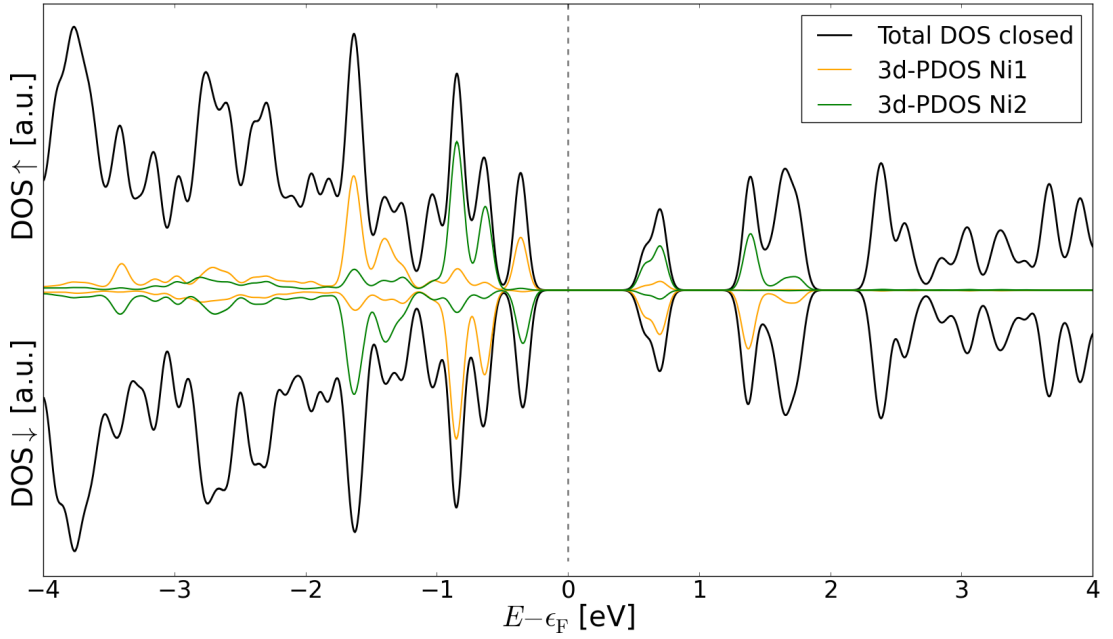
For a ferromagnetic (high-spin) ordering, the occupation of energy levels can be different for \uparrow - and \downarrow -electrons, leading to a non-zero spin-polarization.

In figure 3.1 (a) and 3.1 (b) the total DOS for DUT-8(Ni)_{open/closed,vc} are displayed. In addition to the total DOS, the PDOS for the Ni 3d-states (for each individual Ni) are shown⁹. The energy levels around the Fermi level are clearly dominated by Ni 3d-states. Furthermore, the d-electrons of the two different Ni atoms occupy the same energy levels for \uparrow and \downarrow , indicating an antiferromagnetic behavior.

⁹ For DUT-8(Ni)_{open}, two Ni dimers per unit cell are present. In the DOS, the sum of the first (Ni1) and the second Ni (Ni2) is displayed.



(a) DUT-8(Ni)_{open,vc}



(b) DUT-8(Ni)_{closed,vc}

Figure 3.1.: Density of states for DUT-8(Ni)_{open/closed,vc}.

The spin up DOS is given in the upper half of each figure while the spin down DOS is displayed in the lower half. The partial DOS for the Ni 3d-states (for each Ni) is presented, clearly indicating that the d-electrons dominate the energy levels around the Fermi level ϵ_F . Further, spin up and spin down electrons occupy levels at the same energy, indicating an antiferromagnetic (low-spin) ordering.

3.3. MAGNETIC GROUND STATE INVESTIGATIONS

To analyze the magnetic ground state of a system, total energies corresponding to different magnetic orderings have to be calculated. This was done with spin-polarized KS-DFT. As already explained in section 2.5.1, the magnetic behavior can be characterized by the coupling constant J_{ij} .

It should be considered that DUT-8(Ni)_{open} contains two Ni-dimer SBUs in one unit cell. As the SBUs are well separated by organic linkers, they can be treated independently (see supercell calculations in section 3.4 or model calculation in section 3.5.3). Given this fact, the coupling constant scales linearly with the number of Ni-dimers per unit cell N_{SBU} . Thus, equation (2.57) has to be adjusted to

$$J_{ij} = \frac{\Delta E'}{[\langle \mathbf{S}_{\text{tot}}^2 \rangle_{\text{HS}} - \langle \mathbf{S}_{\text{tot}}^2 \rangle_{\text{LS}}]} \cdot \frac{1}{N_{\text{SBU}}}. \quad (3.2)$$

The results of spin-polarized calculations of the crystal systems are given in table 3.2 (for the initial geometries) and table 3.3 (for the optimized geometries). In those tables, M_{tot} is the total magnetization (given by $\int (n^\uparrow - n^\downarrow) d^3r$) corresponding to the spin-polarization of the entire system while M_{abs} is the absolute magnetization (given by $\int |n^\uparrow - n^\downarrow| d^3r$) referring to the sum of spin-polarizations per atom.

Table 3.2.: Results for spin polarized calculations of the two crystal structures of DUT-8(Ni) in their initial geometries [12].

Parameter	DUT-8(Ni) _{open,init}		DUT-8(Ni) _{closed,init}	
	high-spin	low-spin	high-spin	low-spin
E_{tot} [Ry]	-2685.1016	-2685.1308	-1341.9985	-1342.0044
M_{tot} [μ_{B} /cell]	8.00	0.00	4.00	0.00
M_{abs} [μ_{B} /cell]	8.26	7.47	4.15	3.70
J_{ij} [cm^{-1}]	-267.4 (low-spin)		-108.4 (low-spin)	

Table 3.3.: Results for spin polarized calculations of the two crystal structures of DUT-8(Ni) in their optimized geometries.

Parameter	DUT-8(Ni) _{open,vc}		DUT-8(Ni) _{closed,vc}	
	high-spin	low-spin	high-spin	low-spin
E_{tot} [Ry]	-2685.6353	-2685.6612	-1342.8502	-1342.8671
M_{tot} [μ_{B} /cell]	4.00	0.00	2.00	0.00
M_{abs} [μ_{B} /cell]	4.53	6.29	2.38	3.28
J_{ij} [cm^{-1}]	-316.1 (low-spin)		-411.6 (low-spin)	

For the initial geometries, negative coupling constants and correspondingly a low-spin coupling between the Ni atoms is found. The coupling constant is larger for the open structure in comparison to the closed one. Considering the geometries, the two Ni atoms within the SBU are well separated ($d_{\text{Ni-Ni,open,init}} = 2.806 \text{ \AA}$ and $d_{\text{Ni-Ni,closed,init}} = 2.736 \text{ \AA}$). Taking into account that in $\text{DUT-8(Ni)}_{\text{closed,init}}$ the chemical environments for the two Ni atoms are different (regarding the Ni-O and Ni-N distances), a decrease of the magnetic interaction occurs. This can be seen from the absolute magnetizations in the favourable low-spin magnetic ordering as well. In $\text{DUT-8(Ni)}_{\text{open,init}}$ this quantity becomes larger, thus a stronger magnetic interaction occurs. Furthermore, the spin densities in $\text{DUT-8(Ni)}_{\text{closed,init}}$ are extended onto the organic linkers (as shown in Appendix 7). Thus, a strict localization is not given anymore, leading to a decrease of J_{ij} .

Regarding the optimized structures, negative coupling constants are obtained as well. A difference to the initial structures is the absolute magnetization in the high-spin state. For the initial geometries $M_{\text{abs}} \approx 4 \mu_{\text{B}}$ is obtained, while in the optimized geometries this value becomes $M_{\text{abs}} \approx 2 \mu_{\text{B}}$. This might be attributed to a possible bond formation between the Ni centers due to the reduced Ni-Ni distances ($d_{\text{Ni-Ni,open,vc}} = 2.386 \text{ \AA}$ and $d_{\text{Ni-Ni,open,vc}} = 2.478 \text{ \AA}$). Thus, the absolute values of the coupling constants can hardly be compared quantitatively.

However, in this section the energy differences between the low-spin and the high-spin state shall be analyzed. For $\text{DUT-8(Ni)}_{\text{open,init}}$, this energy difference is larger in comparison to $\text{DUT-8(Ni)}_{\text{open,vc}}$. An explanation of this behavior can again be based on the absolute magnetizations. This quantity becomes smaller in $\text{DUT-8(Ni)}_{\text{open,vc}}$. Therefore, a smaller energy difference occurs due to the reduced magnetic interaction between the Ni centers.

Further explanation can be found considering the localization of the spin densities. Within $\text{DUT-8(Ni)}_{\text{open,init}}$, such densities are localized on the Ni centers¹⁰. On the other hand for $\text{DUT-8(Ni)}_{\text{open,vc}}$, a significant spread of the spin densities over all adjacent linkers occurs (see Appendix 7). Thus, a clear distinction between the high-spin and the low-spin state is not provided anymore. Additionally, the smaller absolute magnetization is another result of this spread. Furthermore, the concept of the Heisenberg-Dirac-Van Vleck Hamiltonian (see section 2.5.1) does not apply anymore, as localized spin centers are required. With that, the coupling constant for this geometry should be considered as a limiting case.

As mentioned before, the spin densities in $\text{DUT-8(Ni)}_{\text{closed,init}}$ are not fully localized on the Ni centers. In contrast, such densities are fairly localized in $\text{DUT-8(Ni)}_{\text{closed,vc}}$. As a result, the coupling constant as well as the energy difference is larger for $\text{DUT-8(Ni)}_{\text{closed,vc}}$. However, the absolute magnetization is smaller in comparison to the initial structures, which is another consequence of the smaller Ni-Ni distance. Comparing the geometries of the two structures, rather large differences can be found. The two Ni centers in the optimized structure have the same chemical environment (i.e. the Ni-O and Ni-N distances are the same in the optimized structure). This is in contrast to the initial structure of $\text{DUT-8(Ni)}_{\text{closed}}$, where the chemical environment is different for the two Ni centers. Thus, the magnetic interaction for the optimized structure is stronger. Interestingly, the energy difference between the high-spin and the low-spin state in $\text{DUT-8(Ni)}_{\text{closed,vc}}$ is the largest for all considered geometries. This is reflected in the strongest magnetic interaction considering J_{ij} . Consequently, for some model system calculations, only models derived from this structure have been used (see section 3.5.2 and 3.5.3).

¹⁰ Localization in this context is used such that the spin densities which contribute to the magnetic interaction are only found at the Ni atoms.

In summary, the low-spin state in all considered geometries is favourable. Taking these considerations into account, model systems (section 3.5) were derived from the initial as well as from the fully optimized structures. This ensures a thorough analysis of the magnetic properties with respect to different Ni-Ni distances. Furthermore, the model systems require significantly less computational time and can be easily modified.

3.4. SUPERCELL CALCULATIONS

As presented in the last section, the calculations on the single unit cells reveal a low-spin ordering in both crystal phases. However, those calculations only included a description of the magnetic coupling between the same unit cell. An appropriate analysis of the magnetic interaction between different unit cells is carried out using a supercell approach. For this purpose, supercells for DUT-8(Ni)_{open,vc} and DUT-8(Ni)_{closed,vc} have been generated such that there are four SBUs per supercell (as depicted in figure 3.2).

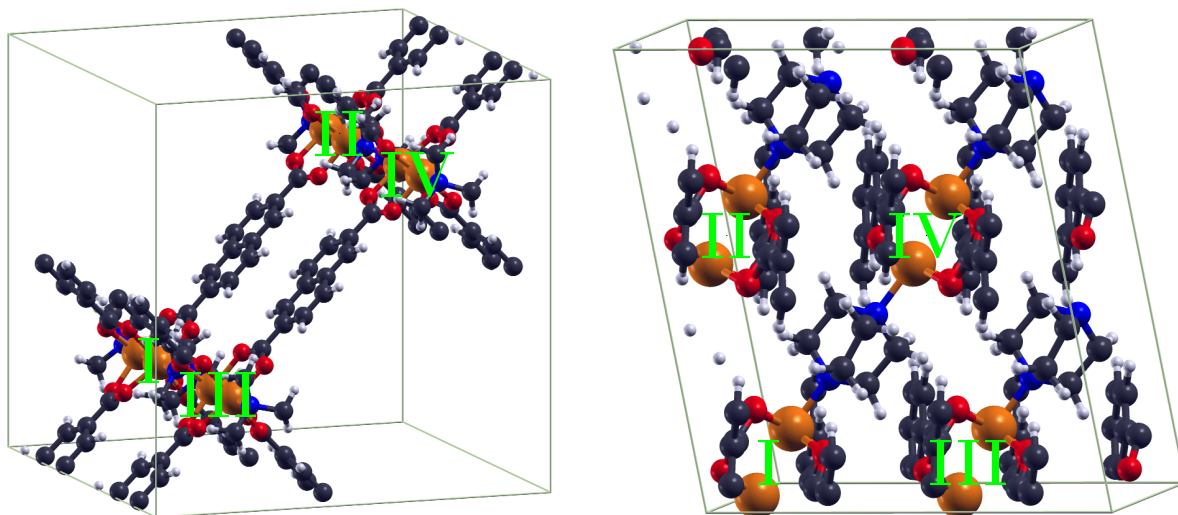


Figure 3.2.: The supercells for DUT-8(Ni)_{open,vc} and DUT-8(Ni)_{closed,vc} to imply different magnetic orderings. The Ni dimers as magnetic units are highlighted (see table 3.4 as well).

This ansatz does not treat the coupling along the carbon rings within DUT-8(Ni)_{closed,vc}. However, considering the length of such linkers, the magnetic coupling along them becomes negligible. Different magnetic orderings within the supercells have been employed. An explicit description of the orderings is given in table 3.4¹¹.

The results of the supercell calculations confirm the discussion from the previous section, i.e. a local LS coupling within the SBU is the most favourable magnetic ordering (see table 3.4). Additionally, the supercell calculations were used to analyze the global magnetic ordering when the local ordering is HS. From these investigations it can be concluded that a global HS arrangement between SBUs, which are interconnected along the dabco units, is more favourable. This behavior is e.g. found for DUT-8(Ni)_{closed,vc} (compare global HS, $S = 2$ and global LS). Thus, if the local order is HS, a global order would be HS (at least in the case of a Ni SBU in DUT-8(Ni)_{closed,vc}). More detailed investigations considering long-range magnetic interactions were carried out, see section 3.5.3.

¹¹ Investigations for the initial structures can be found in Appendix 5. Similar results were obtained.

Table 3.4.: Results for supercell calculations for $\text{DUT-8(Ni)}_{\text{open,vc}}$ and $\text{DUT-8(Ni)}_{\text{closed,vc}}$. The magnetic dimer units **I**, **II**, **III** and **IV** refer to the indication in figure 3.2. \uparrow and \downarrow stand for the spins at a specific Ni atom per SBU. M_{tot} denotes the total magnetization while M_{abs} stands for the absolute magnetization. Additionally, **low** describes a local low-spin ordering, **up** refers to a local high-spin with two \uparrow and **dn** corresponds to a local high-spin with two \downarrow . Different magnetic orderings were compared using $\Delta E_{\text{tot-LS(local)}} = E_{\text{tot}} - E_{\text{LS(local)}}$.

global	type	I	II	III	IV	M_{tot} [μ_{B} /cell]	M_{abs} [μ_{B} /cell]	$\Delta E_{\text{tot-LS(local)}}$ [meV/dimer]
$\text{DUT-8(Ni)}_{\text{open,vc}}$								
LS	I,II,III,IV_{low}	$\uparrow\downarrow$	$\uparrow\downarrow$	$\uparrow\downarrow$	$\uparrow\downarrow$	0.00	12.59	0.00
	I,II,III,IV_{low,2}	$\uparrow\downarrow$	$\uparrow\downarrow$	$\downarrow\uparrow$	$\downarrow\uparrow$	0.00	12.61	3.29
	I-IV_{up} II-III_{dn}	$\uparrow\uparrow$	$\downarrow\downarrow$	$\downarrow\downarrow$	$\uparrow\uparrow$	0.00	8.93	203.84
	I-III_{up} II-IV_{dn}	$\uparrow\uparrow$	$\downarrow\downarrow$	$\uparrow\uparrow$	$\downarrow\downarrow$	n/a	n/a	n/a
HS, $S = 4$	I,II,III,IV_{up}	$\uparrow\uparrow$	$\uparrow\uparrow$	$\uparrow\uparrow$	$\uparrow\uparrow$	n/a	n/a	n/a
$\text{DUT-8(Ni)}_{\text{closed,vc}}$								
LS	I,II,III,IV_{low}	$\uparrow\downarrow$	$\uparrow\downarrow$	$\uparrow\downarrow$	$\uparrow\downarrow$	0.00	13.11	0.00
	I,II,III,IV_{low,2}	$\uparrow\downarrow$	$\uparrow\downarrow$	$\downarrow\uparrow$	$\downarrow\uparrow$	0.00	13.14	7.42
	I,IV_{up} II,III_{dn}	$\uparrow\uparrow$	$\downarrow\downarrow$	$\downarrow\downarrow$	$\uparrow\uparrow$	n/a	n/a	n/a
	I,II_{up} III,IV_{dn}	$\uparrow\uparrow$	$\uparrow\uparrow$	$\downarrow\downarrow$	$\downarrow\downarrow$	0.00	15.40	362.50
	I,III_{up} II,IV_{dn}	$\uparrow\uparrow$	$\downarrow\downarrow$	$\uparrow\uparrow$	$\downarrow\downarrow$	0.00	15.41	362.58
	I,II_{low} III_{up}, IV_{dn}	$\uparrow\downarrow$	$\uparrow\downarrow$	$\uparrow\uparrow$	$\downarrow\downarrow$	0.00	14.68	233.53
	I,III_{low} II_{up}, IV_{dn}	$\uparrow\downarrow$	$\uparrow\uparrow$	$\uparrow\downarrow$	$\downarrow\downarrow$	0.00	14.68	233.47
	I,IV_{low} II_{up}, III_{dn}	$\uparrow\downarrow$	$\uparrow\uparrow$	$\downarrow\downarrow$	$\uparrow\downarrow$	0.00	14.26	218.38
HS, $S = 2$	I,II,IV_{dn} III_{up}	$\downarrow\downarrow$	$\downarrow\downarrow$	$\uparrow\uparrow$	$\downarrow\downarrow$	n/a	n/a	n/a
	I,II_{low} III,IV_{up}	$\uparrow\downarrow$	$\uparrow\downarrow$	$\uparrow\uparrow$	$\uparrow\uparrow$	4.00	11.34	151.81
	I,III_{low} II,IV_{up}	$\uparrow\downarrow$	$\uparrow\uparrow$	$\uparrow\downarrow$	$\uparrow\uparrow$	4.00	11.35	151.81
	I,IV_{low} II,III_{up}	$\uparrow\downarrow$	$\uparrow\uparrow$	$\uparrow\uparrow$	$\uparrow\downarrow$	4.00	11.17	151.09
HS, $S = 4$	I,II,III,IV_{up}	$\uparrow\uparrow$	$\uparrow\uparrow$	$\uparrow\uparrow$	$\uparrow\uparrow$	8.00	9.25	264.88
HS, $S = 8$	I,II,III,IV_{up}	$\uparrow\uparrow$	$\uparrow\uparrow$	$\uparrow\uparrow$	$\uparrow\uparrow$	16.00	16.47	400.98

3.5. MODEL SYSTEMS

As MOFs tend to have rather big unit cells with a large number of atoms, DFT becomes quite demanding from a computational point of view. With that, it is desirable to reduce the computational time while preserving the quality of the results to a large extent. One ansatz to achieve this goal are molecular model systems. Such systems contain less atoms than the original structure and are therefore easier to handle. Additionally, these systems can be easily modified and effects of such modifications can be studied (see figure 3.3).

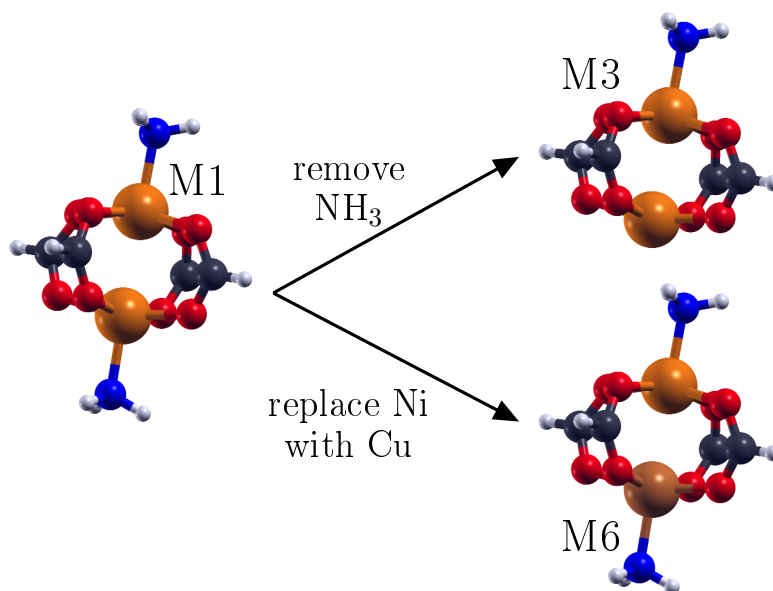


Figure 3.3.: Initial model system (M1) and examples for two modifications, leading to new models (M3, M6). All models are shown in figure 3.4.

As the focus of this work is the electronic magnetism of MOFs and this magnetism is localized on the SBUs, molecular models can be extracted from the crystal structures. For this purpose, the SBU has been cut from the periodic structures. With that, a system that contains only the two Ni atoms and their respective chemical environment (four oxygen atoms, connected with a carbon atom, and one nitrogen atom each) is obtained. All other structural details of the periodic systems are neglected. To ensure charge neutrality and saturate free bonds, the carbon atoms as well as the nitrogen atoms have been saturated with hydrogen, see figure 3.3. This reduces the amount of atoms drastically (132 atoms per unit cell in $\text{DUT-8(Ni)}_{\text{open}}$ to 26 atoms in the initial model system). In addition, the molecular models are finite systems and can be treated without the need of periodic boundary conditions.

Those models not only allow the study of the magnetic properties in a faster manner, but additionally provide the possibility to easily analyze the resulting coupling constant upon structural changes. Furthermore, the metal centers themselves can be exchanged with other 3d-metals to analyze the alterations of the magnetic behavior. This might enable the prediction of new MOFs based on the original structure of DUT-8(Ni) with potential high-spin magnetic characteristics.

To analyze how alterations of the chemical environment affect the magnetic coupling of the Ni atoms, several changes have been implied (see table 3.5 and figure 3.4).

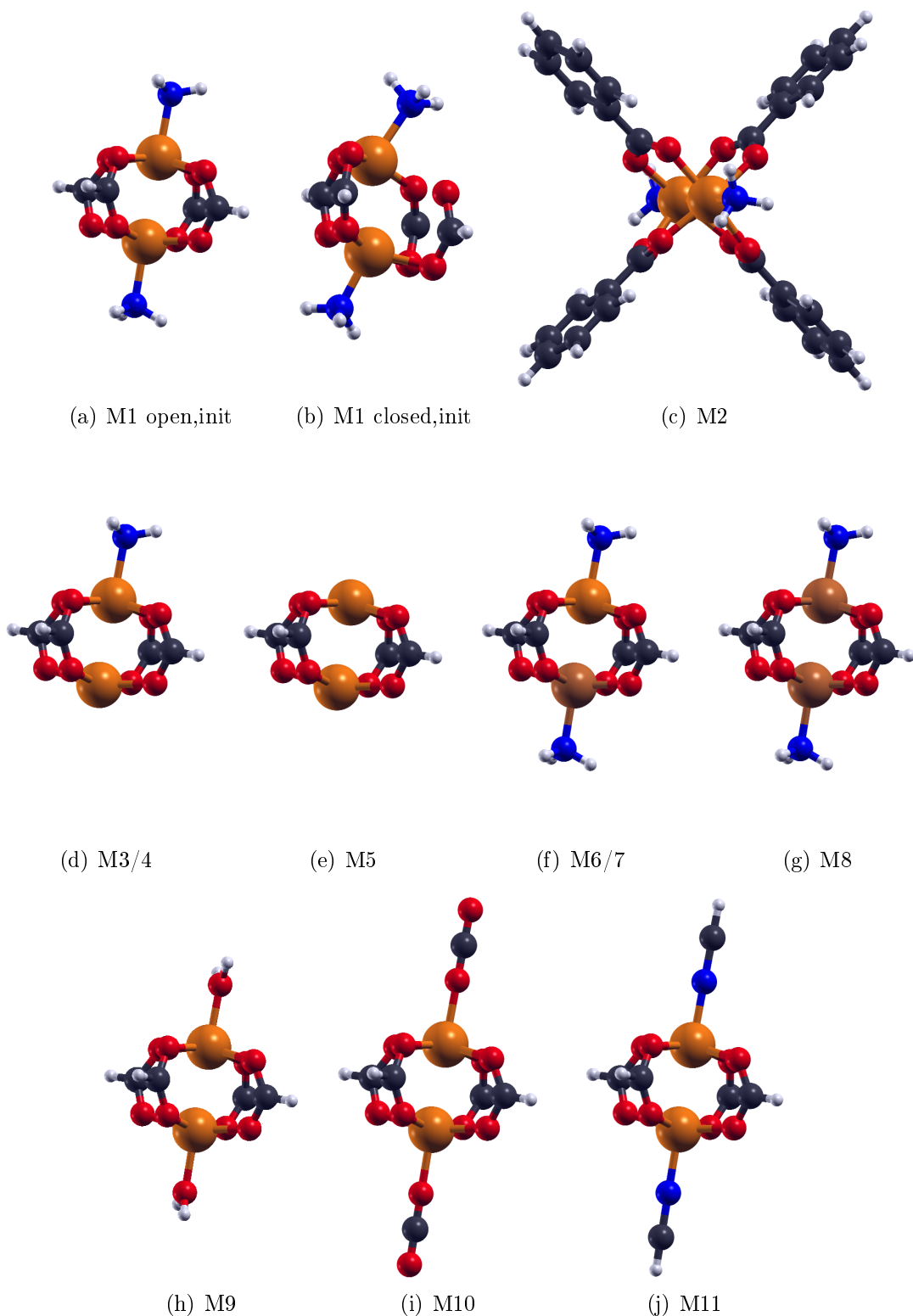


Figure 3.4.: Geometries of the model systems for the investigations of the magnetic behavior of DUT-8(Ni).

The initial model M1 is shown for DUT-8(Ni)_{open,init} (a) and DUT-8(Ni)_{closed,init} (b), while all other models (M2 - M12) are only shown for DUT-8(Ni)_{open,init}. For M2, the carbon rings of the linkers have been added. The removal of one or two NH₃ groups was studied with M3, M4 and M5. An exchange of Ni with Cu was analyzed using M6, M7 and M8. Other functional groups replacing NH₃ were investigated with M9, M10, M11 (corresponding to H₂O, CO₂ and HCN).

Table 3.5.: Alterations of the model systems to study different chemical environments.

Label	initial unit/atom	changed unit/atom
M1	none	none
M2	C-H	C-Phenyl
M3	only first NH ₃	removed
M4	only second NH ₃	removed
M5	both NH ₃	removed
M6	only first Ni	Cu
M7	only second Ni	Cu
M8	both Ni	Cu
M9	NH ₃	OH ₂
M10	NH ₃	OCO
M11	NH ₃	NCH

The model systems only work if the magnetism is localized on the metal centers. This was ensured not only with the supercell calculations discussed in the previous section, but by calculations on further model systems analyzing the magnetic behavior along the dabco units (see section 3.5.3).

3.5.1. INFLUENCE OF CHEMICAL ENVIRONMENTS ON J_{ij}

The model systems as introduced in the previous section have been investigated regarding their coupling constants. To confirm the results from QE, all spin-polarized calculations have been performed with FPLO as well. This allows a comparison between the resulting coupling constant based on an all-electron calculation and a pseudopotential calculation. Thus, the accuracy of the QE calculations to describe J_{ij} can be analyzed. As seen in tables 3.6 and 3.7, the agreement between the pseudopotential and the all-electron results is very good.

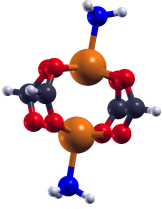
All obtained values for the model systems can be found in Appendix 6.

Table 3.6.: Resulting coupling constants for the model systems as derived from the initial (unrelaxed) structures of DUT-8(Ni).

Model	DUT-8(Ni) _{open,init}		DUT-8(Ni) _{closed,init}	
	J_{QE} [cm ⁻¹]	J_{FPLO} [cm ⁻¹]	J_{QE} [cm ⁻¹]	J_{FPLO} [cm ⁻¹]
M1	-272.2	-274.8	-70.2	-58.6
M2	-254.8	-257.9	-58.9	-45.7
M3	+383.6	+486.7	+269.1	+289.7
M4	+388.2	+502.2	-5.7	+10.7
M5	+722.1	+1050.9	+346.7	+368.6
M6	-247.9	-243.6	+1.8	-5.3
M7	-242.5	-237.7	-104.6	-101.9
M8	-517.6	-496.4	-69.5	-37.5
M9	+121.7	+156.8	+38.3	+94.6
M10	+540.5	+621.6	+379.0	+459.3
M11	+620.7	+694.1	+434.1	+465.2

Table 3.7.: Resulting coupling constants for the model systems as derived from the fully optimized structures of DUT-8(Ni).

Model	DUT-8(Ni) _{open,vc}		DUT-8(Ni) _{closed,vc}	
	J_{QE} [cm^{-1}]	J_{FPLO} [cm^{-1}]	J_{QE} [cm^{-1}]	J_{FPLO} [cm^{-1}]
M1	-68.8	-60.5	-382.3	-364.1
M2	-121.7	-142.2	-424.4	-414.2
M3	+948.6	+936.0	+621.5	+632.9
M4	+954.9	+922.3	+610.9	+621.3
M5	—	—	—	—
M6	-244.7	-240.1	+63.3	+60.0
M7	-239.5	-235.0	+61.5	+61.6
M8	-425.4	—	-97.6	-89.6
M9	+672.2	+689.4	+162.1	+194.8
M10	—	—	+694.2	—
M11	+1071.2	—	—	—



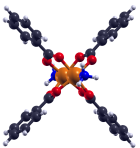
The initial model system (M1) was used as the starting point for all further investigations. This model needs to reproduce the magnetic properties of the crystal structures. As can be seen from table 3.6 and 3.7, the coupling constants of the model systems are in good agreement with the respective values in the crystal structures

$$\text{DUT-8(Ni)}_{\text{open,init}}: J_{\text{crystal}} = -267 \text{ cm}^{-1} \text{ and } J_{\text{M1}} = -272 \text{ cm}^{-1}$$

$$\text{DUT-8(Ni)}_{\text{closed,init}}: J_{\text{crystal}} = -108 \text{ cm}^{-1} \text{ and } J_{\text{M1}} = -70 \text{ cm}^{-1}$$

$$\text{DUT-8(Ni)}_{\text{closed,vc}}: J_{\text{crystal}} = -412 \text{ cm}^{-1} \text{ and } J_{\text{M1}} = -382 \text{ cm}^{-1}.$$

Only for DUT-8(Ni)_{open,vc}, these values differ ($J_{\text{crystal}} = -316 \text{ cm}^{-1}$ and $J_{\text{M1}} = -69 \text{ cm}^{-1}$). This might be the consequence of the very small Ni-Ni distance, which is further analyzed in Appendix 7. This additional analysis shows that the model system ansatz works in general. Only for very small metal-metal distances, the ansatz fails due to an extension of the spin densities onto the adjacent linkers¹². Consequently, the removal of the adjacent linkers leads to an inaccurate description of the magnetic coupling. However, the ansatz works well for Ni-Ni distances larger than 2.47 Å. With that, the models from DUT-8(Ni)_{open,vc} are considered as a limiting case. Accordingly, all further values presented for this model system must be viewed with caution. Because it qualitatively represents the correct magnetic behavior, further investigations were carried out for this model as well. In summary, for all other systems the M1 model represents the magnetic coupling of the crystal structures and additionally shows that the magnetism is localized on single SBUs.



The M1 model was extended by the carbon rings of the linkers in the crystal structures (M2). This was done to determine which influence these additional carbon structures have on the magnetic coupling. With that, it can be evaluated whether the carbon structures have to be considered or can be disregarded. As can be seen from the tables, the additional phenyl rings

¹² In systems where the spin densities are delocalized, the Heisenberg Hamiltonian formalism does not hold anymore, as it requires localized spin centers. However, the total energies of different magnetic orders can be compared, revealing the most favourable ordering.

do barely influence the coupling constant. Only for the models as derived from DUT-8(Ni)_{open,vc}, a rather large difference between the J_{ij} of M1 and M2 is obtained. As already mentioned, this model is characterized by a very small Ni-Ni distance (see Appendix 7). For all further investigations, the phenyl rings have been disregarded, because the coupling constant for all other models is unaffected by these structural elements.

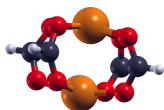


The removal of one NH₃ group was analyzed next (M3). For this model, the magnetic ground state changes from a low-spin to a high-spin state with a resulting spin of $S = 1$. This is caused by the missing attractive interaction between one N to a Ni atom. With that, the electronic density between the Ni atoms increases, leading to a significant overlap of their wave functions.

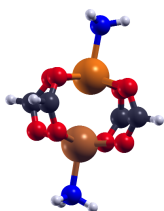
As a consequence, a stronger Ni-Ni interaction and a spin state of 1 occurs.

Those model systems represent the crystal structure with a missing dabco unit, which can appear as a defect in the crystalline nature. Thus, it would be interesting to introduce such defects experimentally and analyze the change in the local magnetic ordering. The effect of defects on the coupling constant were further investigated in section 3.5.2.

For M4 the same result as for M3 is obtained, as the corresponding change is equivalent (removal of one NH₃ group). Only for DUT-8(Ni)_{closed,init} the calculated coupling constant is almost zero. This is a result of the geometry of the system. A significantly different electronic structures upon removal of the different NH₃ groups is present. However, all other models show the same behavior as M3, thus a consistent result is found.



The explanation for M3/M4 holds for M5 as well. Here, the nitrogen atoms are entirely absent, leading to a strong overlap of the wave functions in between the Ni atoms. The remaining electrons arrange in a high-spin ordering. For the optimized structures, the low-spin state becomes non-magnetic and therefore was not further studied.

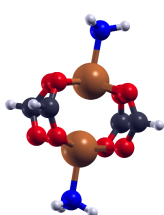


A different magnetic behavior is expected for M6, considering the different electronic configurations of Ni ([Ar]4s²3d⁸) and Cu ([Ar]4s¹3d¹⁰). With that, a different number of unpaired electrons per system occurs, which will interact differently. As is known from literature (e.g. [17]), Cu complexes tend to couple in a low-spin manner ($S = 0$) with a rather small energy difference to the high-spin state of ≈ 100 meV. This can be confirmed with the calculations on such systems. The coupling constants indicate a low-spin magnetic coupling. However, the energy differences to the high-spin state are approximately a factor of two smaller in comparison to the M1 system. An explanation can be based on the larger number of unpaired electrons in a pure Ni-system. For M6, there are two electrons from the Ni atom which participate in the magnetic interaction while there is one from Cu. This results in a high-spin state with $S_{\text{HS}} = 3/2$ and a low-spin state with $S_{\text{LS}} = 1/2$. Thus, there are always two electrons aligned parallel at the Ni site which will align either parallel ($\uparrow\uparrow$) or antiparallel ($\uparrow\downarrow$) with the electron from Cu. Consequently, the separation between the high-spin and the low-spin state is not as distinct as for the pure Cu system ($\uparrow\uparrow$ or $\uparrow\downarrow$, M8), leading to a smaller energy difference.

For DUT-8(Ni)_{closed,init}, once more a coupling constant close to zero is observed. This can again be explained by the geometry and the corresponding different contributions of the electronic structure within this system.

An exception considering the coupling constant is found for DUT-8(Ni)_{closed,vc}, where a high-spin coupling is observed. This might be caused by the different Ni-Cu distance occurring in this model (compared to models derived from the other crystal geometries). As for all other models a low-spin coupling is present, there might be a small distance regime where the magnetic coupling changes to a high-spin manner. Applying stress or strain to the crystal systems could cause different distances between the metal centers. Thus, it would be interesting to investigate whether the magnetic interaction can be changed from a LS to a HS coupling by external forces (e.g. pressure).

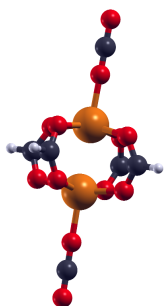
For the M7 system, the same explanation as for M6 can be applied. Here, even the DUT-8(Ni)_{closed,init} model shows a LS coupling.



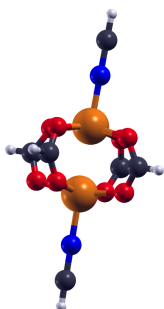
Further, for M8 (pure Cu system) a larger energy difference than in the Ni-Cu mixed systems is found. This can be attributed to the magnetic configurations which occur in each system (see explanation for M6 as well). For FPLO and DUT-8(Ni)_{open,vc}, a non-magnetic state for the low-spin ordering is found. Thus, no further evaluation is carried out.



Considering the model M9, one expects rather strong changes in the magnetic ground state in analogy to the work of [63]. For a substitution of the NH₃ groups with water, two lone pairs of the oxygen are pointing towards the Ni atoms. The oxygen can be characterized to have a sp³ hybridization. Additionally, the Ni-N interaction most likely plays a crucial role in the resulting ground state. However, the Ni atoms are now coordinated with another oxygen instead of the initial nitrogen. As a result, the energy difference $\Delta E_{\text{LS-HS}}$ is comparably small. However, the magnetic ground state already changed to a high-spin state with a spin of 1. This shows the significance of the functional groups at the Ni atoms regarding the magnetic ground state.



For M10, the energy difference is approximately five times larger compared to M9 while the ground state is maintained with a spin of 1. This can be attributed to the significantly stronger interaction of the oxygen to its carbon atom (double bond, sp² hybridization) within the CO₂ molecule. With that, the bonding situation of the adjacent groups plays an important role in the resulting magnetic ground state.



In the last model system (M11) the nitrogen forms a triple bond with its neighboring carbon atom (N≡C-H), leading to a sp-hybridisation. This gives rise to the increase in the energy difference between the high-spin and low-spin state, which seems to be consistent among all considered model systems.

The analysis of the model systems shows that the magnetic ground state within the original Ni dimer system can be easily modified by rather small changes in the chemical environment. It should be possible to implement some of the changes in an experimental setup. The stability of the resulting structures remains to be determined, but the potential to generate a high-spin MOF is certainly given, even with Ni dimers as SBUs.

Given the fact that the replacement with Cu (M6, M7, M8) leads to a rather large change in the coupling constant while keeping the low-spin magnetic behavior, further investigations were carried out. These included a replacement of the metal centers with other 3d-metals, leaving the chemical environment unchanged. With that, the sole influence of the magnetic centers on the magnetic ground state were analyzed. For information regarding the results of this investigation, please see Schwalbe et al. [13].

From this investigation, several combinations of 3d-elements are found to couple in a HS manner. Regarding these findings, further analysis should include a replacement of the obtained combinations of 3d-metals into the crystal structures. An analysis of their stability could be done with e.g. molecular dynamics. Additional investigations regarding long-range magnetic interactions between these HS-SBUs are given in section 3.5.3.

Considering the replacement of the SBU, two approaches could be carried out. On the one hand, all original SBUs could be replaced with HS-SBUs, even though they might not stabilize within the original geometry. On the other hand, one SBU could be replaced with a HS-SBU, while all surrounding ones are left to be the original SBUs. This could stabilize the replaced SBU within the periodic framework and might generate a localized high-spin site surrounded by low-spin units. These low-spin units could then serve as a separator between HS sites, creating a three-dimensional, distinct network of clearly separated high-spin sites.

A thorough theoretical analysis of this stability would require very large supercells. Afterwards, molecular dynamics simulations would have to be carried out for a long time to ensure equilibration. This is beyond the scope of this thesis, but it remains an interesting question for possible future work, both theoretically as well as experimentally.

3.5.2. INFLUENCE OF DEFECTS ON J_{ij}

In this section, results of investigations on systems with a missing dabco unit are reported. Such systems represent defects in the crystal structure. This might be interesting for a comparison with experiment, where defects will be present at all times to a certain extent.

To study the effect of a missing dabco unit, another model was generated, as depicted in figure 3.5. It consists of two M3 models, where the Ni sites with removed NH_3 groups are facing each other. Within this model, different magnetizations on the four Ni centers can be implied (each arrow counts for two electrons at the specific center), i.e. HS(local) and HS(global) $\uparrow\uparrow\uparrow$, HS(local) and LS(global) $\uparrow\uparrow\downarrow$ and LS(local) $\uparrow\downarrow\downarrow$ (see figure 3.6 for a more detailed description).

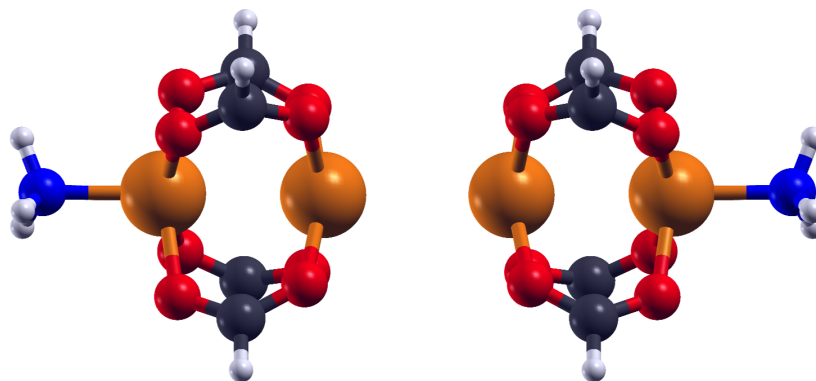


Figure 3.5.: Model system consisting of two M3 models for the evaluation of the magnetic behavior of adjacent SBUs with a removed dabco unit.

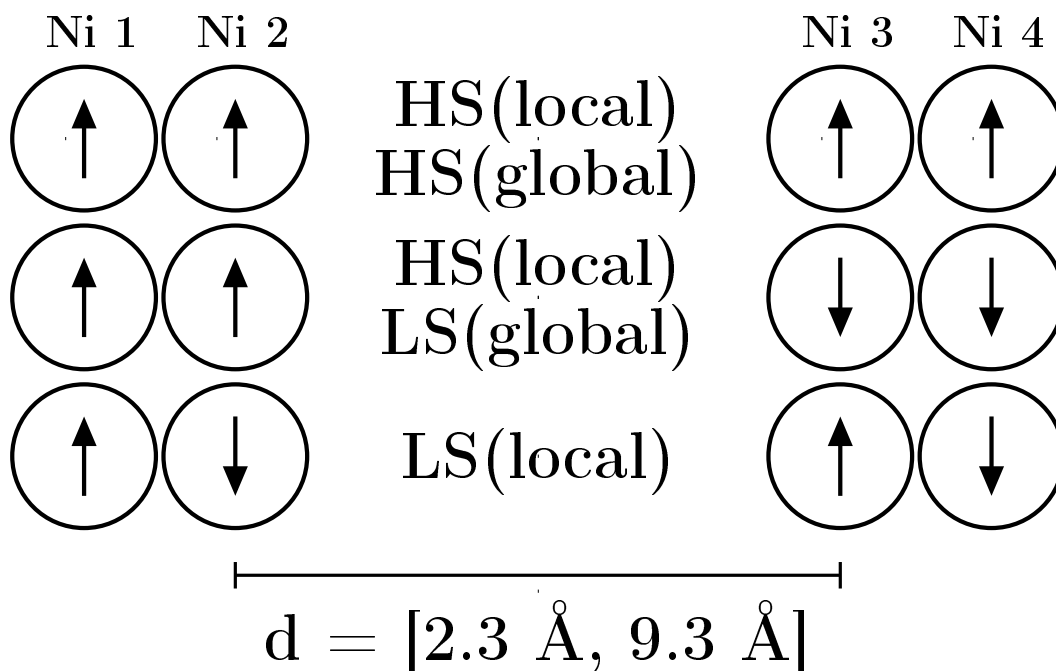


Figure 3.6.: Visualization of the different possible magnetic orientations for a system consisting of two M3 models. Here, Ni atoms 2 and 3 are the sites where the dabco unit has been removed.

For each of those magnetizations, the distance between the two M3 models was successively increased between 2.3 Å and 9.3 Å. This ensures to start from a binding situation and to end at two isolated M3 models. The analysis of the total energies as a function of increasing distance will indicate which of the orderings is most favourable.

As can be seen from figure 3.7, the local HS character is always favourable, as expected from the calculations on the isolated M3 systems. Furthermore, the global magnetic interaction between the SBUs has no effect on the total energy. Thus, the local ordering is significantly stronger than the global interaction¹³. This gives further evidence that the magnetism in the MOFs is completely localized, even in the limiting case of a missing dabco unit.

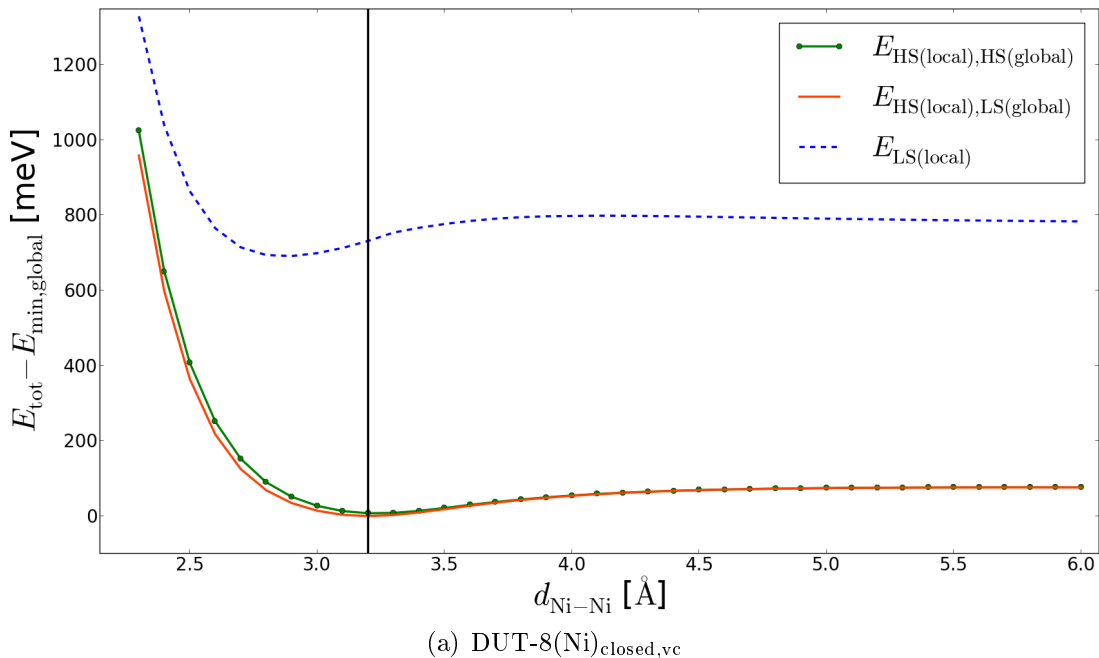


Figure 3.7.: Total energy difference of different magnetic orderings as a function of the Ni-Ni distance. The global energy minimum is always obtained for a local HS coupling, independent of the coupling between the SBUs. The black line denotes the minimum distance.

¹³ Corresponding investigations were performed for DUT-8(Ni)_{open,vc} and DUT-8(Ni)_{open,init}. The results of these investigations are equivalent to the ones reported here (see Appendix 8 for further details).

3.5.3. INFLUENCE OF LONG-RANGE MAGNETIC INTERACTIONS ON J_{ij}

As discussed in the previous sections, the magnetism within the SBU is localized. The investigation of Schwalbe et al. [13] were concerned with the metal exchange in the magnetic dimer unit. An entire family of HS-SBUs was obtained (Fe-Fe, Fe-Co, Fe-Ni and Fe-Cu). Furthermore, as discussed in section 3.5.1, the Ni-Cu dimer coupled in a HS manner for the model system derived from $\text{DUT-8(Ni)}_{\text{closed,vc}}$. With that, further investigations were carried out for these HS-SBUs.

The question about the stability of the local magnetic ordering regarding long-range magnetic interactions along the dabco unit arises (as already mentioned in section 3.4). To analyze this stability, another model system has been generated (see figure 3.8). Within this model, two SBUs are connected with a dabco unit. For the discussions in this section, only the model as derived from $\text{DUT-8(Ni)}_{\text{closed,vc}}$ is used. This was done because the calculations are computationally demanding and the results should be similar for model systems derived from other crystal structures¹⁴. Additionally, the Ni-Cu system as a HS-SBU can be studied.

Considering that there is a maximum amount of two different magnetic centers per SBU (e.g. $X = \text{Fe}$ and $Y = \text{Ni}$) and two SBUs in the model system, three different geometries have to be distinguished, namely XY-D-XY, XY-D-YX and YX-D-XY (the dabco unit will be abbreviated with D). For each of these geometries, two different magnetic orderings can be implied while keeping the HS character per SBU ($\uparrow\uparrow$ -D- $\uparrow\uparrow$ and $\uparrow\uparrow$ -D- $\downarrow\downarrow$). A geometry in addition to a magnetic ordering will be referred to as a configuration (for clarification, see figure 3.9 and table 3.8).

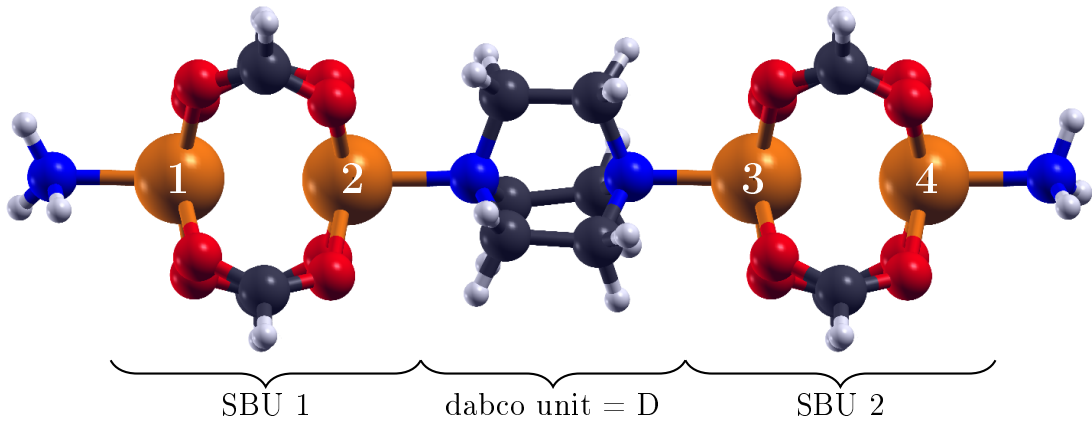


Figure 3.8.: Model system including the dabco unit and two SBUs. The metal centers are enumerated.

$$\left. \begin{array}{l} \text{geometry } \{ X \ Y \quad - \ D \ - \quad X \ Y \} \\ \text{ordering } \{ \uparrow \ \downarrow \quad \quad \quad \uparrow \ \downarrow \} \end{array} \right\} \text{configuration}$$

Figure 3.9.: Explanation of the terms geometry (arrangement of atoms), ordering (spin orientation at the metal centers) and configuration (geometry + ordering). The labels X and Y denote different magnetic centers.

¹⁴ Similar results were obtained for a model system derived from $\text{DUT-8(Ni)}_{\text{open,init}}$, see Appendix 9.

Table 3.8.: Geometries with associated labels of the investigated configurations.

Geometry	Label	Configuration
XX-D-XX	C1	Ni ₁ ↑ Ni ₂ ↓ - D - Ni ₃ ↑ Ni ₄ ↓
	C2	Ni ₁ ↑ Ni ₂ ↓ - D - Ni ₃ ↓ Ni ₄ ↑
	C3	Fe ₁ ↑ Fe ₂ ↑ - D - Fe ₃ ↑ Fe ₄ ↑
	C4	Fe ₁ ↑ Fe ₂ ↑ - D - Fe ₃ ↓ Fe ₄ ↓
XY-D-XY	C5	X ₁ ↑ Y ₂ ↑ - D - X ₃ ↑ Y ₄ ↑
	C6	X ₁ ↑ Y ₂ ↑ - D - X ₃ ↓ Y ₄ ↓
XY-D-YX	C7	X ₁ ↑ Y ₂ ↑ - D - Y ₃ ↑ X ₄ ↑
	C8	X ₁ ↑ Y ₂ ↑ - D - Y ₃ ↓ X ₄ ↓
YX-D-XY	C9	Y ₁ ↑ X ₂ ↑ - D - X ₃ ↑ Y ₄ ↑
	C10	Y ₁ ↑ X ₂ ↑ - D - X ₃ ↓ Y ₄ ↓

As a starting point, the original Ni dimer SBUs with two different magnetic orderings were calculated (configurations C1 and C2), see table 3.8. The magnetic interaction between the two SBUs for this local LS coupling is negligible (see table 3.9).

To analyze the long-range magnetic behavior further, different configurations for all HS-SBUs (i.e. C4–C3, C6–C5, C8–C7, C10–C9) were compared, see tables 3.8 and 3.9. For configurations C5 to C10, an odd number (C5, C7 and C9) refers to a global high-spin coupling while an even number (C6, C8 and C10) denotes a global low-spin coupling. Additionally, the coupling constant between the SBUs can be calculated. For that purpose, each SBU can be assumed to serve as one magnetic center. Consequently, J_{ij} can be evaluated like $J_{C5,C6} = (E_{C6} - E_{C5}) / (\langle \mathbf{S}_{\text{tot},C5}^2 \rangle)^{15}$. The energy differences and the resulting coupling constants are very small (see table 3.9). Regarding these values, no significant global magnetic interaction along the dabco unit occurs.

To further verify the results, optimizations for configurations C1, C2, C3 and C4 were carried out. There are no major differences in neither energy nor the resulting geometry ($\Delta E_{C1-C2,\text{opt}} = -5.07$ meV, $\Delta E_{C4-C3,\text{opt}} = -2.91$ meV). Thus, the local character of the magnetism is stable for a local LS and a local HS coupling.

Table 3.9.: Energy differences and coupling constants for specific configurations.

System	ΔE_{QE} [meV]	ΔE_{FPLO} [meV]	J_{QE} [cm ⁻¹]	J_{FPLO} [cm ⁻¹]
NiNi $E_{C1} - E_{C2}$	-6.81	-7.02	—	—
FeFe $E_{C4} - E_{C3}$	-2.87	—	-0.32	—
FeCo $E_{C6} - E_{C5}$	-3.16	—	-0.46	—
FeCo $E_{C8} - E_{C7}$	-4.45	-4.27	-0.64	-0.62
FeCo $E_{C10} - E_{C9}$	-2.43	-1.85	-0.35	-0.27
FeNi $E_{C6} - E_{C5}$	-3.33	-2.50	-0.64	-0.48
FeNi $E_{C8} - E_{C7}$	-4.13	-3.18	-0.79	-0.61
FeNi $E_{C10} - E_{C9}$	-2.52	-1.79	-0.48	-0.34
FeCu $E_{C6} - E_{C5}$	+0.87	-1.96	+0.23	-0.53
FeCu $E_{C8} - E_{C7}$	-2.11	-1.61	-0.57	-0.52
FeCu $E_{C10} - E_{C9}$	—	—	—	—
NiCu $E_{C6} - E_{C5}$	-3.19	-4.19	-2.15	-2.82
NiCu $E_{C8} - E_{C7}$	-1.06	-1.36	-0.73	-0.91
NiCu $E_{C10} - E_{C9}$	-7.93	-8.54	-5.33	-5.74

¹⁵ This is in analogy to equation (2.58), regarding two equal centers for the calculation of J_{ij} .

Considering the results in table 3.9, the total energy per geometry is unaffected regarding different magnetic orderings. In the following, results of investigations regarding the most favourable geometry will be reported. Only one energy for any geometry needs to be considered. This energy is given as e.g. $E_{XY-D-XY} = (E_{C5} + E_{C6})/2$.

For any combination of elements, certain geometries are energetically more favourable than others. Given the case that e.g. XY-D-YX is the most favourable geometry, the periodicity of the crystal structure needs to be considered. Starting with this geometry, the next SBU is going to have a XY characteristics (XY-D-YX-D- \overline{XY}). Thus, the next SBU-D-SBU geometry is YX-D-XY, which might be the least favourable geometry. Considering a periodic structure, an alternating sequence of YX-D-XY and XY-D-YX occurs (see figure 3.10 for clarification).

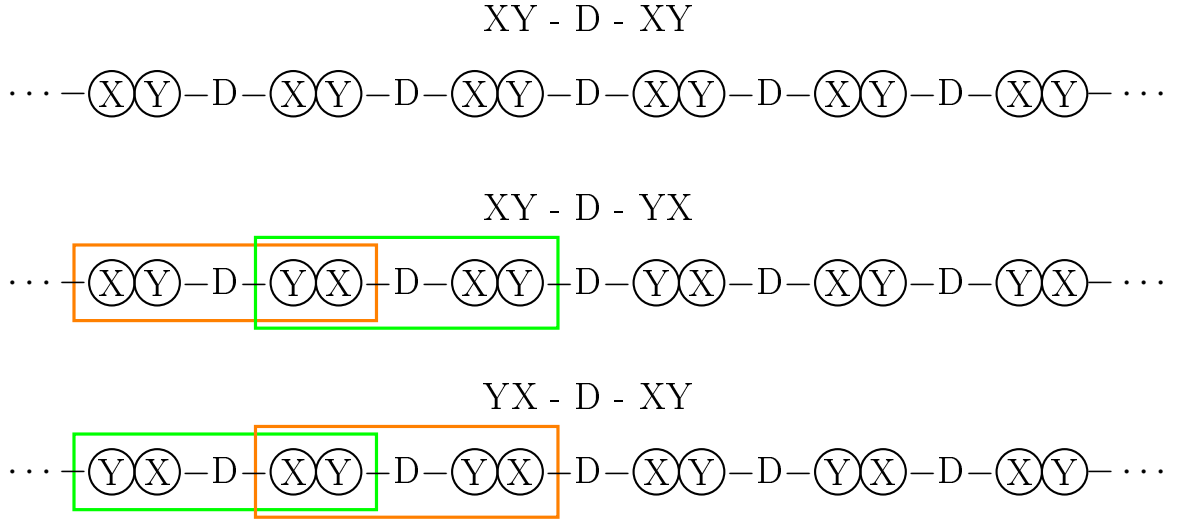


Figure 3.10.: Visualization of the different possible geometries along the dabco unit considering two SBUs. The green rectangle emphasizes the XY-D-YX geometry while the orange one highlights the YX-D-XY geometry. The periodic repetition is shown, indicating that the last two configurations are identical.

Consequently for these two geometries, the average of their energies has to be considered. This average might be energetically less favourable than the XY-D-XY geometry. With that, the energies $E_{XY-D-XY}$, $E_{XY-D-YX}$ and $E_{YX-D-XY}$ have to be calculated and compared. Accordingly, the energy difference ΔE_{geo} needs to be evaluated like

$$\Delta E_{\text{geo}} = E_{XY-D-XY} - \frac{E_{XY-D-YX} + E_{YX-D-XY}}{2}. \quad (3.3)$$

A negative value of ΔE_{geo} indicates XY-D-XY to be the most favourable geometry. On the other hand, a positive value occurs if the average of XY-D-YX and YX-D-XY is more stable. The results are summarized in tables 3.10 and 3.11. All energy values are given in Appendix 10.

From tables 3.10 and 3.11 it can be seen that the FeNi system has a lower energy for the XY-D-XY geometry. Thus, this alternating sequence of FeNi between SBUs is favourable. Whether such an ordering can be stabilized in a crystalline structure and if a realization of the HS-SBUs in spintronic devices is possible should be investigated in future works.

Table 3.10.: Calculated energy differences (with QE) for specific geometries within the model displayed in figure 3.8.

System	$E_{XY-D-XY}$ [Ry]	$E_{XY-D-YX}$ [Ry]	$E_{YX-D-XY}$ [Ry]	ΔE_{geo} [meV]
FeCo	-2051.109365	-2051.111032	-2051.108662	+6.56
FeNi	-2098.457712	-2098.457113	-2098.454815	-23.78
FeCu	-2153.143962	-2153.140394	-2153.145650	-12.78
NiCu	-1865.954956	-1865.947261	-1865.962280	-2.52

Table 3.11.: Calculated energy differences (with FPLO) for specific geometries within the model displayed in figure 3.8.

System	$E_{XY-D-XY}$ [Ha]	$E_{XY-D-YX}$ [Ha]	$E_{YX-D-XY}$ [Ha]	ΔE_{geo} [meV]
FeCo	-7304.255696	-7304.256367	-7304.255675	+8.83
FeNi	-7558.997465	-7558.996760	-7558.996481	-22.98
FeCu	-7827.353495	-7827.351332	-7827.354320	-9.09
NiCu	-8323.390924	-8323.387363	-8323.394306	-2.44

In summary, the performed calculations show that the local character of the magnetism is unchanged considering long-range interaction along the dabco units. This stability should be further examined to study the potential applicability of the given HS-SBUs. Regarding spintronic applications, a stabilization of such HS-SBUs within a crystal structure could be used for the design of either memories on very small scales or logic devices.

PART IV.

MAGNETIC SHIELDING OF ^{129}Xe IN UIO-66/UIO-67

4.1. STRUCTURAL CONSIDERATIONS

In analogy to the investigations of the MOF DUT-8(Ni), the atomic positions as well as the unit cells for the Zr-MOFs UiO-66 and UiO-67 have been fully optimized. This ensures a consistent analysis of the structures in the employed theoretical framework. The resulting cell vectors are given as follows ('prim' stand for the primitive and 'conv' for the conventional unit cell):

Opt UiO-66:

$$\mathbf{a}_{\text{prim}} = \begin{pmatrix} -10.45935 \\ 0.00000 \\ 10.45935 \end{pmatrix} \text{ \AA}, \mathbf{b}_{\text{prim}} = \begin{pmatrix} 0.00000 \\ 10.45935 \\ 10.45935 \end{pmatrix} \text{ \AA}, \mathbf{c}_{\text{prim}} = \begin{pmatrix} -10.45935 \\ 10.45935 \\ 0.00000 \end{pmatrix} \text{ \AA}$$

$$\mathbf{a}_{\text{conv}} = \begin{pmatrix} 20.91871 \\ 0.00000 \\ 0.00000 \end{pmatrix} \text{ \AA}, \mathbf{b}_{\text{conv}} = \begin{pmatrix} 0.00000 \\ 20.91871 \\ 0.00000 \end{pmatrix} \text{ \AA}, \mathbf{c}_{\text{conv}} = \begin{pmatrix} 0.00000 \\ 0.00000 \\ 20.91871 \end{pmatrix} \text{ \AA}$$

Opt UiO-67:

$$\mathbf{a}_{\text{prim}} = \begin{pmatrix} -13.50731 \\ 0.00000 \\ 13.50731 \end{pmatrix} \text{ \AA}, \mathbf{b}_{\text{prim}} = \begin{pmatrix} 0.00000 \\ 13.50731 \\ 13.50731 \end{pmatrix} \text{ \AA}, \mathbf{c}_{\text{prim}} = \begin{pmatrix} -13.50731 \\ 13.50731 \\ 0.00000 \end{pmatrix} \text{ \AA}$$

$$\mathbf{a}_{\text{conv}} = \begin{pmatrix} 27.01461 \\ 0.00000 \\ 0.00000 \end{pmatrix} \text{ \AA}, \mathbf{b}_{\text{conv}} = \begin{pmatrix} 0.00000 \\ 27.01461 \\ 0.00000 \end{pmatrix} \text{ \AA}, \mathbf{c}_{\text{conv}} = \begin{pmatrix} 0.00000 \\ 0.00000 \\ 27.01461 \end{pmatrix} \text{ \AA}$$

Table 4.1.: Cell parameters for the conventional unit cell obtained from geometry optimization of the two MOFs UiO-66 and UiO-67.

		a [\AA]	b [\AA]	c [\AA]	α [°]	β [°]	γ [°]
UiO-66	Opt	20.9187	20.9187	20.9187	90	90	90
	Literature [28]	20.9784	20.9784	20.9784	90	90	90
UiO-67	Opt	27.0146	27.0146	27.0146	90	90	90
	Literature [30]	27.0942	27.0942	27.0942	90	90	90

The optimized structures agree well with the structures from the literature [28, 30]. The deviation is approximately 0.3 %. Further details are given in Appendix 1. For all further investigations, the fully optimized structures are used. Furthermore, the primitive unit cells for both MOFs are considered. From a computational perspective this is necessary, because the conventional unit cells contain a large number of atoms (456 atoms for UiO-66 and 696 atoms for UiO-67). Thus, a feasible treatment within DFT can only be carried out for the primitive unit cells (114 atoms for UiO-66 and 174 atoms for UiO-67). Additionally, taking into account the adsorption of Xe atoms into the structures, the computational time for molecular dynamics (MD) can be significantly reduced by employing the primitive cells, as only a fraction of Xe atoms needs to be added to fill the pores of the MOFs.

4.2. ^1H AND ^{13}C NMR INVESTIGATIONS

To validate the GIPAW method implemented in Quantum ESPRESSO (QE), the ^{13}C and ^1H chemical shifts for both MOFs (UiO-66 and UiO-67) were calculated and compared with experimental values [64, 65]¹⁶. The reference shielding values for the QE results are taken from calculations of tetramethylsilane (TMS), with $\sigma_{\text{ref,C}} = 176.64$ ppm and $\sigma_{\text{ref,H}} = 30.67$ ppm. In tables 4.2 and 4.3, the results are summarized. As seen in these tables, the calculated results agree well with the literature values. All values are slightly larger than the experimental chemical shifts, but the relative differences for different atoms can be reproduced. As this behavior occurs consistently for all analyzed species, it could be expected that in general the calculated chemical shifts will be larger than the experimental values.

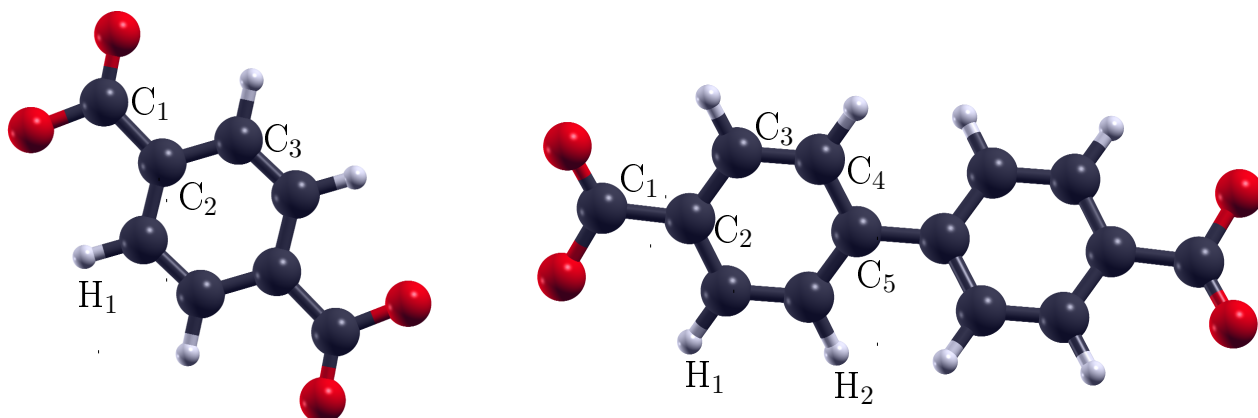


Figure 4.1.: Assignment of the carbon and hydrogen atoms in the linkers of UiO-66 and UiO-67 as used in table 4.2 and 4.3.

Table 4.2.: Comparison between literature values and QE results for the ^{13}C chemical shift of UiO-66 and UiO-67. All values are given in ppm.

C atom	UiO-66		UiO-67	
	reference [64]	QE	reference [65]	QE
C ₁	171	185	174	184
C ₂	137	149	134	145
C ₃	131	143	130	143
C ₄	—	—	124	137
C ₅	—	—	143	158

Table 4.3.: Comparison between literature values and QE results for the ^1H chemical shift of UiO-66 and UiO-67. The hydrogen atoms of the SBU are labelled H_{SBU} . All values are given in ppm.

C atom	UiO-66		UiO-67	
	reference [64]	QE	reference [65]	QE
H_{SBU}	2.6	4.0	2.5	3.4
H ₁	8.0	11.5	7.8	9.7
H ₂	—	—	8.3	10.5

¹⁶ The experimental values for UiO-67 are taken from Figures 2-4 in the supplementary material of [65].

4.3. MODEL SYSTEMS

High-pressure NMR measurements of the ^{129}Xe chemical shift in the MOFs UiO-66 and UiO-67 show a decrease of the chemical shift comparing the smaller (UiO-66) with the larger (UiO-67) structure. To assist with an explanation of this behavior from the theoretical side, the chemical shift of Xe within the MOFs has to be analyzed. For a systematic investigation of the chemical shift, a Xe atom could be placed at several positions inside the crystal structure to calculate the corresponding magnetic shielding. Additionally, the influence on the chemical shift by adjacent Xe atoms might be analyzed by placing several Xe atoms at different positions.

However, such calculations would be computationally very demanding. Considering this approach, a large number of different Xe positions within the porous networks would have to be analyzed. This procedure is not efficient and would require an enormous amount of computational time. Thus, the investigation has not been carried out as described above.

Another approach is based on the individual characterization of several influences on the chemical shift. This approach is in close analogy to the work of Ito and Fraissard [59] (see section 2.6.2), who proposed that the ^{129}Xe chemical shift can be described by the sum of several contributions (see equation (2.73)).

These contributions include the influence of Xe-Xe interactions ($\delta_{\text{Xe-Xe}}$) as well as Xe-surface interactions (δ_{S}) on the chemical shift. Furthermore, a reference (δ_0) is needed to calculate the chemical shift for a given value of the magnetic shielding. Based on this approach, model systems have been constructed to evaluate the different contributions individually. This does not only allow an individual analysis of different influences on the chemical shift, but reduces the computational effort drastically. Furthermore, this individual analysis provides information about the chemical shift in each of the different pores of the MOFs. With that, the evaluation of the chemical shift at an atomistic level can be carried out. In the following sections, the model systems for the different contributions are introduced. At the end, the chemical shift within the MOFs UiO-66 and UiO-67 in the high-pressure limit will be evaluated. This enables an explanation of the observed behavior of the chemical shift when comparing the two MOFs, i.e. the decrease of the chemical shift from UiO-66 to UiO-67.

In all further discussions, the total chemical shift is calculated as $\delta_{\text{tot}} = \sigma_{\text{ref}} - 1/3(\sigma_{11} + \sigma_{22} + \sigma_{33})$ ¹⁷. Accordingly, the scalar and isotropic chemical shift is evaluated to be comparable with experiments. The σ_{ij} are the entries of the shielding tensor corresponding to the investigated Xe atom. These entries will be different in comparison to an isolated Xe atom, leading to $\delta_{\text{tot}} \neq 0$. For an anisotropic shift in a certain direction, the relation $\delta_i = \sigma_{\text{ref}} - \sigma_{ii}$ can be used instead (where $i = 1, 2, 3$ corresponds to the cartesian coordinates x, y, z).

4.3.1. ^{129}Xe REFERENCE δ_0

Following the approach of Ito and Fraissard (see equation (2.73)) [59], the reference shielding δ_0 for Xe is needed. This reference value is the magnetic shielding of an isolated Xe atom. For calculations with QE, a reference value of $\sigma_{\text{ref}} = 6192.47$ ppm is obtained, which will be used for the evaluation of the chemical shift.

¹⁷ All entries in σ_{ref} are identical ($\sigma_{\text{ref},11} = \sigma_{\text{ref},22} = \sigma_{\text{ref},33} = \sigma_{\text{ref}}$), because the reference system is isotropic (Xe atom).

To verify this value, additional steps were carried out. In literature, a shielding value from a fully relativistic calculation using the ADF code is obtained with a value of $\sigma_{\text{ref,lit}} = 6409$ ppm [66]. Our own ADF calculation gives a value of $\sigma_{\text{ref,ADF}} = 6597$ ppm (PBE exchange-correlation functional, QZ4P basis set, using the zeroth order regular approximation (ZORA) to the Dirac equation [67, 68, 69, 70] to treat relativistic effects). Thus, the QE values deviates from a fully relativistic treatment by 3 - 6 %, which is a known trend when comparing scalar relativistic with fully relativistic calculations of the magnetic shielding [71]¹⁸.

From the experimental side, the reference is obtained by measuring the resonance frequency of Xe gas at different pressures and extrapolate those values to zero pressure. This can be referred to a single Xe atom in vacuum. To verify this approach theoretically, a Xe reference system has been created. For this purpose, a cell of $(20 \times 20 \times 20) \text{ \AA}^3$ is filled with N_{Xe} Xe atoms placed randomly inside this box ($N_{\text{Xe}} \in \mathbb{N}$, $1 \leq N_{\text{Xe}} \leq 30$). This approach simulates different Xe pressure (higher number of Xe atoms \rightarrow higher pressure at constant volume). The minimum distance between the Xe atoms has been chosen to be 4 \AA due to the Xe vdW radius of 2.16 \AA [73]. This avoids that the atoms come too close to each other, considering that Xe is a noble gas and thus mononuclear.

After placing the Xe atoms in the cell, the magnetic shielding of all Xe atoms was calculated. By averaging all magnetic shieldings in each system separately, an average value of the chemical shift $\bar{\delta}$ per discrete number of Xe atoms N_{Xe} is obtained. These values correspond to the experimental approach. To achieve reliable statistics, the presented approach was carried out four times for each number of atoms N_{Xe} . The results are summarized in figure 4.2. A linear behavior in correspondence to experiments has been found.

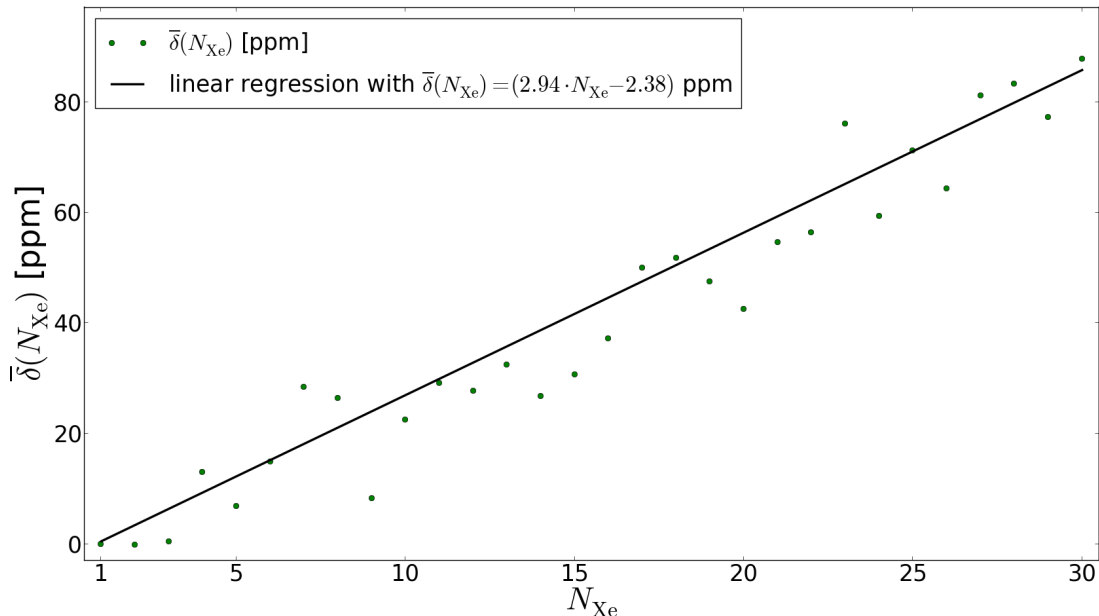


Figure 4.2.: Average chemical shift $\bar{\delta}$ for systems with a different amount of Xe atoms $N_{\text{Xe}} = [1, 30]$.

¹⁸ Another approach to calculate the shielding can be based on the work of Lamb (see equation (2.24)). The corresponding $1/r$ values were taken from fully relativistic Hartree-Fock-Slater calculations [72] (the values are given in Appendix 11). The resulting shielding is $\sigma_{\text{dia}} = 6012.5$ ppm.

4.3.2. INFLUENCE OF Xe-Xe INTERACTIONS $\delta_{\text{Xe-Xe}}$

To describe the influence of Xe-Xe interactions on the chemical shift, another model system has been prepared. Within this system, two Xe atoms are placed at distances of $d_{\text{Xe-Xe}} = [4.00, 7.00]$ Å while the distance was increased by $\Delta d = 0.01$ Å. For each distance, the shielding of the Xe atoms was calculated. The resulting chemical shift as a function of distance is displayed in figure 4.3. An exponential behavior is found. This behavior is used for further evaluations.

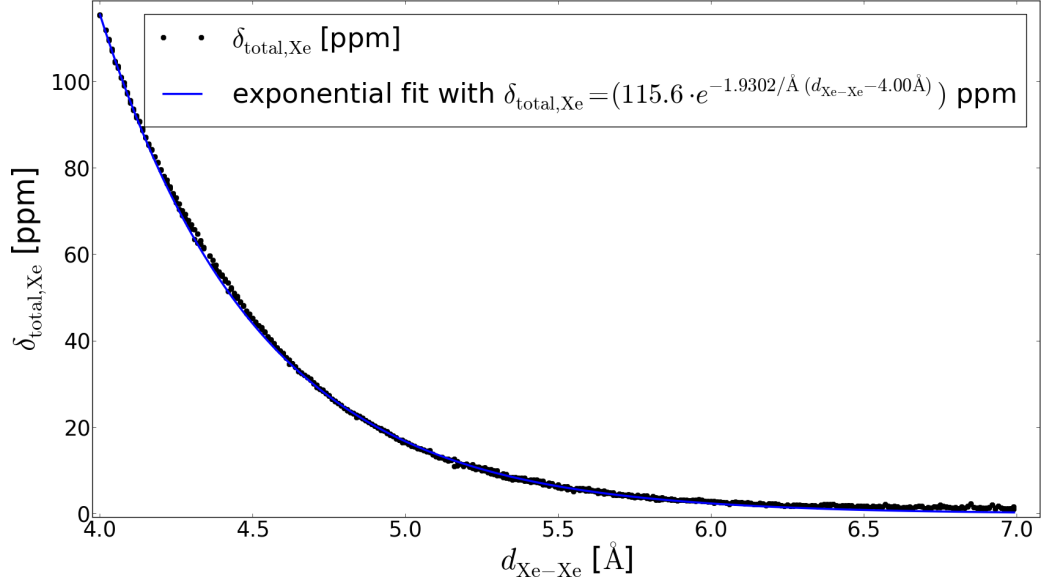


Figure 4.3.: Total chemical shift $\delta_{\text{total,Xe}} = \sigma_{\text{ref}} - 1/3\text{Tr}(\sigma(d_{\text{Xe-Xe}}))$ as a function of distance between two Xe atoms $d_{\text{Xe-Xe}}$.

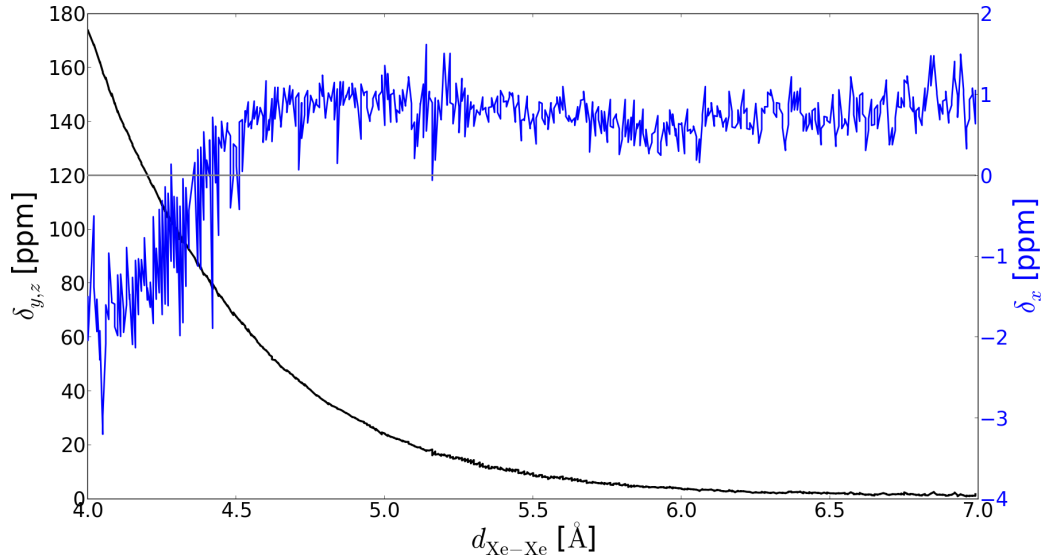


Figure 4.4.: Chemical shift component along the Xe-Xe axis δ_x and perpendicular to this axis $\delta_{y,z}$ as a function of distance of two Xe atoms $d_{\text{Xe-Xe}}$. The gray line separates shielding ($\delta > 0$) and deshielding ($\delta < 0$) regions for δ_x .

The components to the chemical shift in each direction (x, y, z) are plotted in 4.4. Along the Xe-Xe axis (x in this case), the component of the chemical shift is small and slightly increases from a negative value at small distances to a positive value at larger distances. On the contrary, the components in the other two directions are significantly larger and contribute stronger to the total chemical shift. Such a behavior for a Xe pair model is known from literature as well [71].

Because so far only two Xe atoms were taken into account, the validity of the Xe pair model needs to be verified for larger numbers of Xe atoms. For this purpose, the systems with N_{Xe} Xe atoms ($N_{\text{Xe}} = 1, \dots, 30$) were further investigated. The chemical shift of each Xe atom was calculated using the shielding values obtained with QE. Additionally, values using the Xe pair model have been evaluated. This was done to determine whether the influences on $\delta_{\text{Xe-Xe}}$ are additive, thus if $\delta_{\text{Xe-Xe}} = \sum \delta(d_{\text{Xe-Xe}})$. The results are displayed in figure 4.5.

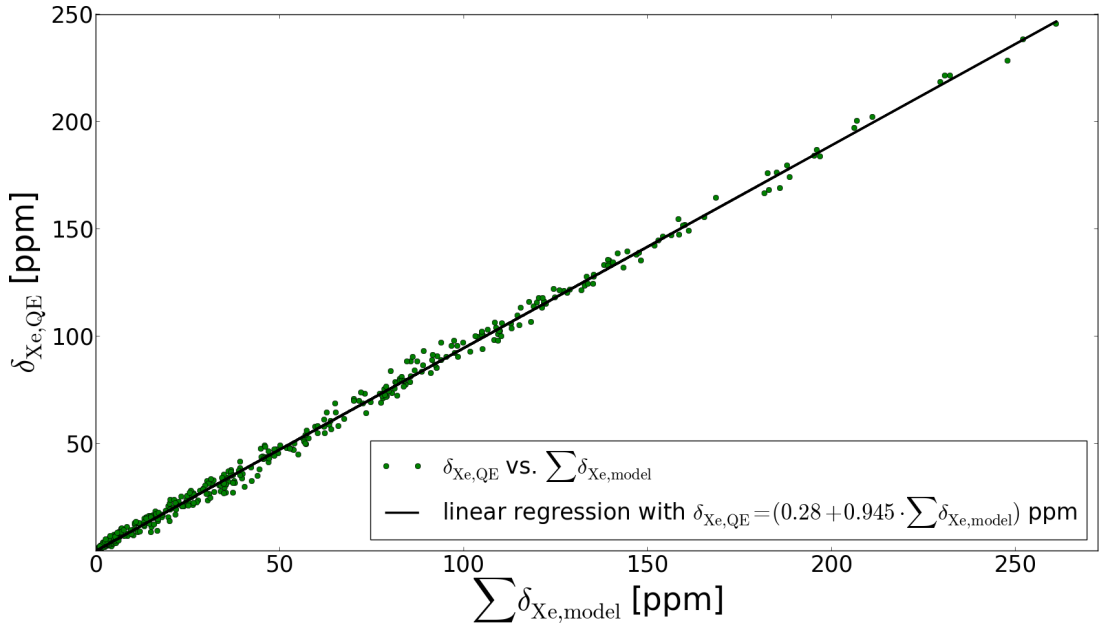


Figure 4.5.: Chemical shifts for all systems with N_{Xe} Xe atoms obtained from the Xe pair model $\sum \delta_{\text{Xe,model}}$ in comparison to the ones obtained from QE calculations (denoted as $\delta_{\text{Xe,QE}}$).

The diagram shows a nearly perfect correlation, as the linear regression has a slope of 0.95 and only slightly deviates from the origin (+0.28 ppm). Additionally, the standard deviation amounts to ± 4.17 ppm. The deviation might stem from higher order effects, which are not covered in the pair model. However, the deviation is small, indicating that such kind of effects play a minor role in the description of $\delta_{\text{Xe-Xe}}$. With that, this model system can be used to describe the chemical shift as introduced by Xe-Xe interactions for any number of Xe atoms.

In experiments, a value for the chemical shift of Xe in the liquid phase of $\delta_{\text{exp}} = 203$ ppm at $T = 237$ K and $p = 1.73$ MPa was observed. To further verify the Xe pair model, this chemical shift was analyzed theoretically. For this purpose, a Monte-Carlo (MC) simulation employing a Metropolis algorithm [74, 75, 76] with a NPT ensemble for 100 Xe atoms, which interact via a Lennard-Jones potential, was used. The temperature and pressure of the simulation were chosen according to the experimental situation.

Initially, the literature values for the Lennard-Jones parameters ($\epsilon = 0.01904$ eV, $\sigma = 3.962$ Å $\rightarrow r_0 = \sqrt[6]{2} \cdot \sigma = 4.447$ Å [77]) were taken. The resulting chemical shift becomes $\delta_{\text{lit}} \approx 125$ ppm, which is much smaller than the experimentally determined chemical shift. However, the literature values were derived for solids at 145 K. Thus, they are not suitable for simulating the desired temperature and pressure conditions. Consequently, a new set of Lennard-Jones parameters had to be established.

Therefore, a geometry optimization of two Xe atoms including vdW corrections [2] was performed (where forces were reduced below 10^{-10} Ry/a₀ = $2.57 \cdot 10^{-9}$ eV/Å). This allows the extraction of the equilibrium distance as well as the potential minimum. The Lennard-Jones potential curves are displayed in figure 4.6.

The minimum distance was found to be $r_0 = 4.189$ Å, showing a rather large deviation to the literature values. This is not surprising, because the vdW radius of Xe used within the correction of Grimme is smaller ($r_{\text{vdW,Xe,Grimme}} = 1.88$ Å) [2] than its actual value ($r_{\text{vdW,Xe}} = 2.16$ Å) [73]. With that, the minimum distance becomes smaller in comparison to the literature values.

The potential minimum was evaluated by comparing the total energy of two isolated Xe atoms ($2 \cdot E_{\text{tot,Xe}}$) with the energy obtained with the optimization ($E_{\text{tot,opt}}$). An energy minimum of $2 \cdot E_{\text{tot,Xe}} - E_{\text{tot,opt}} = \epsilon = 0.01972$ eV has been found, which is close to the literature values. Thus, the main difference in the resulting chemical shift will come from a smaller distance between the Xe atoms, leading to stronger interactions between them.

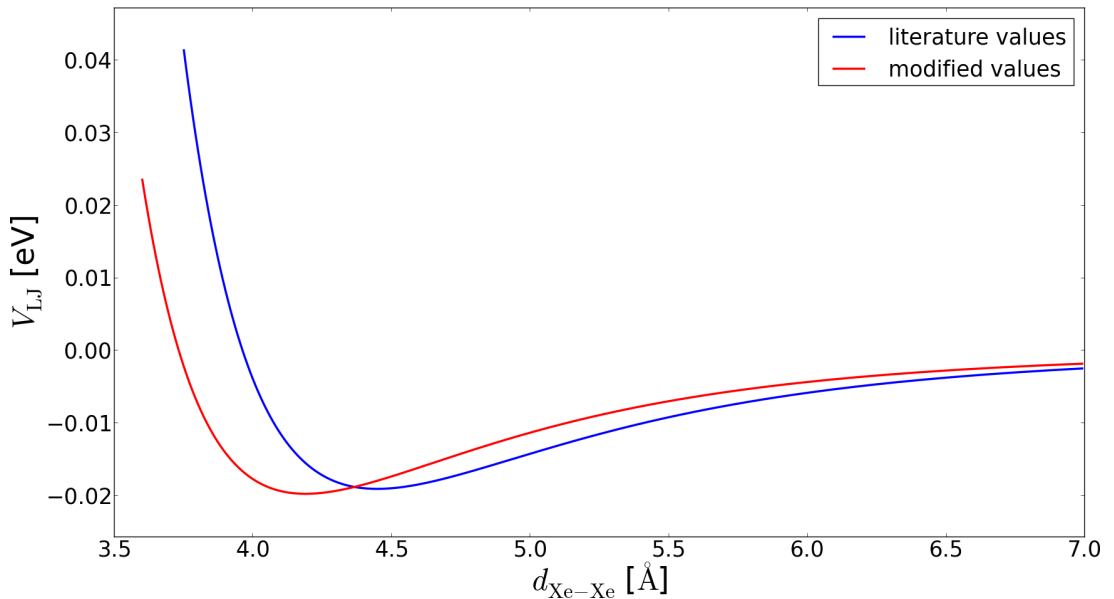


Figure 4.6.: Lennard-Jones potentials for Xe. The potential curves derived from the literature values ($\epsilon = 0.01904$ eV, $\sigma = 3.962$ Å $\rightarrow r_0 = 4.447$ Å [77]) and from the modified values ($\epsilon = 0.01972$ eV, $\sigma = 3.732$ Å $\rightarrow r_0 = 4.189$ Å) are shown.

Given the new parametrization of the Lennard-Jones potential, further Monte-Carlo simulations were performed. Each MC simulation was carried out for $5 \cdot 10^5$ steps, of which $3 \cdot 10^5$ steps were taken for equilibration and $2 \cdot 10^5$ steps were used for the evaluation of the average chemical shift $\bar{\delta}$. To obtain reasonable statistics, the MC has been performed twenty times (see table 4.4). Finally, with the new set of parameters a chemical shift of $\delta_{\text{modified}} \approx 197 \pm 9$ ppm is found, which is in much better agreement with the experimental value ($\delta_{\text{exp}} = 203$ ppm).

Table 4.4.: Chemical shift for liquid Xe as a result of several MC runs at $T = 237$ K and $p = 1.73$ MPa. The average over all runs is named δ_{modified} and given together with its standard deviation.

run	$\bar{\delta}$ [ppm]	run	$\bar{\delta}$ [ppm]
1	195.31	11	191.39
2	221.71	12	205.84
3	195.08	13	187.61
4	197.82	14	193.85
5	203.53	15	208.95
6	182.93	16	190.28
7	200.19	17	189.32
8	189.42	18	192.52
9	185.01	19	191.81
10	200.33	20	209.15
$\delta_{\text{modified}} = 196.60 \pm 9.29$ ppm			

4.3.3. INFLUENCE OF XE-SURFACE INTERACTIONS δ_S

The last contribution to the chemical shift of Xe is the influence of the surface of the system. In this context, surface refers to the walls inside a pore. This contribution becomes especially important in MOFs due to their high porosity and resulting high surface area¹⁹. To investigate δ_S , two further model systems were used²⁰.

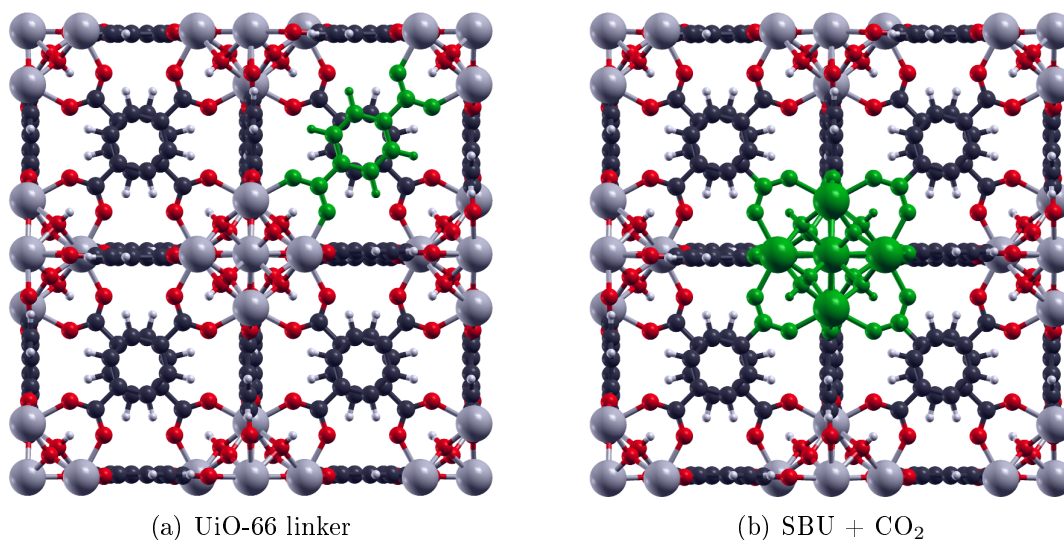


Figure 4.7.: Model systems for the evaluation of δ_S . The linker in UiO-66 as well as the SBU with coordinated CO₂ groups are highlighted.

¹⁹ A thorough analysis of the porosity and the void/accessible volumes of all MOFs has been performed, see Appendix 14. Good agreement with literature values has been obtained.

²⁰ An initial investigation of benzene was carried out, as the chemical shift around this molecule is known [78]. This was done to verify the employed procedure, see Appendix 12.

On the one hand there is the linker in UiO-66 (see figure 4.9), which can be employed to describe all linker related influences on the shift. This is due to the fact that the difference in the linkers of the two MOFs is an additional connection between two carbon rings in UiO-67 (see figure 4.1 in section 4.2). However, all investigations show that this additional connection is negligible for the description of the chemical shift. Adsorbed Xe atoms tend to go into the corners of a pore due to attractive Xe-surface interactions (see Appendix 13). Thus, this additional C-C bond in UiO-67 is not contributing to the chemical shift and can therefore be neglected.

Furthermore, the linker model provides information about the shift in the tetrahedral (T_p) as well as the octahedral (O_p) pores. This can be seen from the orientation of such linkers in the different pores (see figure 4.8 (a)).

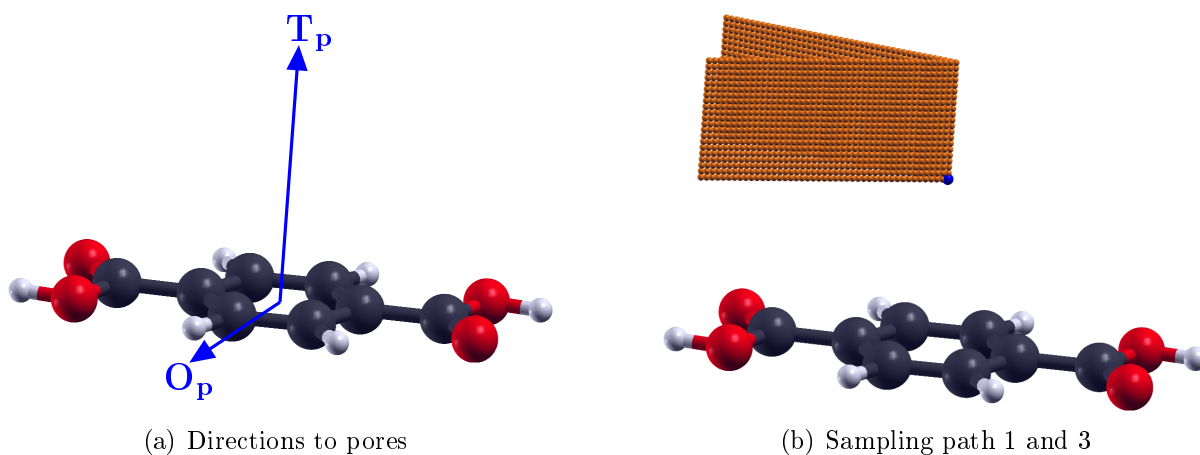


Figure 4.8.: In (a), directions to the pores (out-of-plane: T_p pore, in-plane: O_p pore) are shown. In (b), a visualization of the sampling points for path 1 and 3 is given. The blue dot indicates the point directly above center of the carbon ring.

In the T_p pores, the molecular plane of the linker faces towards the inside of the pore, 'covering' it from all sides. In the O_p pores, the linker lies in-plane, thus sticking into the pores with its outermost hydrogen atoms. In comparison to the T_p pores, the linker can be imagined as being rotated by 90° within the O_p pores.

To analyze the chemical shift, the space around the linker needs to be analyzed in-plane and out-of-plane to cover all effects in each of the pores. To systematically evaluate the chemical shift around this model system, a single Xe atom has been placed at different positions along the linker while the shielding has been computed (see figure 4.8 and 4.9 [21] for clarification).

The out-of-plane contributions have been analyzed by placing a Xe atom above the molecular plane. As a starting point, the position directly above the middle of the carbon ring was chosen. Afterwards, the Xe atom has been moved towards the oxygen atoms in 0.1 \AA steps (path 1 and path 3 in figure 4.8 and 4.9).

Additionally, starting from the same initial position the Xe atom has been moved by 0.1 Å steps towards a position in between the O atoms (path 2). For each movement, the height to the molecular plane has been increased systematically by 0.1 Å.

The influence of the carbon ring on the chemical shift was analyzed similarly by moving a Xe atom either towards a C-H bond or in between two carbon atoms (path 7 and path 8). This was done for a benzene molecule, because the influence on the chemical shift is expected to be the same for both molecules. However, the computational time for benzene is lower. Given this analysis, all possible relative positions to the model system for the T_p pores are covered.

For the relative positions in the O_p pore, the initial starting point was chosen to be along a C-H bond lying in-plane of the molecule. Afterwards, the Xe atom has been moved within the molecular plane by 0.1 Å steps further along the C-H vector as well as perpendicular to this vector (path 4, path 5, path 6). As before, the height to the molecular plane has been increased by 0.1 Å steps to include all relative positions for the O_p pore.

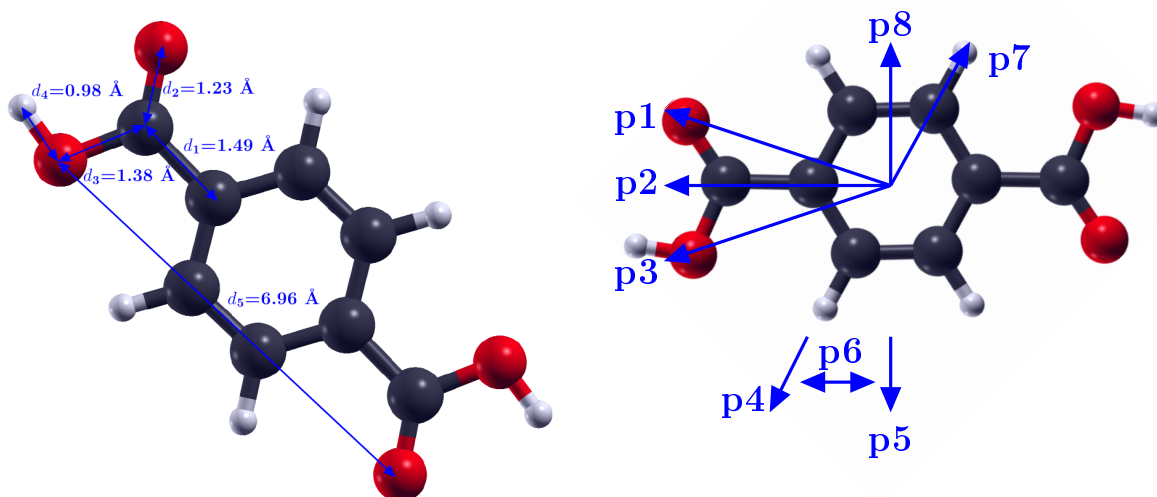


Figure 4.9.: The linker in UiO-66 as a model system to derive δ_S according to the influence of this molecule on the chemical shift of Xe.

On the left side, the distances within this model are shown. On the right side, the directions of the sampling paths (abbreviated with p) are illustrated. Path 1 (p1) and path 3 (p3) have been distinguished to average contributions which occur if Xe is close to the oxygen atoms within the MOFs. In between p4 and p5, several more values have been sampled, denoted as p6. The positions above the H atoms were analyzed with a benzene model, as the influences do not change (denoted as p7 and p8). Additionally for all paths, the height per path has been increased by several steps to include several distances to this structure unit.

The presented approach allows a tabulation of shielding values at any position around the linker model (see figure 4.9 for further details). To apply the tabulated values, the Xe position within a MOFs can be related to the respective relative position of the model. Correspondingly, the value of the shielding at this position can be used. This allows a fast evaluation of the chemical shift introduced by Xe-surface interactions for any Xe position, as e.g. obtained from MD simulations.

The second model system is a Zr cluster, combining the SBU of the two MOFs and its adjacent CO₂ groups (see figure 4.7 (b)). This model incorporates the corners of the respective pores (see figure 4.10). With that, the influence of the SBU on the chemical shift of nearby Xe atoms can be studied.

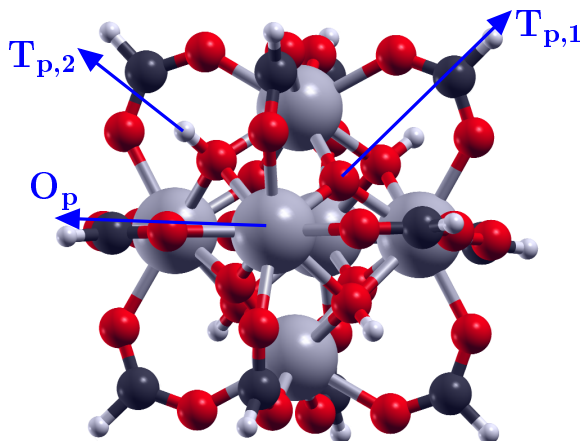


Figure 4.10.: The Zr cluster, a SBU with coordinated CO₂ groups. The directions to the pores are illustrated.

In the T_{p,1} pore, the corner is a μ_3 -O while in the T_{p,2} pore, all corners are made up by a μ_3 -OH. This difference seems small, which is the reason why the tetrahedral pores are usually not distinguished. However, for the description of the chemical shift such differences may have a significant effect. Thus, both pores have been analyzed individually.

In contrast to the T_p pores, the corner of the O_p pore is a blank Zr atom pointing into the pore. Consequently, those three sides need to be analyzed regarding their influence on the chemical shift of Xe.

Again, this was done by placing a single Xe atom at several positions around the model system and calculating the resulting shielding with QE. This allows further tabulation of these shielding values.

Considering the previous investigations, all required model systems have been generated to evaluate the chemical shift of Xe anywhere within the pores of the MOFs. The tabulation includes 300 values for the Xe pair model, about 5500 values for the linker model and roughly 170 values for the Zr cluster.

The significant advantage of those model systems is not just their computational effort, but rather the possibility to treat different influences on the chemical shift individually.

4.4. CHEMICAL SHIFT OF XE IN UIO-66 AND UIO-67

To apply the tabulated values to the MOFs, a consideration of the maximum number of Xe atoms for the pores has to be carried out. For this purpose, the pores can be characterized by their size. The volume of a regular tetrahedron V_T and a regular octahedron V_O with respect to the edge length a are given by

$$V_T = \frac{a^3}{6\sqrt{2}} \quad (4.1)$$

$$V_O = \frac{\sqrt{2}a^3}{3} = 4 \cdot V_T. \quad (4.2)$$

As a first approximation for the filling of the MOFs, a simplified picture can be considered. Each pore can be treated as an idealized tetrahedron or octahedron with a certain edge length. An initial edge length can be defined as the distance between oxygen atoms of adjacent CO_2 groups. This corresponds to the O-O distance within the linker, see e.g. figure 4.9. With that, values of $a_{\text{UiO-66}} = 6.96 \text{ \AA}$ and $a_{\text{UiO-67}} = 11.29 \text{ \AA}$ are obtained. These values can be used to estimate the accessible volume per pore (see table 4.5) and to approximate a maximum amount of Xe atoms which can be placed inside this volume.

Table 4.5.: Volumes of the pores (T and O) for UiO-66 and UiO-67 for a specific edge length. In this estimation, there is no differentiation between the two tetrahedral pores.

UiO-66		UiO-67	
$V_T [\text{\AA}^3]$	$V_O [\text{\AA}^3]$	$V_T [\text{\AA}^3]$	$V_O [\text{\AA}^3]$
39.79	159.15	169.57	678.29

For this approximation, the vdW radius of a Xe atom has to be considered ($r_{\text{vdW,Xe}} = 2.16 \text{ \AA}$ [73]). Thus, a Xe atom occupies a volume of $V_{\text{Xe}} = \frac{4}{3}\pi r_{\text{vdW,Xe}}^3 \approx 42.21 \text{ \AA}^3$. Accordingly, there can only be one Xe atom in the T_p pore and four in the O_p pore in UiO-66. On the other hand, four Xe per T_p pore and 16 per O_p pore can occupy the pore volume in UiO-67.

However, geometrical constraints need to be considered. The argumentation for the T_p pores in this respect does not change and the number of Xe atoms is the same as before. In contrast, the linker in the O_p is sticking into the pore, reducing the accessible volume. Further analysis shows that those restrictions lead to only two Xe atoms within the O_p pore in UiO-66 and seven Xe atoms in the respective pore of UiO-67.

These values were used for a first verification of the introduced model systems. For this purpose, the pores have been filled with the amount of Xe atoms as explained above. Afterwards, the magnetic shielding of each Xe atom has been calculated with QE. With that, the chemical shift δ_{QE} was obtained. Additionally, the summed up values of the model systems were used to evaluate δ_{models} .

The results can be found in table 4.6. It should be noted that these values do not represent the experimental situation. The Xe atoms were placed into the pores by hand. With that, the only purpose of this table is to evaluate the model systems.

As can be seen from table 4.6, the values for the chemical shift comparing δ_{QE} and δ_{models} agree well. With this verification of the tabulated values, the model systems were further applied to the completely filled pores as will be discussed next.

Table 4.6.: Comparison of the chemical shift of Xe atoms inside the pores of UiO-66 and UiO-67. Derived from the model systems (δ_{models}) and from calculations with QE (δ_{QE}). All values are given in ppm.

	UiO-66		UiO-67	
	δ_{models}	δ_{QE}	δ_{models}	δ_{QE}
$\delta_{\text{T}_{\text{p},1}}$	-5.46	-7.95	+49.79	+67.82
$\delta_{\text{T}_{\text{p},2}}$	-5.22	-4.95	+25.45	+31.85
$\delta_{\text{O}_{\text{p}}}$	+93.31	+86.97	+59.81	+54.91
δ_{average}	+43.33	+40.25	+47.98	+52.90
difference [%]	7		9	

Within the initial consideration the orientations of the linkers, the twist of the linkers in UiO-67 and the fact that atoms are not hard spheres were neglected. Thus, it is probable that a different amount of Xe atoms can be placed inside the different pores.

To analyze this behavior further, several MDs were performed on the UiOs. For each MD, a different amount of Xe atoms was placed in the pores of the MOFs. The stability of the resulting systems was analyzed. Once a system cannot equilibrate anymore, the maximum amount of atoms is exceeded. With this ansatz, a new distribution of Xe atoms is found.

For the T_{p} pores, the same argumentation as before holds. The tetrahedral environment does not allow more Xe atoms to enter this pore. Thus, for UiO-66 there is one Xe atom while in UiO-67 there are 4 Xe atoms in such pores. However, for the O_{p} pores a different behavior is observed. In UiO-66, six Xe atoms can fit inside this pore, occupying each of the six corners. For UiO-67, the number increases to 12 atoms. In detail, six Xe atoms are at the corners of the pore and six are further inside the pore. All results are summarized in table 4.7.

Table 4.7.: The maximum number of Xe atoms inside the pores of UiO-66 and UiO-67. N_{init} is derived from a comparison between the volume of the pore and the Xe atom (see table 4.5). For $N_{\text{Xe,geo}}$, geometrical constraints are considered. The final amount of Xe atoms, as derived from molecular dynamics, is denoted as $N_{\text{Xe,MD}}$.

pore	UiO-66			UiO-67		
	N_{init}	$N_{\text{Xe,geo}}$	$N_{\text{Xe,MD}}$	N_{init}	$N_{\text{Xe,geo}}$	$N_{\text{Xe,MD}}$
$\text{T}_{\text{p},1}$	1	1	1	4	4	4
$\text{T}_{\text{p},2}$	1	1	1	4	4	4
O_{p}	4	2	6	16	7	12

Considering the two MOFs UiO-66 and UiO-67, experiments find a decrease of the chemical shift from $\delta_{\text{UiO-66}} = 280$ ppm to $\delta_{\text{UiO-67}} = 245$ ppm. However, experiments are limited to the measurement of the average chemical shift. Thus, the model systems can provide an atomistic description of the chemical shift as introduced by several sources (Xe-Xe and Xe-surface interactions).

The maximum number of Xe atoms (see table 4.7) was taken for further investigations. This number represent the high-pressure limit. Molecular dynamics (MDs) simulations were used to determine the distribution of Xe atoms within each pore under experimental conditions ($T = 237$ K, $p = 1.73$ MPa). An equilibration time of 20 ps was employed for all MD simulations. The obtained distribution of Xe atoms was used to analyze the chemical shift. This was done considering different contributions ($\delta_{\text{Xe-Xe}}$, δ_{S}) in the different pores of the MOFs, explaining the experimental behavior. The results are summarized in table 4.8 and visualized in figure 4.11.

Table 4.8.: Chemical shifts within the pores of UiO-66 and UiO-67 as evaluated with the model systems. All values are given in ppm.

The maximum amount of Xe atoms was used, representing the high-pressure limit. An individual analysis of the different contributions to the chemical shift is carried out. Accordingly, $\delta_{\text{Xe-Xe}}$ denotes the shift as introduced by Xe-Xe interactions, $\delta_{\text{S,linker}}$ is the shift which originates from Xe-linker interactions and $\delta_{\text{S,SBU}}$ is the corresponding shift from Xe-SBU interactions. The presented values for $\delta_{\text{Xe-Xe}}$, $\delta_{\text{S,linker}}$ and $\delta_{\text{S,SBU}}$ are the average over all Xe atoms per pore (in O_p for UiO-67 this is carried out more explicit, as different shifts occur for the outer (first value) and inner (second value) Xe atoms). All values contribute to a chemical shift per pore (highlighted in blue). The total chemical shift (highlighted **bold**) can be obtained by averaging the chemical shifts per pore over the number of atoms per pore. The differences between UiO-67 and UiO-66 are given as $\Delta\delta$.

pore	contribution	UiO-66	UiO-67	$\Delta\delta$
$T_{p,1}$	$\delta_{\text{Xe-Xe}}$	—	0	—
	$\delta_{\text{S,linker}}$	$3 \times 49 = 147$	$3 \times 46 = 138$	-9
	$\delta_{\text{S,SBU}}$	100	156	+56
	$\delta_{\text{total},T_{p,1}}$	247	294	+47
$T_{p,2}$	$\delta_{\text{Xe-Xe}}$	—	0	—
	$\delta_{\text{S,linker}}$	$3 \times 41 = 123$	$3 \times 35 = 105$	-18
	$\delta_{\text{S,SBU}}$	62	106	+44
	$\delta_{\text{total},T_{p,2}}$	185	211	+26
O_p	$\delta_{\text{Xe-Xe}}$	72	$\frac{6 \times 143 + 6 \times 190}{12} = 166$	+94
	$\delta_{\text{S,linker}}$	$4 \times 56 = 224$	$\frac{6 \times (4 \times 53) + 6 \times 0}{12} = 106$	-118
	$\delta_{\text{S,SBU}}$	69	$\frac{6 \times 90 + 6 \times 0}{12} = 45$	-24
	$\delta_{\text{total},O_p}$	365	317	-48
	$\delta_{\text{total,theo}}$	328	291	-37
	$\delta_{\text{total,exp}}$	280	245	-35

Chemical shift in the tetrahedral pores Starting with the analysis of the tetrahedral pores, an increase in the chemical shift for $T_{p,1}$ ($\Delta\delta \approx +47$ ppm) and $T_{p,2}$ ($\Delta\delta \approx +26$ ppm) comparing UiO-67 with UiO-66 has been found. The model systems allow to evaluate this behavior by analyzing the distribution of the Xe atoms within these pores. Firstly, there is no difference of the Xe-Xe contributions between UiO-66 and UiO-67. This is due to the fact that there is only one Xe atom present inside the T_p of UiO-66, i.e. there is no Xe-Xe interaction. On the other hand for UiO-67, the equilibrated averaged distances between the four Xe atoms within such pores are large (circa 8 Å). Accordingly, the contributions to the chemical shift negligible.

Analyzing the contributions to the chemical shift from Xe-surface interactions, quite strong differences between the MOFs were found. Because there is only one Xe atom per T_p pore in UiO-66, this atom tends to go towards any corner of the pores. Such positions are energetically more favourable due to Xe-MOF interactions than the middle of the pore (see Appendix 13). However, the geometry of the pore does not imply any strict localization of the atom. Due to the temperature the atom can move rather freely, leading on average to an increased distance to the corners and thus to the SBU in comparison to UiO-67. Correspondingly, the contributions to the shift from this source is smaller, with values of $\delta_{S,SBU,UiO-66}(T_{p,1}) \approx 100$ ppm and $\delta_{S,SBU,UiO-66}(T_{p,2}) \approx 62$ ppm.

For UiO-67, a different distribution of Xe atoms occurs in comparison to UiO-66. Due to the larger available space, each of the four corners in the T_p pore is occupied by one Xe atom. With that, there is a strict localization for all Xe atoms. This leads to a smaller average distance to the SBU in comparison to UiO-66. Thus, the contribution from this source is larger with $\delta_{S,SBU,UiO-67}(T_{p,1}) \approx 156$ ppm and $\delta_{S,SBU,UiO-67}(T_{p,2}) \approx 106$ ppm.

Considering the influence of the linkers on the shift, the average position of the Xe atom in UiO-66 leads to a slightly larger shift from the linkers. The respective values are $\delta_{S,linker,UiO-66}(T_{p,1}) \approx 147$ ppm and $\delta_{S,linker,UiO-66}(T_{p,2}) \approx 123$ ppm. The contributions from the linkers in UiO-67 are similar to UiO-66. However, they becomes slightly smaller, resulting in $\delta_{S,linker,UiO-67}(T_{p,1}) \approx 138$ ppm and $\delta_{S,linker,UiO-67}(T_{p,2}) \approx 105$ ppm.

The difference of the shift between the two tetrahedral pores has two main reasons. Firstly, $T_{p,2}$ is slightly larger than $T_{p,1}$, thus the Xe atom has more space to move. Secondly, the corners are different, as mentioned before. In $T_{p,1}$, there is a μ_3 -O allowing the Xe atom to come rather close to the SBU. On the other hand, the corner in $T_{p,2}$ is a μ_3 -OH. The hydrogen atom sticks into the pore, hindering the Xe atom to come as close to the SBU. Additionally, the influence of the hydrogen atom on the chemical shift is smaller compared to the μ_3 -O. With that, an overall decrease of the chemical shift in $T_{p,2}$ occurs.

This point shall be discussed in more detail. As mentioned before, the two pores are slightly different considering their geometries. However, the effect of those geometries on the chemical shift is significant. Therefore, each pore had to be analyzed individually.

In summary, the investigations show that the Xe-Xe contribution is negligible in both MOFs considering the T_p pores. The Xe-linker effect is similar, even though it becomes slightly larger in UiO-66, especially in $T_{p,2}$. The opposite is observed for the Xe-SBU influence, which becomes significantly larger in UiO-67 due to the strict localization of the Xe atoms in all corners of these pores. This leads to an increase of the chemical shift in UiO-67.

Chemical shift in the octahedral pores The investigations of the chemical shift in the octahedral pores show a different behavior in comparison to the tetrahedral pores. A decrease of the chemical shift ($\Delta\delta \approx -48$ ppm) comparing UiO-67 and UiO-66 has been found. The discussion will again be based on the distribution of the Xe atoms within the pores. First of all, the Xe-Xe interactions are significant. In UiO-66, there are six Xe atoms within the O_p . All six corners of this pore are occupied by one Xe atom (in analogy to the T_p in UiO-67). Due to larger Xe-Xe distances in comparison to UiO-67, a smaller influence from the Xe-Xe interactions was obtained, resulting in a value of $\delta_{\text{Xe-Xe,UiO-66}}(O_p) \approx 72$ ppm.

The distribution of the Xe atoms in UiO-67 considering the O_p is different. There are twelve Xe atoms in this pore, where six are at the corners (outer atoms) while six are further inside the pore (inner atoms). This distribution of Xe atoms leads to a strong increase of the Xe-Xe influence in contrast to UiO-66. The contribution to the outer atoms is smaller due to the smaller amount of neighboring Xe atoms, resulting in a shift of approximately 143 ppm. In contrast, the inner atoms have more neighbors, which increases the average chemical shift of them to ca. 190 ppm. Thus, averaging these values over the number of contributing atoms gives a value of $\delta_{\text{Xe-Xe,UiO-67}}(O_p) \approx 166$ ppm, which is significantly larger than the respective contribution in UiO-66.

For the consideration of the Xe-surface interactions, an influence of the SBU on the shift in UiO-66 is given by $\delta_{\text{S,SBU,UiO-66}}(O_p) \approx 69$ ppm.

In UiO-67, the average distance of the outer atoms to the SBU becomes smaller due to the additional interaction with the inner atoms. This results in a larger contribution to the chemical shift with a value of approximately 90 ppm. However, the inner atoms do not experience any influence of the surface. Consequently, their contribution to the chemical shift is zero. Thus, on average the chemical shift as introduced by the SBU reduces in UiO-67 to $\delta_{\text{S,SBU,UiO-67}}(O_p) \approx 45$ ppm.

This effect can be seen more severely for the influence of the linkers. In UiO-66, this influence leads to a large chemical shift of $\delta_{\text{S,linker,UiO-66}}(O_p) \approx 224$ ppm. The influence on the outer atoms in UiO-67 is very similar with a value of ca. 212 ppm. But again the contribution on the inner atoms is negligible, resulting in an average chemical shift of $\delta_{\text{S,linker,UiO-67}}(O_p) \approx 106$ ppm. Thus, the chemical shift in UiO-67 becomes significantly smaller than the corresponding value in UiO-66. Remarkably, this decrease only happens due to the averaging over all Xe atoms and cannot be contributed to a decrease of the chemical shift of all atoms.

In summary, the Xe-Xe interactions in UiO-67 are much more pronounced in comparison to UiO-66, leading to a significantly larger contribution of $\delta_{\text{Xe-Xe}}$. However, even though there are more Xe atoms within the O_p in UiO-67, the chemical shift within this pore is reduced. This is due to the fact that the global average over all Xe atoms has to be considered to be comparable to the experiments. Although the contributions to the chemical shift considering the outer atoms in UiO-67 are equal or even larger compared to UiO-66, the averaging over all Xe atoms leads to a smaller chemical shift for the entire pore.

Averaging all contributions - comparison to experiment For comparison with the experimental data, the average of the chemical shift per pore with respect to the corresponding number of Xe atoms per pore has to be evaluated. This results in

$$\begin{aligned}\delta_{\text{total,UiO-66}} &= (1 \times \delta_{\text{total,Tp,1}} + 1 \times \delta_{\text{total,Tp,2}} + 6 \times \delta_{\text{total,Op}})/8 \\ &= (1 \times 247 \text{ ppm} + 1 \times 185 \text{ ppm} + 6 \times 365 \text{ ppm})/8 = 328 \text{ ppm} \\ \delta_{\text{total,UiO-67}} &= (4 \times \delta_{\text{total,Tp,1}} + 4 \times \delta_{\text{total,Tp,2}} + 6 \times \delta_{\text{outer,Op}} + 6 \times \delta_{\text{inner,Op}})/20 \\ &= (4 \times 294 \text{ ppm} + 4 \times 211 \text{ ppm} + 6 \times 445 \text{ ppm} + 6 \times 190 \text{ ppm})/20 \\ &= (4 \times 294 \text{ ppm} + 4 \times 211 \text{ ppm} + 12 \times 317 \text{ ppm})/20 = 291 \text{ ppm}.\end{aligned}$$

The chemical shift becomes smaller in UiO-67 compared to UiO-66, in correspondence to the experimental results. However, the analysis of the model systems provides individual contributions to the chemical shift. This allows a thorough analysis of all contributions and an explanation of the experimental observation. The absolute values between the theoretical predictions and the experimental data differ, i.e. the theoretical values are too large. However, comparing the difference of the shift between UiO-67 and UiO-66, an experimental value of $\Delta\delta_{\text{tot,exp}} = -35 \text{ ppm}$ is found. From the theoretical approach, a value of $\Delta\delta_{\text{tot,theo}} = -37 \text{ ppm}$ is obtained (see inset in figure 4.11). Thus, the relative difference agrees well between both theory and experiment.

In the inset of figure 4.11, the theoretical values were subtracted by 47 ppm. This corresponds to the difference between the theoretical and the experimental values, which occurs consistently for both MOFs (see table 4.8).

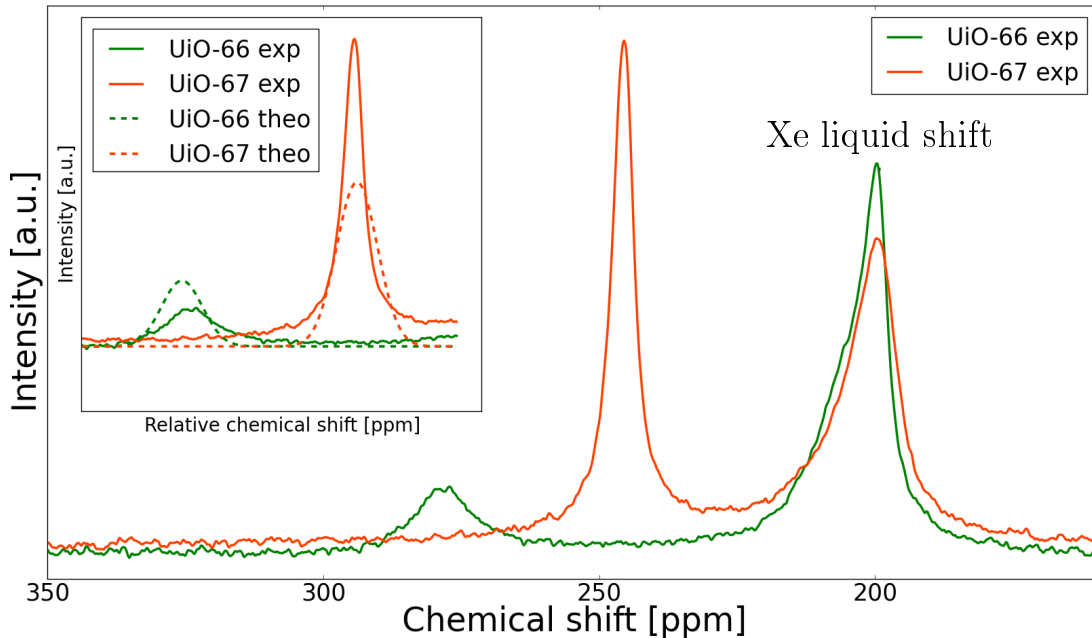


Figure 4.11.: Comparison of the theoretically predicted (theo) and the measured (exp) NMR spectra. The inset shows the relative chemical shift, visualizing the difference between the chemical shift of UiO-66 and UiO-67 from theory and experiment. A good agreement has been found, while the theoretical investigations can explain the difference at an atomistic level.

There are 8 Xe atoms per primitive unit cell in UiO-66 and 20 Xe atoms per primitive unit cell in UiO-67. With that, the ratio of Xe atoms comparing UiO-67 and UiO-66 is 2.5. The resulting intensity of the NMR signal for UiO-67 should be 2.5 times larger in comparison to UiO-66. In the measurements, a ratio $I_{\text{UiO-67}} \approx 8I_{\text{UiO-66}}$ is found. However, the intensities depend on numerous factors and are difficult to correct. As the experiments were not intended to improve the intensities, but to measure the chemical shift, it shall only be noted here that a ratio of 2.5 would match the theoretical prediction.

Considering the absolute values of the chemical shift, numerous reasons for the difference between theoretical and experimental values occur. All theoretical investigations were based on the idealized crystalline structures. From these structures, the model systems were derived. With that, all considered systems were either entirely periodic or completely isolated. Structural deviations from the idealized structure, such as defects, were not implemented in the theoretical investigations. As experiments used the MOFs as powders, the crystallinity is reduced. This might cause surface effects which have not been analyzed with the model systems to play a role. Such effects will influence the chemical shift in ways which were not covered with the theoretical ansatz.

Additionally, as seen from the investigations of the Xe liquid shift (which agrees well between theory and experiment) it seems that the model systems for δ_{S} systematically give a too large value of the chemical shift. Further, chemical shifts obtained from calculations with QE are in general too large (see initial NMR investigation, section 4.2). In addition, the CO₂ groups are part of the linker as well as of the Zr cluster model (see figure 5.2). Thus, the influence of this structural unit might be counted twice. This further leads to consistently too large chemical shifts. However, the difference between the two MOFs is entirely recovered as mentioned before, which was the main purpose of the investigation.

Taking all those considerations into account, the model systems allow a full analysis of the chemical shift of Xe within the metal-organic frameworks UiO-66 and UiO-67. An explanation of the experimental behavior was found at an atomistic level. The theoretical approach allows an insight which is not accessible by experimental methods. Furthermore, this approach should be transferable to other MOFs, like UiO-68.



PART V.

CONCLUSION AND OUTLOOK

Within this thesis, several theoretical investigations regarding different magnetic properties in metal-organic frameworks (MOFs) were carried out. Most calculations were performed in the framework of density functional theory (DFT) (see section 2.1).

The magnetism in MOFs can be classified based on its origin. Some structures have an intrinsic, electronic magnetism due to spin-spin coupling of their metal centers. Once unpaired electrons on different metal centers occur, they will interact magnetically. To describe such magnetism, spin-polarized DFT calculations have been employed to compare ground state energies of a system with a low-spin (antiferromagnetic) and a high-spin (ferromagnetic) magnetic ordering. This identifies which magnetic ordering is energetically more favourable. Based on these calculations, the magnetic coupling can be further analyzed by the formalism of a Heisenberg-Dirac-Van Vleck Hamiltonian (see section 2.5.1).

Another property is introduced by the electronic cloud around an atom, which influences an external magnetic field due to induced orbital currents. This concept is called magnetic shielding and is the basis of NMR investigations (see section 2.2). Changes in the magnetic shielding due to the interactions with a chemical environment are referred to as chemical shift (see section 2.6.2). This property can be measured to a high degree of accuracy and can be calculated using theoretical methods (see section 2.4). This enables the possibility to approach a certain problem from both theoretical and experimental sides.

DUT-8(Ni) In the first part of this thesis, the electronic and magnetic structure of the MOF DUT-8(Ni) (DUT - Dresden University of Technology) was analyzed. This MOF is flexible and consequently exists in two stable configurations, namely DUT-8(Ni)_{open} and DUT-8(Ni)_{closed}.

Initial considerations were concerned with the analysis of the magnetic ground state of each configuration, i.e. the magnetic coupling between the two Ni atoms which form the secondary building unit (SBU) (see section 3.3). As this ground state remained unclear from the experimental side, calculations considering different magnetic orderings were carried out to determine the energetically most favourable one. The investigations were based on initial as well as fully optimized structures (see section 3.1). This ensured a full overview of the magnetic interactions in similar chemical environments with different distances between the magnetic centers.

Furthermore, the well known concept of the Heisenberg-Dirac-Van Vleck Hamiltonian as a model Hamiltonian has been employed to analyze the strength of the coupling (the coupling constant J_{ij}). The coupling was found to be antiferromagnetic/ low-spin in both configurations of DUT-8(Ni), such that the spins at the two Ni atoms align antiparallel. The strength of the coupling is in the order of several hundred cm^{-1} (see section 3.3).

In a next step, model systems have been derived from the crystal structures (see section 3.5). The model systems were constructed considering only the constituents which contribute to the magnetism, i.e. the metal centers and their chemical environment. Based on these model systems, changes were implied to the chemical environment to study the effects on the magnetic coupling (see sections 3.5.1 and 3.5.2) while reducing computational time. The entire approach is visualized in figure 5.1.

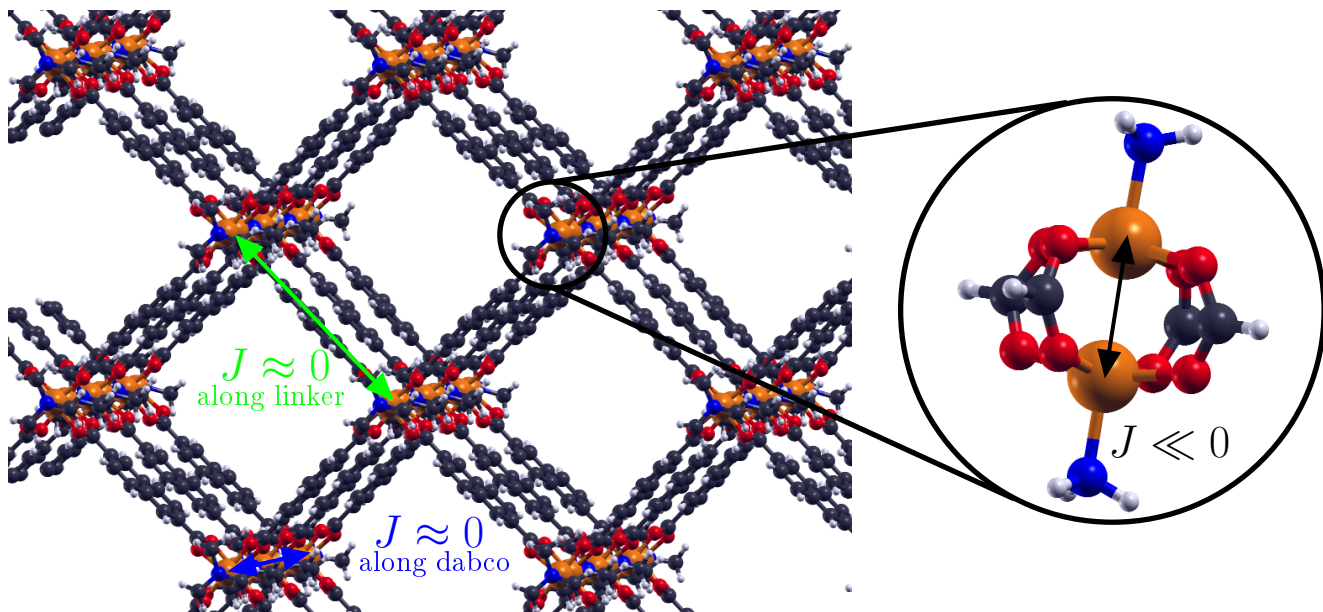


Figure 5.1.: Comparison between the coupling constant along the linkers, along the dabco unit and between the Ni atoms of one SBU within the crystal structure of DUT-8(Ni). This figure shows that the separation of the model systems to describe the intrinsic magnetism is justified, as there are negligible influences on the local magnetism by adjacent SBUs.

The molecular models represent the electronic and especially the magnetic structure of the respective crystalline structures, while containing only a fraction of the amount of atoms (132 atoms per unit cell for DUT-8(Ni)_{open}, 66 atoms per unit cell for DUT-8(Ni)_{closed} and 26 atoms for the model systems). Additionally, such models can be modified to determine how alterations of the chemical environment change the magnetic coupling of the two Ni centers.

As seen in sections 3.5.1 and 3.5.2, such changes have a major effect on the coupling, modifying it from the low-spin to a high-spin state by implying several alterations. Some of the modifications could be introduced in experimental setups, like defects.

Further analysis included a replacement of the transition metal atoms, giving rise to a HS coupling between the magnetic centers. The SBUs within the MOF and with that the magnetism therein are well localized. Considerations concerning long-range magnetic interactions of HS-SBUs were performed at the end of the first part of this thesis (see section 3.5.3). These investigations show that the magnetism per SBU is stable and no long-range ordering occurs. This might allow to build a HS-MOF with highly localized spin sites, which could be used e.g. in memory storage devices. Thus, if the mentioned HS-MOFs could be created, the HS-SBUs would generate stable local spin sites.

Further investigations should include a study on the stability of the HS-SBUs in the existing geometry of DUT-8(Ni) or even find a new geometry (different chemical environment) which stabilizes the magnetic properties. Furthermore, it could be analyzed experimentally whether the implementation of the proposed alterations lead to the theoretically predicted HS coupling.

UiO-66 and UiO-67 The second part of this thesis was concerned with the magnetic shielding and consequently the chemical shift of ^{129}Xe inside the MOFs UiO-66 and UiO-67. High-pressure NMR experiments observed a decrease of the chemical shift comparing UiO-67 to UiO-66. To analyze this behavior theoretically, model systems have been employed. These models included a simple Xe pair model, which is able to accurately predict the chemical shift as introduced by adjacent Xe atoms. This has been verified by analyzing the chemical shift of Xe in its liquid phase, which is found in experiment (at $T = 237$ K and $p = 1.73$ MPa) to be $\delta_{\text{exp}} = 203$ ppm. With Monte-Carlo simulations employing a NPT ensemble, a value of $\delta_{\text{theo}} \approx 200$ ppm has been obtained. Thus, the Xe pair model was validated.

Further model systems were employed to simulate the surface inside the pores of the MOFs, as seen in figure 5.2. These models were used to analyze the chemical shift of Xe at several positions relative to each model. With that, a tabulation of the chemical shift in relative positions to structural elements within the pores of the MOFs was performed. By adding the different contributions together, the chemical shift inside the MOFs for each Xe at any position was investigated (this approach is based on the investigations by Ito and Fraissard [59]). With that, not just the total average chemical shift per MOF was analyzed (as in experiments) but several different contributions within the different pores were evaluated individually.

Finally, a thorough investigation at the atomistic level has been carried out. The difference between the chemical shift of UiO-66 and UiO-67 coincides with the experimental one. However, with the generated model systems it is possible to describe different influences in the different pores of the MOFs. This allows a fundamental understanding of all influences on the chemical shift. With that, complete explanation of the observed behavior was provided, which would not be possible in experiments due to the limitations to measure only the total (average) chemical shift.

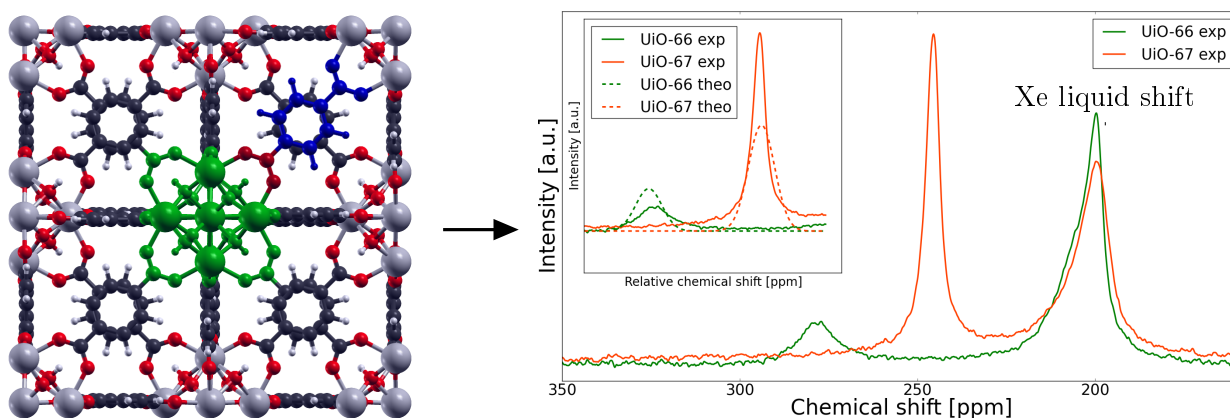


Figure 5.2.: Highlight of the linker (blue) as well as the Zr cluster (green) in UiO-66. Together with the Xe pair model, the NMR spectra of ^{129}Xe in UiO-66 and UiO-67 was calculated at an atomistic level.

For future investigations, the model systems could be used together with GCMC (grand canonical Monte-Carlo) simulations to analyze the adsorption isotherms for the chemical shift within UiO-66 and UiO-67. These isotherms can be compared with experiments. On the one hand this would provide further insights into the behavior of the Xe chemical shift at lower pressure. On the other hand the models systems could be further verified. Additionally, the model systems could be transferred to similar systems (such as UiO-68) to analyze the chemical shift in an isostructural system and further verify their accuracy.

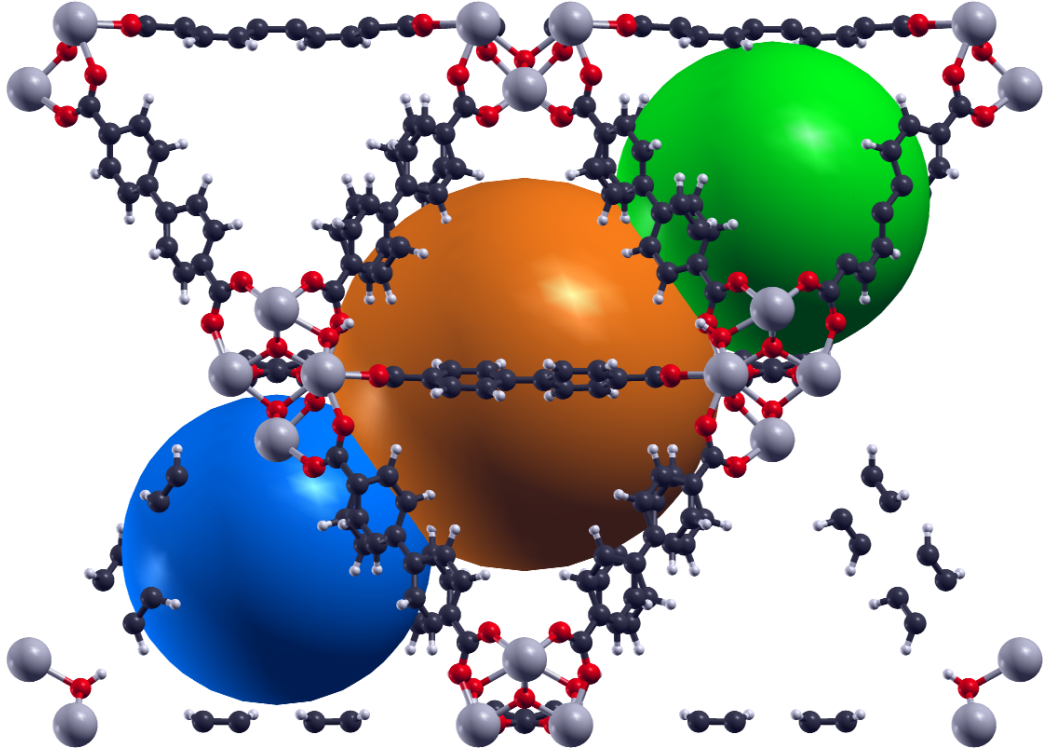
PART VI.

APPENDICES

APPENDIX INDICES

- Appendix 1 Visualization of the tetrahedral and octahedral pores in UiO-67. Additionally, comparison of the initial and fully relaxed structures of UiO-66 and UiO-67
- Appendix 2 Considerations regarding the Heisenberg Hamiltonian
- Appendix 3 Convergence tests
- Appendix 4 Binding energies for all metal-organic frameworks
- Appendix 5 Supercell calculations for the initial structures of DUT-8(Ni)
- Appendix 6 All energies and J_{ij} values for the models of DUT-8(Ni)
- Appendix 7 Considerations for M1 and its verification
- Appendix 8 Modelling defects with the initial DUT-8(Ni)_{open} models
- Appendix 9 Influence of long-range magnetic interactions for DUT-8(Ni)_{open,init} model
- Appendix 10 Energies for the double SBU model systems from QE and FPLO
- Appendix 11 Hartree-Fock-Slater calculations for the $\frac{1}{r}$ dependence of σ for Xe
- Appendix 12 Calculations of the chemical shift of Xe around benzene
- Appendix 13 Energetically favourable positions in UiO-66 and UiO-67
- Appendix 14 Calculation of the porosity for all MOFs

APPENDIX 1



(a) UiO-67 along xz

Figure 6.1.: UiO-67 shown along the xz direction to visualize the octahedral and tetrahedral pores. Only one pore each is highlighted. The overlap of the spheres is attributed to the fact that spheres are used to fill tetrahedral and octahedral environments.

Table 6.1.: Comparison of distances [\AA], angles [$^\circ$] and cell volume [\AA^3] for the initial structures of UiO-66 [28] and UiO-67 [30] as well as the full variable cell relaxation in QE. No significant differences are found. The deviation is calculated like deviation = $(1 - \frac{\text{relaxed}}{\text{initial}}) \times 100\%$.

	UiO-66			UiO-67		
	initial	relaxed	deviation [%]	initial	relaxed	deviation [%]
$d_{\text{Zr,Zr short}}$	3.572	3.539	0.924	3.571	3.540	0.868
$d_{\text{Zr,Zr long}}$	5.052	5.006	0.911	5.050	5.006	0.871
$d_{\text{Zr,O cluster}}$	2.089	2.075	0.670	2.089	2.075	0.670
$d_{\text{Zr,OH cluster}}$	2.286	2.273	0.569	2.285	2.273	0.525
$d_{\text{Zr,O linker}}$	2.248	2.242	0.267	2.252	2.246	0.266
$d_{\text{C,O}}$	1.273	1.275	-0.157	1.272	1.274	-0.157
$d_{\text{C,H}}$	1.084	1.089	-0.461	1.085	1.090	-0.461
$\angle_{\text{O,C,O}}$	125.249	125.567	-0.254	125.255	125.648	-0.314
$\angle_{\text{C,C,C middle}}$	—	—	—	31.470	29.303	6.886
V_{cell}	2308.113	2288.469	0.851	4972.434	4928.750	0.879

APPENDIX 2

COMPARISON BETWEEN HEISENBERG AND ISING MODEL

In the following section, a comparison between the Ising and the Heisenberg model will be carried out to highlight the differences of those models even for simple cases. The easiest possible system, which consists of two interacting spins with $S_1 = S_2 = \frac{1}{2}$, will be taken to evaluate those differences. The Hilbert space basis of such a system is $|\uparrow\uparrow\rangle, |\uparrow\downarrow\rangle, |\downarrow\uparrow\rangle, |\downarrow\downarrow\rangle$ resulting in a four-dimensional Hamiltonian. For the Ising model (taking only z into account, $\gamma = 0$, see equation (2.47)) the following Hamiltonian occurs

$$\hat{H}_{\text{Ising}} = -2J_{12}(S_{1,z}S_{2,z}). \quad (6.1)$$

As the eigenvalues of S_z are known to be $S_z |\pm\rangle = m_S |\pm\rangle$ (using atomic units with $\hbar = 1$), where m_S is the spin quantum number with $m_S = \pm\frac{1}{2}$ and the \pm indicates either spin up (\uparrow) or spin down (\downarrow), the already mentioned basis can be used to gain the interaction matrix for the Ising model

$S_{1,z}S_{2,z}$	$\uparrow\uparrow$	$\uparrow\downarrow$	$\downarrow\uparrow$	$\downarrow\downarrow$
$\uparrow\uparrow$	$\frac{1}{4}$	0	0	0
$\uparrow\downarrow$	0	$-\frac{1}{4}$	0	0
$\downarrow\uparrow$	0	0	$-\frac{1}{4}$	0
$\downarrow\downarrow$	0	0	0	$\frac{1}{4}$

This gives the Ising Hamiltonian like

$$\hat{H}_{\text{Ising}} = -\frac{J}{2} \begin{pmatrix} 1 & 0 & 0 & 0 \\ 0 & -1 & 0 & 0 \\ 0 & 0 & -1 & 0 \\ 0 & 0 & 0 & 1 \end{pmatrix}.$$

Calculating the energy eigenvalues for this matrix yields $E_{1,2} = \pm\frac{J}{2}$, leading to an energy difference between the FM and the AFM state of $\Delta E = J$.

With $\gamma = 1$, the Heisenberg model is obtained. The corresponding Hamiltonian is

$$\hat{H}_{\text{Heisenberg}} = -2J_{12} (S_{1,x}S_{2,x} + S_{1,y}S_{2,y} + S_{1,z}S_{2,z}). \quad (6.2)$$

As S_z commutes with \mathbf{S}^2 but not with $S_{1,x}S_{2,x} + S_{1,y}S_{2,y}$, the latter formulation has to be expressed in a different way. For that purpose, the generation and annihilation operators \hat{S}_+ and \hat{S}_- are introduced

$$\hat{S}_+ = S_x + iS_y \quad (6.3)$$

$$\hat{S}_- = S_x - iS_y, \quad (6.4)$$

acting on a state like [79]

$$\hat{S}_\pm |S, S_z\rangle = \sqrt{S(S+1) - S_z(S_z \pm 1)} |S, S_z \pm 1\rangle. \quad (6.5)$$

It can be shown that the wanted expression can be derived from those operators

$$\frac{1}{2} \left(\hat{S}_{1,+} \hat{S}_{2,-} + \hat{S}_{1,-} \hat{S}_{2,+} \right) = S_{1,x} S_{2,x} + S_{1,y} S_{2,y}. \quad (6.6)$$

From this, an interaction matrix can be defined taking only x and y into account

$$\begin{array}{c|cccc} \frac{1}{2}(\hat{S}_{1,+}\hat{S}_{2,-} + \hat{S}_{1,-}\hat{S}_{2,+}) & \uparrow\uparrow & \uparrow\downarrow & \downarrow\uparrow & \downarrow\downarrow \\ \hline \uparrow\uparrow & 0 & 0 & 0 & 0 \\ \uparrow\downarrow & 0 & 0 & \frac{1}{2} & 0 \\ \downarrow\uparrow & 0 & \frac{1}{2} & 0 & 0 \\ \downarrow\downarrow & 0 & 0 & 0 & 0 \end{array}$$

which creates a Hamiltonian with non-diagonal elements

$$\hat{H}_{x,y} = -\frac{J}{2} \begin{pmatrix} 0 & 0 & 0 & 0 \\ 0 & 0 & 2 & 0 \\ 0 & 2 & 0 & 0 \\ 0 & 0 & 0 & 0 \end{pmatrix}.$$

Using equation (6.6) to replace the expression in equation (6.2) gives

$$\hat{H}_{\text{Heisenberg}} = -2J_{12} \left(\frac{1}{2} \left(\hat{S}_{1,+} \hat{S}_{2,-} + \hat{S}_{1,-} \hat{S}_{2,+} \right) + S_{1,z} S_{2,z} \right). \quad (6.7)$$

Taking into account that

$$\begin{aligned} \hat{S}_+ |m_S\rangle &= |m_S + 1\rangle, \\ \hat{S}_- |m_S\rangle &= |m_S - 1\rangle, \\ \hat{S}_+ |\uparrow\rangle &= 0, \\ \hat{S}_+ |\downarrow\rangle &= |\uparrow\rangle, \\ \hat{S}_- |\uparrow\rangle &= |\downarrow\rangle, \\ \hat{S}_- |\downarrow\rangle &= 0 \end{aligned}$$

leads to an expression of the Hamiltonian like (an explicit calculation of the entries of this Hamiltonian is given in the next section)

$$\hat{H}_{\text{Heisenberg}} = -\frac{J}{2} \begin{pmatrix} 1 & 0 & 0 & 0 \\ 0 & -1 & 2 & 0 \\ 0 & 2 & -1 & 0 \\ 0 & 0 & 0 & 1 \end{pmatrix}.$$

Calculating the eigenvalues shows a singlet state ($S = 0$, AFM) with $E_1 = \frac{3}{2}J$ and a triplet state ($S = 1$, FM) with $E_{2,3,4} = -\frac{1}{2}J$ leading to an energy difference of $\Delta E = 2J$.

The corresponding eigenstates follow as

$$\begin{aligned}
|\uparrow\uparrow\rangle &\rightarrow S = 1, m_S = 1, \\
|\downarrow\downarrow\rangle &\rightarrow S = 1, m_S = -1, \\
\frac{|\uparrow\downarrow\rangle + |\downarrow\uparrow\rangle}{\sqrt{2}} &\rightarrow S = 1, m_S = 0, \\
\frac{|\uparrow\downarrow\rangle - |\downarrow\uparrow\rangle}{\sqrt{2}} &\rightarrow S = 0, m_S = 0.
\end{aligned}$$

In conclusion, this comparison shows that even for this very simple case the results of the two models differ. The Ising model certainly has the advantage of its simplicity, but the Heisenberg model describes the splitting of the levels correctly.

CALCULATION OF THE ENTRIES OF THE HEISEBERG HAMILTONIAN

The calculation of the entries of the Heisenberg spin Hamiltonian shall be carried out here. The discussion is reduced to two particles with $S^1 = S^2 = \frac{1}{2}$. In this case the Hamiltonian is given by

$$\hat{H}_{\text{Heisenberg}} = -2J\mathbf{S}^1 \cdot \mathbf{S}^2 = -2J(S_x^1 S_x^2 + S_y^1 S_y^2 + S_z^1 S_z^2). \quad (6.8)$$

As already mentioned in section 2.5.1 the generation and annihilation operators are used

$$\hat{S}_+ = S_x + iS_y \quad (6.9)$$

$$\hat{S}_- = S_x - iS_y. \quad (6.10)$$

Calculating the products $\hat{S}_+ \cdot \hat{S}_-$ and $\hat{S}_- \cdot \hat{S}_+$ gives

$$\hat{S}_+ \cdot \hat{S}_- = (S_x)^2 + iS_y S_x - S_x iS_y + (S_y)^2 \quad (6.11)$$

$$\hat{S}_- \cdot \hat{S}_+ = (S_x)^2 + S_x iS_y - iS_y S_x + (S_y)^2, \quad (6.12)$$

which can be summed up to obtain

$$\left(\hat{S}_+ \cdot \hat{S}_-\right) + \left(\hat{S}_- \cdot \hat{S}_+\right) = 2(S_x)^2 + 2(S_y)^2 \quad (6.13)$$

$$\left(\hat{S}_+^1 \cdot \hat{S}_-^2\right) + \left(\hat{S}_-^1 \cdot \hat{S}_+^2\right) = 2(S_x^1 S_x^2) + 2(S_y^1 S_y^2), \quad (6.14)$$

leading to the Hamiltonian in the form

$$\hat{H}_{\text{Heisenberg}} = -2J \left(\frac{\left(\hat{S}_+^1 \cdot \hat{S}_-^2\right) + \left(\hat{S}_-^1 \cdot \hat{S}_+^2\right)}{2} + S_z^1 S_z^2 \right). \quad (6.15)$$

It is known that

$$\begin{aligned}\hat{S}_\pm |S, S_z\rangle &= \sqrt{S(S+1) - S_z(S_z \pm 1)} |S, S_z \pm 1\rangle \\ S_z |\pm\rangle &= m_S |\pm\rangle \quad (\hbar = 1),\end{aligned}$$

with $m_S = \pm\frac{1}{2}$ being the spin quantum number, leading to

$$\begin{aligned}\hat{S}_+ |m_S\rangle &= |m_S + 1\rangle \\ \hat{S}_- |m_S\rangle &= |m_S - 1\rangle \\ \hat{S}_+ |\uparrow\rangle &= 0 \\ \hat{S}_+ |\downarrow\rangle &= |\uparrow\rangle \\ \hat{S}_- |\uparrow\rangle &= |\downarrow\rangle \\ \hat{S}_- |\downarrow\rangle &= 0 \\ S_z |\uparrow\rangle &= +\frac{1}{2} |\uparrow\rangle \\ S_z |\downarrow\rangle &= -\frac{1}{2} |\downarrow\rangle \\ \langle\uparrow|\uparrow\rangle &= 1 \\ \langle\uparrow|\downarrow\rangle &= 0.\end{aligned}$$

For the considered case, the relations for \hat{S}_+ and \hat{S}_- can be written out like

$$\hat{S}_+ |\uparrow\rangle = \sqrt{\frac{1}{2} \binom{3}{\frac{3}{2}} - \frac{1}{2} \binom{3}{\frac{3}{2}}} \left| \frac{1}{2}, \frac{3}{2} \right\rangle = 0 \quad (6.16)$$

$$\hat{S}_+ |\downarrow\rangle = \sqrt{\frac{1}{2} \binom{3}{\frac{3}{2}} - \left(-\frac{1}{2}\right) \binom{1}{\frac{1}{2}}} \left| \frac{1}{2}, \frac{1}{2} \right\rangle = 1 |\uparrow\rangle \quad (6.17)$$

$$\hat{S}_- |\uparrow\rangle = \sqrt{\frac{1}{2} \binom{3}{\frac{3}{2}} - \frac{1}{2} \binom{-1}{-\frac{1}{2}}} \left| \frac{1}{2}, -\frac{1}{2} \right\rangle = 1 |\downarrow\rangle \quad (6.18)$$

$$\hat{S}_- |\downarrow\rangle = \sqrt{\frac{1}{2} \binom{3}{\frac{3}{2}} - \left(-\frac{1}{2}\right) \binom{-3}{-\frac{3}{2}}} \left| \frac{1}{2}, -\frac{3}{2} \right\rangle = 0. \quad (6.19)$$

As in this case S_z can only have values of $\pm\frac{1}{2}$, the values $S_z = \pm\frac{3}{2}$ are forbidden. The basis for the Hamiltonian is given by $|\uparrow\uparrow\rangle, |\uparrow\downarrow\rangle, |\downarrow\uparrow\rangle, |\downarrow\downarrow\rangle$ and thus the interaction matrix can be expressed like

$$\begin{array}{c|cccc} & \uparrow\uparrow & \uparrow\downarrow & \downarrow\uparrow & \downarrow\downarrow \\ \hline \uparrow\uparrow & & & & \\ \uparrow\downarrow & & & & \\ \downarrow\uparrow & & & & \\ \downarrow\downarrow & & & & \end{array}$$

Considering the element between $\uparrow\uparrow$ and $\uparrow\uparrow$ gives

$$\begin{aligned}
\langle \uparrow\uparrow | \hat{H}_{\text{Heisenberg}} | \uparrow\uparrow \rangle &= \langle \uparrow\uparrow | -2J \left(\frac{(\hat{S}_+^1 \cdot \hat{S}_-^2) + (\hat{S}_-^1 \cdot \hat{S}_+^2)}{2} + S_z^1 S_z^2 \right) | \uparrow\uparrow \rangle \\
&= \langle \uparrow\uparrow | -J \hat{S}_+^1 \cdot \hat{S}_-^2 - J \hat{S}_-^1 \cdot \hat{S}_+^2 - 2J S_z^1 S_z^2 | \uparrow\uparrow \rangle \\
&= -J \langle \uparrow\uparrow | \hat{S}_+^1 \cdot \hat{S}_-^2 | \uparrow\uparrow \rangle - J \langle \uparrow\uparrow | \hat{S}_-^1 \cdot \hat{S}_+^2 | \uparrow\uparrow \rangle - 2J \langle \uparrow\uparrow | S_z^1 S_z^2 | \uparrow\uparrow \rangle.
\end{aligned}$$

Treating the terms separately shows

$$\begin{aligned}
-J \langle \uparrow\uparrow | \hat{S}_+^1 \cdot \hat{S}_-^2 | \uparrow\uparrow \rangle &= -J \langle \uparrow\uparrow | 0 \cdot 1 | \uparrow\downarrow \rangle = 0 \\
-J \langle \uparrow\uparrow | \hat{S}_-^1 \cdot \hat{S}_+^2 | \uparrow\uparrow \rangle &= -J \langle \uparrow\uparrow | 1 \cdot 0 | \uparrow\uparrow \rangle = 0 \\
-2J \langle \uparrow\uparrow | S_z^1 S_z^2 | \uparrow\uparrow \rangle &= -2J \langle \uparrow\uparrow | \frac{1}{2} \frac{1}{2} | \uparrow\uparrow \rangle = -\frac{J}{2}.
\end{aligned}$$

Thus the matrix element is $\langle \uparrow\uparrow | \hat{H}_{\text{Heisenberg}} | \uparrow\uparrow \rangle = -\frac{J}{2}$. Accordingly, all other elements can be calculated leading to the Hamiltonian given in previous section.

APPENDIX 3

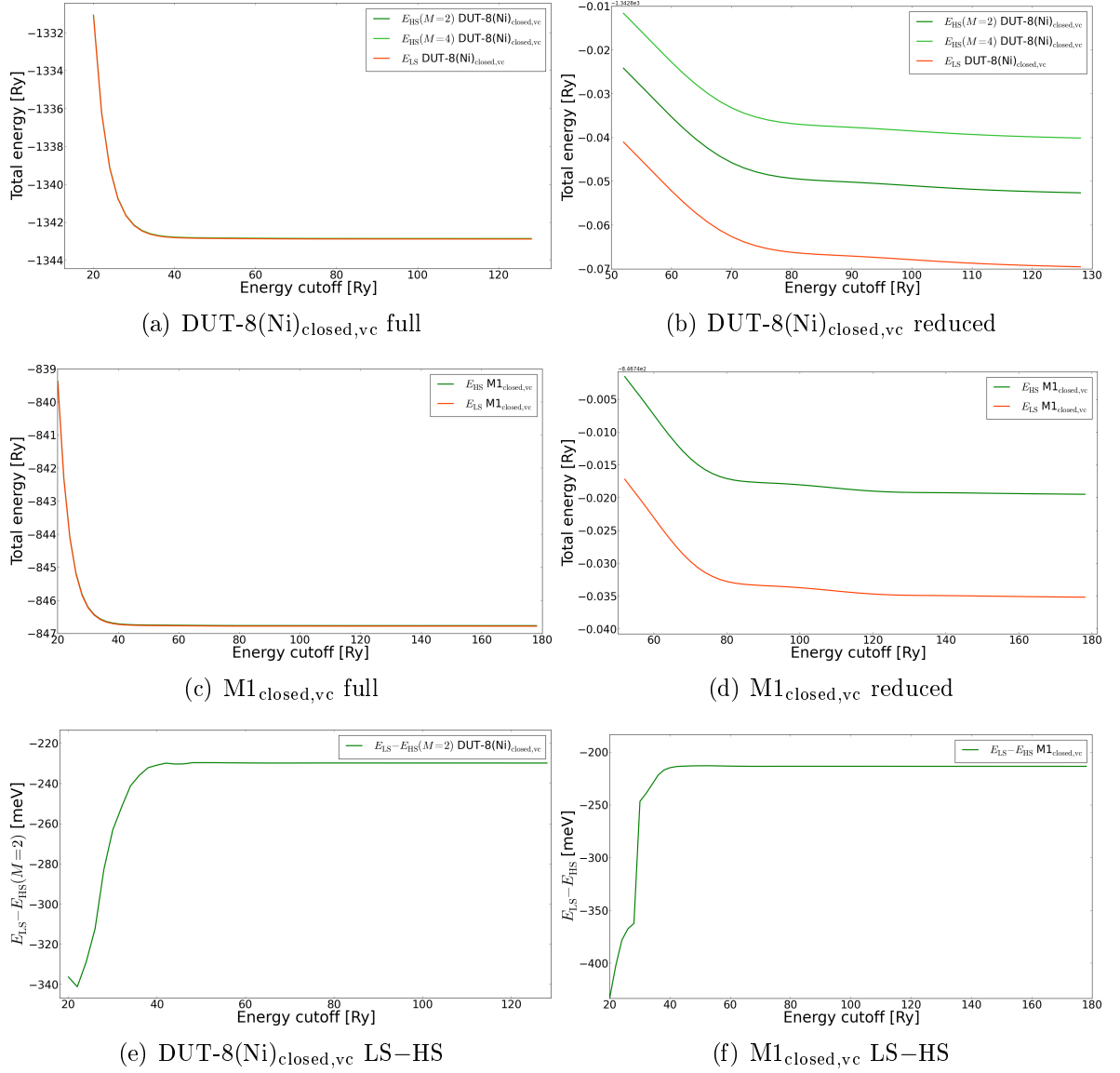


Figure 6.2.: Energies for high-spin and low-spin magnetic orders for DUT-8(Ni)_{closed,vc} and the corresponding M1 models for different kinetic energy cutoffs. Two different HS states are presented. The two last pictures show the energy difference $E_{LS} - E_{HS}$.

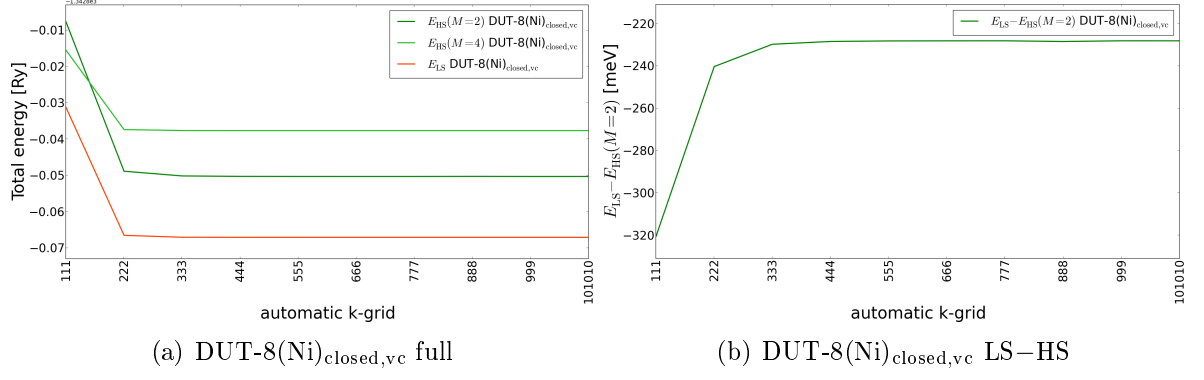


Figure 6.3.: Energies and $E_{\text{LS}} - E_{\text{HS}}$ for DUT-8(Ni)_{closed,vc} for different k-grids.

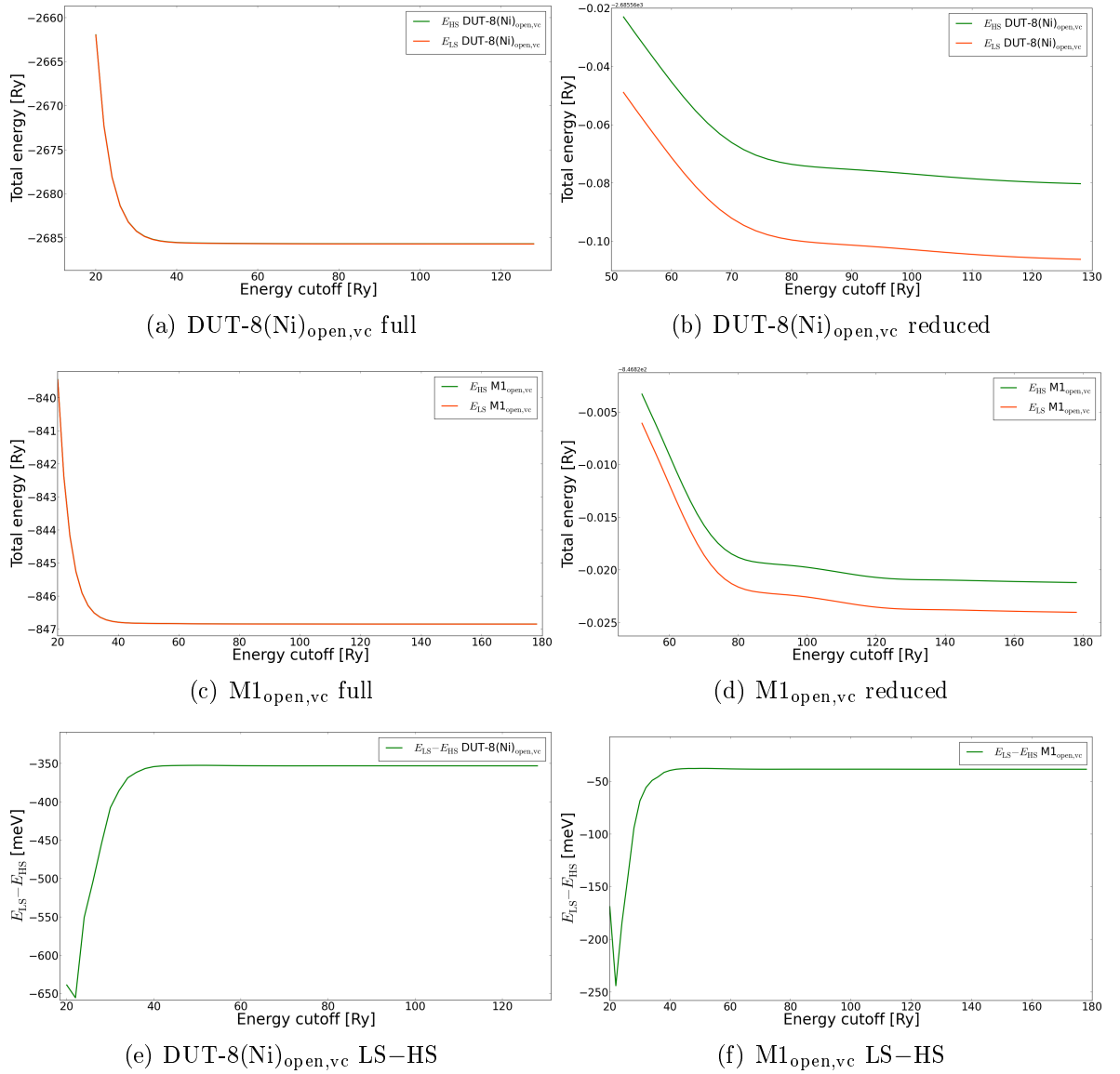


Figure 6.4.: Energies for high-spin and low-spin magnetic orders for DUT-8(Ni)_{open,vc} and the corresponding M1 models for different kinetic energy cutoffs. Two different HS states are presented. The two last pictures show the energy difference $E_{\text{LS}} - E_{\text{HS}}$.

APPENDIX 4

Table 6.2.: Ground state atomic energies and magnetizations as benchmarked with QE ($E_{\text{cutoff}} = 300$ Ry, $15 \times 15 \times 15$ Å cell). The pseudopotential for Ru did not describe the atomic energy at all, thus no convergence has been achieved.

Element	$E(\text{Element})$ [Ry]	M [μ_B]	Element	$E(\text{Element})$ [Ry]	M [μ_B]
H	-0.999981	1.00	Ni	-185.351926	2.00
He	-5.786087	0.00	Cu	-212.836844	1.00
Li	-14.929801	1.00	Zn	-243.753599	0.00
Be	-6.543937	0.00	Ga	-277.733052	1.00
B	-11.001874	1.00	Ge	-315.269244	2.00
C	-17.868525	2.00	As	-175.773163	3.00
N	-27.836842	3.00	Se	-189.132540	2.00
O	-41.295723	2.00	Br	-204.271642	1.00
F	-59.127830	1.00	Kr	-221.402799	0.00
Ne	-82.025630	0.00	Rb	-239.864241	1.00
Na	-109.172888	1.00	Sr	-260.130151	0.00
Mg	-33.506324	0.00	Y	-282.294747	1.00
Al	-39.250366	1.00	Zr	-306.758109	4.00
Si	-46.391802	2.00	Nb	-333.755509	5.00
P	-55.279324	3.00	Mo	-363.455156	6.00
S	-66.069166	2.00	Tc	-395.798755	5.00
Cl	-79.224102	1.00	Ru	—	—
Ar	-95.082428	0.00	Rh	-469.752025	3.00
K	-112.948573	1.00	Pd	-330.837746	0.00
Ca	-133.380692	0.00	Ag	-355.121477	1.00
Sc	-156.652229	1.00	Cd	-381.761911	0.00
Ti	-183.314893	4.00	In	-410.602387	1.00
V	-213.640042	5.00	Sn	-441.829919	2.00
Cr	-247.929876	6.00	Sb	-347.464633	3.00
Mn	-286.241561	5.00	Te	-512.032305	2.00
Fe	-328.912845	4.00	I	-378.815290	1.00
Co	-161.682460	3.00	Xe	-593.376828	0.00

Table 6.3.: Binding energies E_{bind} for several systems including all considered MOFs. Calculated with $E_{\text{bind}} = E_{\text{system}} - \sum_i n_i E_i$, where E_{system} is the total energy of the complete system and n_i is the number of atoms of species i with the energy E_i . The reduced binding energy $E_{\text{bind,red}}$ is the binding energy per atom, thus $E_{\text{bind,red}} = E_{\text{bind}}/N$, with N as the total number of atoms per system/cell.

System	sum formula	N	E_{bind} [Ry]	$E_{\text{bind,red}}$ [Ry]
DUT-8(Ni) _{open,init}	Ni ₄ N ₄ O ₁₆ C ₆₀ H ₄₈	132	-51.652001	-0.391309
DUT-8(Ni) _{closed,init}	Ni ₂ N ₂ O ₈ C ₃₀ H ₂₄	66	-25.265441	-0.382809
DUT-8(Ni) _{open,vc}	Ni ₄ N ₄ O ₁₆ C ₆₀ H ₄₈	132	-52.184054	-0.395334
DUT-8(Ni) _{open,vc,fix angles}	Ni ₄ N ₄ O ₁₆ C ₆₀ H ₄₈	132	-52.184059	-0.395334
DUT-8(Ni) _{closed,vc}	Ni ₂ N ₂ O ₈ C ₃₀ H ₂₄	66	-26.128431	-0.395885
M1 _{open,init}	Ni ₂ N ₂ O ₈ C ₄ H ₁₀	26	-8.612039	-0.331232
M1 _{closed,init}	Ni ₂ N ₂ O ₈ C ₄ H ₁₀	26	-8.184674	-0.314795
M1 _{open,vc}	Ni ₂ N ₂ O ₈ C ₄ H ₁₀	26	-8.686612	-0.334100
M1 _{closed,vc}	Ni ₂ N ₂ O ₈ C ₄ H ₁₀	26	-8.617741	-0.331456
UiO-66	Zr ₆ O ₃₂ C ₄₈ H ₂₈	114	-50.309947	-0.441315
UiO-67	Zr ₆ O ₃₂ C ₈₄ H ₅₂	174	-75.158274	-0.431944
Linker UiO-66	C ₈ O ₄ H ₆	18	-7.122742	-0.395708
Zr cluster	Zr ₆ O ₃₂ C ₁₂ H ₁₆	66	-27.102384	-0.410642

For the initial structures, DUT-8(Ni)_{open,init} is more stable than the respective DUT-8(Ni)_{closed,init} structure. However, as DUT-8(Ni)_{closed} is the one 'as made' and the one which stabilizes when no absorption occurs, one would expect an lower binding energy for DUT-8(Ni)_{closed}. Indeed, in our optimizations we find that DUT-8(Ni)_{closed,vc} is energetically more favourable by about 7.5 meV/atom.

APPENDIX 5

Table 6.4.: Results for supercell calculations for the DUT-8(Ni)_{open,init} and the DUT-8(Ni)_{closed,init} structure featuring different magnetic orderings. The magnetic dimer units **I**, **II**, **III** and **IV** are indicated in figure 3.2. \uparrow and \downarrow count for the Ni at the magnetic dimer unit. Furthermore, M_{tot} is the total magnetization, M_{abs} the absolute magnetization, **low** stand for a low-spin ordering and **high** for a high-spin ordering. The energy difference $\Delta E_{\text{LS}(\text{local})} = E_{\text{tot}} - E_{\text{LS}(\text{local})}$ is used to compare different magnetic ordering.

global	type	I	II	III	IV	M_{tot} [μ_{B} /cell]	M_{abs} [μ_{B} /cell]	$\Delta E_{\text{LS}(\text{local})}$ [meV/dimer]
DUT-8(Ni) _{open,init}								
low	I,II,III,IV _{low}	$\uparrow\downarrow$	$\uparrow\downarrow$	$\uparrow\downarrow$	$\uparrow\downarrow$	0.00	14.93	0.00
	I-IV _{high} II-III _{high}	$\uparrow\uparrow$	$\downarrow\downarrow$	$\downarrow\downarrow$	$\uparrow\uparrow$	0.00	16.38	190.349
	I-II _{high} III-IV _{high}	$\uparrow\uparrow$	$\uparrow\uparrow$	$\downarrow\downarrow$	$\downarrow\downarrow$	0.00	16.35	190.369
high, $S = 4$	I,II,III,IV _{high}	$\uparrow\uparrow$	$\uparrow\uparrow$	$\uparrow\uparrow$	$\uparrow\uparrow$	n/a	n/a	n/a
high, $S = 8$	I,II,III,IV _{high}	$\uparrow\uparrow$	$\uparrow\uparrow$	$\uparrow\uparrow$	$\uparrow\uparrow$	16.00	16.52	198.927
DUT-8(Ni) _{closed}								
low	I,II,III,IV _{low}	$\uparrow\downarrow$	$\uparrow\downarrow$	$\uparrow\downarrow$	$\uparrow\downarrow$	0.00	14.80	0.00
	I-IV _{high} II-III _{high}	$\uparrow\uparrow$	$\downarrow\downarrow$	$\downarrow\downarrow$	$\uparrow\uparrow$	0.00	16.63	80.747
	I-II _{high} III-IV _{high}	$\uparrow\uparrow$	$\uparrow\uparrow$	$\downarrow\downarrow$	$\downarrow\downarrow$	0.00	16.36	58.086
	I-III _{high} II-IV _{high}	$\uparrow\uparrow$	$\downarrow\downarrow$	$\uparrow\uparrow$	$\downarrow\downarrow$	0.00	16.34	58.058
high, $S = 4$	I,II,IV _{high} III-all _{low}	$\downarrow\downarrow$	$\downarrow\downarrow$	$\uparrow\uparrow$	$\downarrow\downarrow$	8.00	16.49	69.411
	II,III,IV _{high} I-all _{low}	$\uparrow\uparrow$	$\downarrow\downarrow$	$\downarrow\downarrow$	$\downarrow\downarrow$	8.00	16.49	69.411
	I,II,III,IV _{high}	$\uparrow\uparrow$	$\uparrow\uparrow$	$\uparrow\uparrow$	$\uparrow\uparrow$	8.00	11.71	307.799
high, $S = 8$	I,II,III,IV _{high}	$\uparrow\uparrow$	$\uparrow\uparrow$	$\uparrow\uparrow$	$\uparrow\uparrow$	16.00	16.62	80.709

APPENDIX 6

Table 6.5.: Results of spin polarized calculations, leading to high-spin and low-spin ordering energies, for the DUT-8(Ni)_{open,init} models with calculated coupling constant J (QE).

Parameter	M1		M2	
	high-spin	low-spin	high-spin	low-spin
E_{tot} [Ry]	-846.754375	-846.769263	-1308.080997	-1308.094936
M_{tot} [μ_{B} /cell]	4.00	0.00	4.00	0.00
M_{abs} [μ_{B} /cell]	4.12	3.75	4.13	3.78
\mathbf{J} [cm^{-1}]	-272.2 (low-spin)		-254.8 (low-spin)	

	M3		M4	
	high-spin	low-spin	high-spin	low-spin
E_{tot} [Ry]	-814.889521	-814.873781	-814.889708	-814.873781
M_{tot} [μ_{B} /cell]	2.00	0.00	2.00	0.00
M_{abs} [μ_{B} /cell]	2.24	3.78	2.24	3.79
\mathbf{J} [cm^{-1}]	383.6 (high-spin (S=1))		388.2 (high-spin (S=1))	

	M5		M6	
	high-spin	low-spin	high-spin	low-spin
E_{tot} [Ry]	-783.002321	-782.972697	-874.137174	-874.143955
M_{tot} [μ_{B} /cell]	2.00	0.00	3.00	1.00
M_{abs} [μ_{B} /cell]	2.28	3.96	3.16	2.66
\mathbf{J} [cm^{-1}]	722.1 (high-spin (S=1))		-247.9 (low-spin)	

	M7		M8	
	high-spin	low-spin	high-spin	low-spin
E_{tot} [Ry]	-874.137337	-874.143971	-901.496196	-901.505635
M_{tot} [μ_{B} /cell]	3.00	1.00	2.00	0.00
M_{abs} [μ_{B} /cell]	3.16	2.67	2.17	1.84
\mathbf{J} [cm^{-1}]	-242.5 (low-spin)		-517.6 (low-spin)	

	M9		M10	
	high-spin	low-spin	high-spin	low-spin
E_{tot} [Ry]	-871.157189	-871.152198	-986.589603	-986.567429
M_{tot} [μ_{B} /cell]	2.00	0.00	2.00	0.00
M_{abs} [μ_{B} /cell]	2.32	3.74	2.32	3.73
\mathbf{J} [cm^{-1}]	121.7 (high-spin (S=1))		540.5 (high-spin (S=1))	

	M11		M12	
	high-spin	low-spin	high-spin	low-spin
E_{tot} [Ry]	-878.129988	-878.104523	-785.183492	-785.171607
M_{tot} [μ_{B} /cell]	2.00	0.00	2.00	0.00
M_{abs} [μ_{B} /cell]	2.16	4.06	2.19	1.91
\mathbf{J} [cm^{-1}]	620.7 (high-spin (S=1))		651.8 (high-spin (S=1))	

Table 6.6.: Results of spin polarized calculations, leading to high-spin and low-spin ordering energies, for the DUT-8(Ni)_{open,init} models with calculated coupling constant J (FPLO).

Parameter	M1		M2	
	high-spin	low-spin	high-spin	low-spin
E_{tot} [Ha]	-3911.497240	-3911.504756	-4835.233889	-4835.240945
M_{tot} [μ_B]	4.00	0.00	4.00	0.00
M_{abs} [μ_B]	4.00	3.65	4.01	3.68
J [cm^{-1}]	-274.8 (low-spin)		-257.9 (low-spin)	
	M3		M4	
	high-spin	low-spin	high-spin	low-spin
E_{tot} [Ha]	-3854.921547	-3854.911562	-3854.921631	-3854.911328
M_{tot} [μ_B]	2.00	0.00	2.00	0.00
M_{abs} [μ_B]	2.17	3.54	2.16	3.55
J [cm^{-1}]	486.7 (high-spin (S=1))		502.2 (high-spin (S=1))	
	M5		M6	
	high-spin	low-spin	high-spin	low-spin
E_{tot} [Ha]	-3798.334966	-3798.313407	-4045.694721	-4045.698052
M_{tot} [μ_B]	2.00	0.00	3.00	1.00
M_{abs} [μ_B]	2.12	3.80	3.00	2.59
J [cm^{-1}]	1050.9 (high-spin (S=1))		-243.6 (low-spin)	
	M7		M8	
	high-spin	low-spin	high-spin	low-spin
E_{tot} [Ha]	-4045.694775	-4045.698026	-4179.880396	-4179.884922
M_{tot} [μ_B]	3.00	1.00	2.00	0.00
M_{abs} [μ_B]	3.00	2.59	2.05	1.70
J [cm^{-1}]	-237.7 (low-spin)		-496.4 (low-spin)	
	M9		M10	
	high-spin	low-spin	high-spin	low-spin
E_{tot} [Ha]	-3951.245838	-3951.242622	-4175.555403	-4175.542651
M_{tot} [μ_B]	2.00	0.00	2.00	0.00
M_{abs} [μ_B]	2.17	3.64	2.15	3.61
J [cm^{-1}]	156.8 (high-spin (S=1))		621.6 (high-spin (S=1))	
	M11		M12	
	high-spin	low-spin	high-spin	low-spin
E_{tot} [Ha]	-3984.948996	-3984.934758
M_{tot} [μ_B]	2.00	0.00		
M_{abs} [μ_B]	2.40	3.93		
J [cm^{-1}]	694.1 (high-spin (S=1))		...	

Table 6.7.: Results of spin polarized calculations, leading to high-spin and low-spin ordering energies, for the DUT-8(Ni)_{closed,init} models with calculated coupling constant J (QE).

Parameter	M1		M2	
	high-spin	low-spin	high-spin	low-spin
E_{tot} [Ry]	-846.338057	-846.341899	-1307.584689	-1307.587911
M_{tot} [μ_{B} /cell]	4.00	0.00	4.00	0.00
M_{abs} [μ_{B} /cell]	4.17	3.64	4.20	3.71
J [cm^{-1}]	-70.2 (low-spin)		-58.9 (low-spin)	

	M3		M4	
	high-spin	low-spin	high-spin	low-spin
E_{tot} [Ry]	-814.497587	-814.486547	-814.488818	-814.489133
M_{tot} [μ_{B} /cell]	2.00	0.00	4.00	0.00
M_{abs} [μ_{B} /cell]	2.84	3.65	4.18	3.58
J [cm^{-1}]	269.1 (high-spin (S=1))		-5.7 (low-spin)	

	M5		M6	
	high-spin	low-spin	high-spin	low-spin
E_{tot} [Ry]	-782.637608	-782.623384	-873.705448	-873.705398
M_{tot} [μ_{B} /cell]	2.00	0.00	3.00	1.00
M_{abs} [μ_{B} /cell]	3.06	3.71	3.17	2.66
J [cm^{-1}]	346.7 (high-spin (S=1))		1.8 (high-spin (S=1.5))	

	M7		M8	
	high-spin	low-spin	high-spin	low-spin
E_{tot} [Ry]	-873.719088	-873.721949	-901.072541	-901.073809
M_{tot} [μ_{B} /cell]	3.00	1.00	2.00	0.00
M_{abs} [μ_{B} /cell]	3.17	2.54	2.16	1.64
J [cm^{-1}]	-104.6 (low-spin)		-69.5 (low-spin)	

	M9		M10	
	high-spin	low-spin	high-spin	low-spin
E_{tot} [Ry]	-870.747059	-870.745486	-986.178308	-986.162758
M_{tot} [μ_{B} /cell]	2.00	0.00	2.00	0.00
M_{abs} [μ_{B} /cell]	2.93	3.49	3.06	3.38
J [cm^{-1}]	38.3 (high-spin (S=1))		379.0 (high-spin (S=1))	

	M11		M12	
	high-spin	low-spin	high-spin	low-spin
E_{tot} [Ry]	-877.734942	-877.717131	-784.827747	-784.827098
M_{tot} [μ_{B} /cell]	2.00	0.00	2.00	0.00
M_{abs} [μ_{B} /cell]	3.42	3.59	2.44	2.19
J [cm^{-1}]	434.1 (high-spin (S=1))		35.6 (high-spin (S=1))	

Table 6.8.: Results of spin polarized calculations, leading to high-spin and low-spin ordering energies, for the DUT-8(Ni)_{closed,init} models with calculated coupling constant J (FPLO).

Parameter	M1		M2	
	high-spin	low-spin	high-spin	low-spin
E_{tot} [Ha]	-3911.280552	-3911.282156	-4834.975649	-4834.976900
M_{tot} [μB]	4.00	0.00	4.00	0.00
M_{abs} [μB]	4.05	3.43	4.07	3.53
J [cm^{-1}]	-58.6 (low-spin)		-45.7 (low-spin)	
	M3		M4	
	high-spin	low-spin	high-spin	low-spin
E_{tot} [Ha]	-3854.718415	-3854.712473	-3854.714055	-3854.713763
M_{tot} [μB]	2.00	0.00	4.00	0.00
M_{abs} [μB]	2.59	3.47	4.04	3.45
J [cm^{-1}]	289.7 (high-spin (S=1))		10.7 (high-spin (S=2))	
	M5		M6	
	high-spin	low-spin	high-spin	low-spin
E_{tot} [Ha]	-3798.146386	-3798.138824	-4045.472902	-4045.472974
M_{tot} [μB]	2.00	0.00	3.00	1.00
M_{abs} [μB]	2.99	3.57	3.08	2.49
J [cm^{-1}]	368.6 (high-spin (S=1))		-5.3 (low-spin)	
	M7		M8	
	high-spin	low-spin	high-spin	low-spin
E_{tot} [Ha]	-4045.479955	-4045.481348	-4179.665269	-4179.666028
M_{tot} [μB]	3.00	1.00	2.00	0.00
M_{abs} [μB]	3.06	2.41	2.09	1.57
J [cm^{-1}]	-101.9 (low-spin)		-37.5 (low-spin)	
	M9		M10	
	high-spin	low-spin	high-spin	low-spin
E_{tot} [Ha]	-3951.032552	-3951.030612	-4175.343129	-4175.333708
M_{tot} [μB]	2.00	0.00	2.00	0.00
M_{abs} [μB]	2.85	3.35	2.97	3.01
J [cm^{-1}]	94.6 (high-spin (S=1))		459.3 (high-spin (S=1))	
	M11		M12	
	high-spin	low-spin	high-spin	low-spin
E_{tot} [Ha]	-3984.744804	-3984.735262	-3799.239752	-3799.239346
M_{tot} [μB]	2.00	0.00	2.00	0.00
M_{abs} [μB]	3.32	3.39	2.37	2.08
J [cm^{-1}]	465.2 (high-spin (S=1))		44.7 (high-spin (S=1))	

Table 6.9.: Results of spin polarized calculations, leading to high-spin and low-spin ordering energies, for the DUT-8(Ni)_{open,vc} models with calculated coupling constant J (QE).

Parameter	M1		M2	
	high-spin	low-spin	high-spin	low-spin
E_{tot} [Ry]	-846.841011	-846.843836	-1308.253423	-1308.258418
M_{tot} [μ_{B} /cell]	2.00	0.00	2.00	0.00
M_{abs} [μ_{B} /cell]	2.28	3.21	2.24	3.23
J [cm^{-1}]	-68.8 (low-spin)		-121.7 (low-spin)	
	M3		M4	
	high-spin	low-spin	high-spin	low-spin
E_{tot} [Ry]	-814.996581	-814.957662	-814.997193	-814.958017
M_{tot} [μ_{B} /cell]	2.00	0.00	2.00	0.00
M_{abs} [μ_{B} /cell]	2.23	3.04	2.22	3.06
J [cm^{-1}]	948.6 (high-spin (S=1))		954.9 (high-spin (S=1))	
	M5		M6	
	high-spin	low-spin	high-spin	low-spin
E_{tot} [Ry]	-783.129353	-783.104115	-874.132832	-874.139524
M_{tot} [μ_{B} /cell]	2.00	0.00	3.00	1.00
M_{abs} [μ_{B} /cell]	2.23	1.19	3.19	2.35
J [cm^{-1}]	1384.1 (high-spin (S=1))		-244.7 (low-spin)	
	M7		M8	
	high-spin	low-spin	high-spin	low-spin
E_{tot} [Ry]	-874.132780	-874.139331	-901.477265	-901.485022
M_{tot} [μ_{B} /cell]	3.00	1.00	2.00	0.00
M_{abs} [μ_{B} /cell]	3.19	2.36	2.18	1.92
J [cm^{-1}]	-239.5 (low-spin)		-425.4 (low-spin)	
	M9		M10	
	high-spin	low-spin	high-spin	low-spin
E_{tot} [Ry]	-871.275958	-871.248381	-986.711098	-
M_{tot} [μ_{B} /cell]	2.00	0.00	2.00	-
M_{abs} [μ_{B} /cell]	2.26	3.18	2.26	-
J [cm^{-1}]	672.2 (high-spin (S=1))		(high-spin (S=1))	
	M11		M12	
	high-spin	low-spin	high-spin	low-spin
E_{tot} [Ry]	-878.237231	-878.217699	-	-
M_{tot} [μ_{B} /cell]	2.00	0.00	-	-
M_{abs} [μ_{B} /cell]	2.49	1.36	-	-
J [cm^{-1}]	1071.2 (high-spin (S=1))		-	

Table 6.10.: Results of spin polarized calculations, leading to high-spin and low-spin ordering energies, for the DUT-8(Ni)_{open,vc} models with calculated coupling constant J (FPLO).

Parameter		M1		M2	
		high-spin	low-spin	high-spin	low-spin
E_{tot}	[Ry]	-3911.507314	-3911.508554	-4835.248980	-4835.251896
M_{tot}	$[\mu_{\text{B}}/\text{cell}]$	2.00	0.00	2.00	0.00
M_{abs}	$[\mu_{\text{B}}/\text{cell}]$	2.06	3.11	2.05	3.13
\mathbf{J}	$[\text{cm}^{-1}]$	-60.5 (low-spin)		-142.2 (low-spin)	
		M3		M4	
		high-spin	low-spin	high-spin	low-spin
E_{tot}	[Ry]	-3854.946938	-3854.927745	-3854.947252	-3854.928339
M_{tot}	$[\mu_{\text{B}}/\text{cell}]$	2.00	0.00	2.00	0.00
M_{abs}	$[\mu_{\text{B}}/\text{cell}]$	2.06	2.48	2.06	2.65
\mathbf{J}	$[\text{cm}^{-1}]$	936.0 (high-spin (S=1))		922.3 (high-spin (S=1))	
		M5		M6	
		high-spin	low-spin	high-spin	low-spin
E_{tot}	[Ry]	-3798.375608	-3798.369013	-4045.691194	-4045.694477
M_{tot}	$[\mu_{\text{B}}/\text{cell}]$	2.00	0.00	3.00	1.00
M_{abs}	$[\mu_{\text{B}}/\text{cell}]$	2.07	0.24	3.00	2.28
\mathbf{J}	$[\text{cm}^{-1}]$	723.6 (high-spin (S=1))		-240.1 (low-spin)	
		M7		M8	
		high-spin	low-spin	high-spin	low-spin
E_{tot}	[Ha]	-4045.691197	-4045.694441	-4179.869896	-4179.867505
M_{tot}	$[\mu_{\text{B}}/\text{cell}]$	3.00	1.00	2.00	0.00
M_{abs}	$[\mu_{\text{B}}/\text{cell}]$	3.00	2.28	2.04	0.00
\mathbf{J}	$[\text{cm}^{-1}]$	-235.0 (low-spin)		— (low-spin)	
		M9		M10	
		high-spin	low-spin	high-spin	low-spin
E_{tot}	[Ha]	-3951.275102	-3951.260966	-4175.587403	—
M_{tot}	$[\mu_{\text{B}}/\text{cell}]$	2.00	0.00	2.00	0.00
M_{abs}	$[\mu_{\text{B}}/\text{cell}]$	2.06	3.07	2.07	3.73
\mathbf{J}	$[\text{cm}^{-1}]$	689.4 (high-spin (S=1))		(high-spin (S=1))	
		M11		M12	
		high-spin	low-spin	high-spin	low-spin
E_{tot}	[Ha]	—	—	—	—
M_{tot}	$[\mu_{\text{B}}/\text{cell}]$	—	—	—	—
M_{abs}	$[\mu_{\text{B}}/\text{cell}]$	—	—	—	—
\mathbf{J}	$[\text{cm}^{-1}]$	(high-spin (S=1))		—	

Table 6.11.: Results of spin polarized calculations, leading to high-spin and low-spin ordering energies, for the DUT-8(Ni)_{closed,vc} models with calculated coupling constant J (QE).

Parameter	M1		M2	
	high-spin	low-spin	high-spin	low-spin
E_{tot} [Ry]	-846.759283	-846.774966	-1308.170367	-1308.187779
M_{tot} [μ_B /cell]	2.00	0.00	2.00	0.00
M_{abs} [μ_B /cell]	2.18	3.36	2.17	3.37
\mathbf{J} [cm^{-1}]	-382.3 (low-spin)		-424.4 (low-spin)	
	M3		M4	
	high-spin	low-spin	high-spin	low-spin
E_{tot} [Ry]	-814.909156	-814.883658	-814.909931	-814.884868
M_{tot} [μ_B /cell]	2.00	0.00	2.00	0.00
M_{abs} [μ_B /cell]	2.27	3.18	2.28	3.22
\mathbf{J} [cm^{-1}]	621.5 (high-spin (S=1))		610.9 (high-spin (S=1))	
	M5		M6	
	high-spin	low-spin	high-spin	low-spin
E_{tot} [Ry]	-783.036494	-783.025939	-874.067430	-874.065699
M_{tot} [μ_B /cell]	2.00	0.00	3.00	1.00
M_{abs} [μ_B /cell]	2.29	1.24	3.18	2.58
\mathbf{J} [cm^{-1}]	578.9 (high-spin (S=1))		63.3 (high-spin (S=1.5))	
	M7		M8	
	high-spin	low-spin	high-spin	low-spin
E_{tot} [Ry]	-874.067319	-874.065637	-901.410898	-901.412677
M_{tot} [μ_B /cell]	3.00	1.00	2.00	0.00
M_{abs} [μ_B /cell]	3.18	2.55	2.16	1.97
\mathbf{J} [cm^{-1}]	61.5 (high-spin (S=1.5))		-97.6 (low-spin)	
	M9		M10	
	high-spin	low-spin	high-spin	low-spin
E_{tot} [Ry]	-871.195973	-871.189322	-986.619073	-986.590590
M_{tot} [μ_B /cell]	2.00	0.00	2.00	0.00
M_{abs} [μ_B /cell]	2.31	3.35	2.32	3.06
\mathbf{J} [cm^{-1}]	162.1 (high-spin (S=1))		694.2 (high-spin (S=1))	
	M11		M12	
	high-spin	low-spin	high-spin	low-spin
E_{tot} [Ry]	----	----	----	----
M_{tot} [μ_B /cell]	---	---	---	---
M_{abs} [μ_B /cell]	---	---	---	---
\mathbf{J} [cm^{-1}]	(high-spin (S=1))		---	

Table 6.12.: Results of spin polarized calculations, leading to high-spin and low-spin ordering energies, for the DUT-8(Ni)_{closed,vc} models with calculated coupling constant J (FPLO).

Parameter	M1		M2	
	high-spin	low-spin	high-spin	low-spin
E_{tot} [Ha]	-3911.464998	-3911.472467	-4835.182259	-4835.190753
M_{tot} [μ_{B} /cell]	2.00	0.00	2.00	0.00
M_{abs} [μ_{B} /cell]	2.08	3.24	2.01	3.24
\mathbf{J} [cm^{-1}]	-364.1 (low-spin)		-414.2 (low-spin)	
	M3		M4	
	high-spin	low-spin	high-spin	low-spin
E_{tot} [Ha]	-3854.901865	-3854.888882	-3854.902218	-3854.889478
M_{tot} [μ_{B} /cell]	2.00	0.00	2.00	0.00
M_{abs} [μ_{B} /cell]	2.07	2.99	2.09	3.03
\mathbf{J} [cm^{-1}]	632.9 (high-spin (S=1))		621.3 (high-spin (S=1))	
	M5		M6	
	high-spin	low-spin	high-spin	low-spin
E_{tot} [Ha]	-3798.327675	-3798.322455	-4045.656827	-4045.656006
M_{tot} [μ_{B} /cell]	2.00	0.00	3.00	1.00
M_{abs} [μ_{B} /cell]	2.08	0.24	3.00	2.44
\mathbf{J} [cm^{-1}]	572.5 (high-spin (S=1))		60.0 (high-spin (S=1.5))	
	M7		M8	
	high-spin	low-spin	high-spin	low-spin
E_{tot} [Ha]	-4045.656874	-4045.656031	-4179.834879	-4179.835696
M_{tot} [μ_{B} /cell]	3.00	1.00	2.00	0.00
M_{abs} [μ_{B} /cell]	3.00	2.46	2.04	1.81
\mathbf{J} [cm^{-1}]	61.6 (high-spin (S=1.5))		-89.6 (low-spin)	
	M9		M10	
	high-spin	low-spin	high-spin	low-spin
E_{tot} [Ha]	-3951.234022	-3951.230025	-4175.539816	-
M_{tot} [μ_{B} /cell]	2.00	0.00	2.00	0.00
M_{abs} [μ_{B} /cell]	2.07	3.22	2.08	3.06
\mathbf{J} [cm^{-1}]	194.8 (high-spin (S=1))		(high-spin (S=1))	
	M11		M12	
	high-spin	low-spin	high-spin	low-spin
E_{tot} [Ha]	-3984.927232	-	-	-
M_{tot} [μ_{B} /cell]	2.00	-	-	-
M_{abs} [μ_{B} /cell]	2.32	-	-	-
\mathbf{J} [cm^{-1}]	(high-spin (S=1))		-	

APPENDIX 7

Following the argumentation of M1 in section 3.5.1, a comparison between the resulting coupling constants J_{ij} for M1, M2 and the two SBU model as seen in section 3.5.3 has been carried out. This was done to determine the importance of the adjacent linkers. It seems that this is especially important for DUT-8(Ni)_{open,vc}, where the spin densities strongly interact with each other due to the very small Ni-Ni distance.

Thus, one can compare the coupling constants as obtained in the crystal structure (as a reference) with the J_{ij} for M1, M2 (adjacent carbon rings) and the two SBU model (adjacent dabco unit). By comparing the absolute differences in J_{ij} as well as the ratio of the J_{ij} s, a deeper insight into the distribution of the spin densities can be obtained. For this purpose, the following quantities are defined

$$\begin{aligned}\Delta J &= |J_{\text{crystal}} - J_{\text{M1}}| \\ \xi_{\text{M1-crystal}} &= \frac{J_{\text{M1}}}{J_{\text{crystal}}} \\ \xi_{\text{M1-M2}} &= \frac{J_{\text{M1}}}{J_{\text{M2}}} \\ \xi_{\text{M1-twoSBU}} &= \frac{J_{\text{M1}}}{J_{\text{two SBU}}},\end{aligned}$$

where the first one determines the absolute difference between the M1 model and the crystalline calculation considering J_{ij} (should preferably be close to zero cm^{-1}), the second gives an insight into the relative difference between M1 and crystal value (preferably close to 1) and the other two give an insight into how much the spin densities spread to the different linkers (preferably close to 1 as well).

These quantities have been determined for all considered systems (DUT-8(Ni)_{open,init}, DUT-8(Ni)_{closed,init}, DUT-8(Ni)_{open,vc}, DUT-8(Ni)_{closed,vc}) to fully understand where the model ansatz works well and where it starts to be not accurate anymore. More importantly, one can figure out why the ansatz might fail considering the distribution of the spin densities.

To determine the J_{ij} within a single SBU from the two SBU system (section 3.5.3), one needs two magnetic configurations, namely $\uparrow\uparrow$ -dabco- $\uparrow\uparrow$ and $\uparrow\downarrow$ -dabco- $\uparrow\downarrow$ (in accordance to the crystalline arrangement). Thus, the J_{ij} per SBU can be defined in analogy to equation (2.56), considering that $\Delta E' = (E_{\uparrow\downarrow\text{-dabco-}\uparrow\downarrow} - E_{\uparrow\uparrow\text{-dabco-}\uparrow\uparrow}) \cdot \frac{1}{2}$ and the total spins for HS and LS have to be divided by two to get the single SBU values, thus $S_{\text{HS/LS}} = \frac{1}{2}S_{\text{HS/LS,full}}$. The results are summarized in tables 6.13 and 6.14.

Table 6.13.: All coupling constant values for the evaluation of the given ratios.

System	J_{crystal} [cm^{-1}]	J_{M1} [cm^{-1}]	J_{M2} [cm^{-1}]	$J_{\text{two SBU}}$ [cm^{-1}]
DUT-8(Ni) _{open,init}	-267.4	-272.2	-254.8	-278.1
DUT-8(Ni) _{closed,init}	-108.4	-70.2	-58.9	-111.5
DUT-8(Ni) _{open,vc}	-316.1	-68.8	-121.7	-238.6
DUT-8(Ni) _{closed,vc}	-411.6	-382.3	-424.4	-423.7

Table 6.14.: Deeper analysis of the coupling constant in DUT-8(Ni). Different contributions show how much the magnetism is localized. If this is not the case and the J of M1 and the crystalline calculation differ, this investigation gives insight into where the spin densities will distribute.

System	ΔJ [cm^{-1}]	$\xi_{\text{M1-crystal}}$	$\xi_{\text{M1-M2}}$	$\xi_{\text{M1-twoSBU}}$
DUT-8(Ni) _{open,init}	4.8	1.018	1.068	0.979
DUT-8(Ni) _{closed,init}	38.2	0.648	1.192	0.972
DUT-8(Ni) _{open,vc}	247.3	0.218	0.565	0.288
DUT-8(Ni) _{closed,vc}	29.3	0.929	0.901	0.902

For DUT-8(Ni)_{open,init}, the magnetism is highly localized on the SBU and the spin densities do not distribute towards neither the carbon linker nor the dabco unit. This is clearly represented by $\Delta J \approx 0 \text{ cm}^{-1}$ and by all $\xi \approx 1$.

As mentioned in section 3.5.1, for DUT-8(Ni)_{closed,init} the trend looks a little different. There, the absolute value changes, giving rise to a significantly different ratio $\xi_{\text{M1-crystal}}$. This can be attributed to the lack of symmetry in the system, leading to a redistribution of the spin densities. The ratio is large due to the small value of J_{ij} in the first place. In comparison to the fully relaxed structure of DUT-8(Ni)_{closed}, a very similar absolute value in the change of J_{ij} has been found. Furthermore, the spin densities seem to have only spread onto the carbon linkers and not along the dabco unit (a comparison between $\xi_{\text{M1-twoSBU}}$ to DUT-8(Ni)_{open,init} shows that this quantity is essentially the same for both structures). Considering the length of the carbon linkers in the crystalline structure, there is a small coupling along such linkers. Therefore, even for this structure the magnetism is fairly localized. This investigation additionally shows that for DUT-8(Ni)_{closed,init}, even though it lacks symmetry and the J_{ij} for the crystal calculation and M1 differ quite strongly, further model calculation do not show any urgent necessity of the inclusion of the linkers in the description of J_{ij} .

Continuing with DUT-8(Ni)_{closed,vc}, one observes similar trends as for DUT-8(Ni)_{open,init}. The absolute change is larger, but due to the significantly larger J_{ij} in comparison to DUT-8(Ni)_{closed,init}, the initial ratio is still close to 1. Furthermore, the effect of the carbon linkers is negligible. Additionally, the influence of the dabco unit is the same as the one for the carbon linkers and thus negligible as well. With that, the M1 for this structure satisfactorily represents the magnetic properties of the crystalline structure.

At last, DUT-8(Ni)_{open,vc} shall be analyzed. Here, a significant absolute change in J_{ij} occurs. This is clearly reflected in the ratio between the J_{ij} of M1 and the crystalline value (about 5 times smaller). In contrast to DUT-8(Ni)_{closed,init}, the influences arise from the carbon linkers and even more from the dabco units. Thus, the spin densities are strongly distributed over the carbon linkers and the dabco unit, giving rise to strong effects on the coupling constant within the crystalline structure. This can be related to the very small Ni-Ni distance in the system, $d_{\text{Ni-Ni}} = 2.378 \text{ \AA}$. With that, this structure seems to be a limit for the applicability of the model system ansatz. Clearly, if the spin densities are strongly distributed on all sets of linkers, a model system where the linkers are cut off cannot accurately represent the magnetic properties of the crystalline structure. However, it should be noted that for all other systems, the ansatz works very well and is suitable for the description of the magnetic interaction between the Ni centers.

With that, the model system ansatz is verified and the strictly different values for DUT-8(Ni)_{open,vc} have been explained. This shall be discussed one step further. Combining the coupling constants for M2 and the two SBU model such as $J_{\text{all linkers}} = J_{\text{M2}} + J_{\text{twoSBU}}$ and comparing the resulting value with the crystalline one, a ratio of

$$\xi_{\text{open,vc}} = \frac{J_{\text{all linkers}}}{J_{\text{crystal}}} = 1.139.$$

is obtained. This value certainly represents the crystalline structure much better than the models systems individually. The final analysis is supposed to show that the model systems can reproduce the crystalline features. For too small Ni-Ni distances, more than one model is needed to investigate these features accurately. However, this extended model system ansatz gives reliable results and can be used as an verification of any model system.

APPENDIX 8

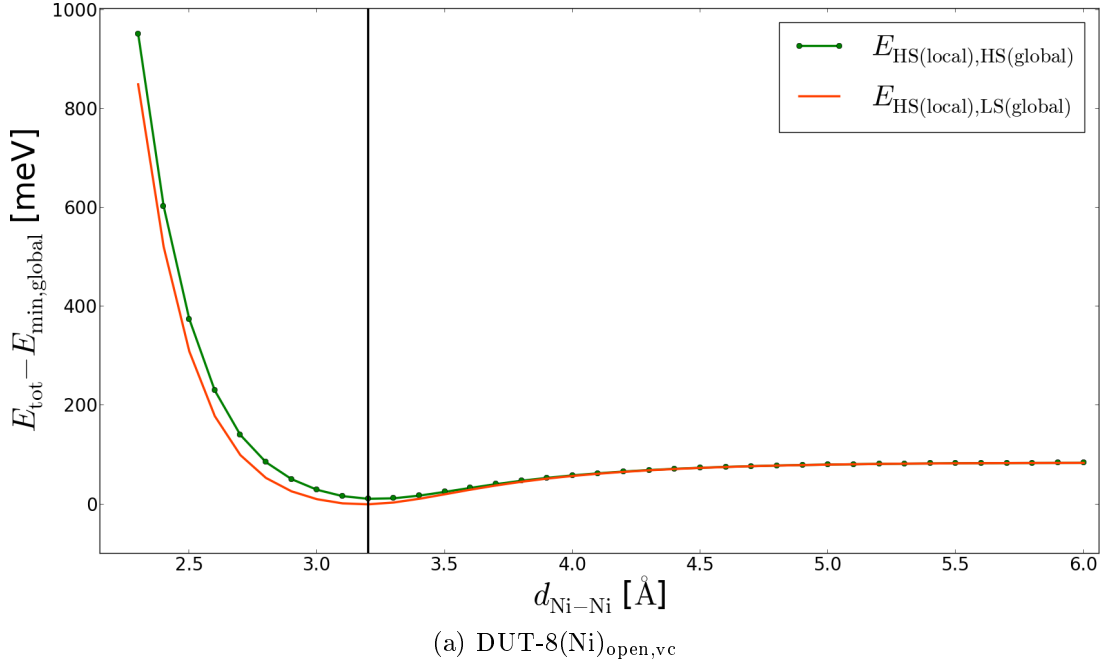


Figure 6.5.: Total energy difference of different magnetic ordering as a function of the Ni-Ni distance. For the model system derived from DUT-8(Ni)_{open,vc}. The global energy minimum is always obtained for a local HS coupling, independent of the coupling between the SBUs. The black line denotes the minimum distance.

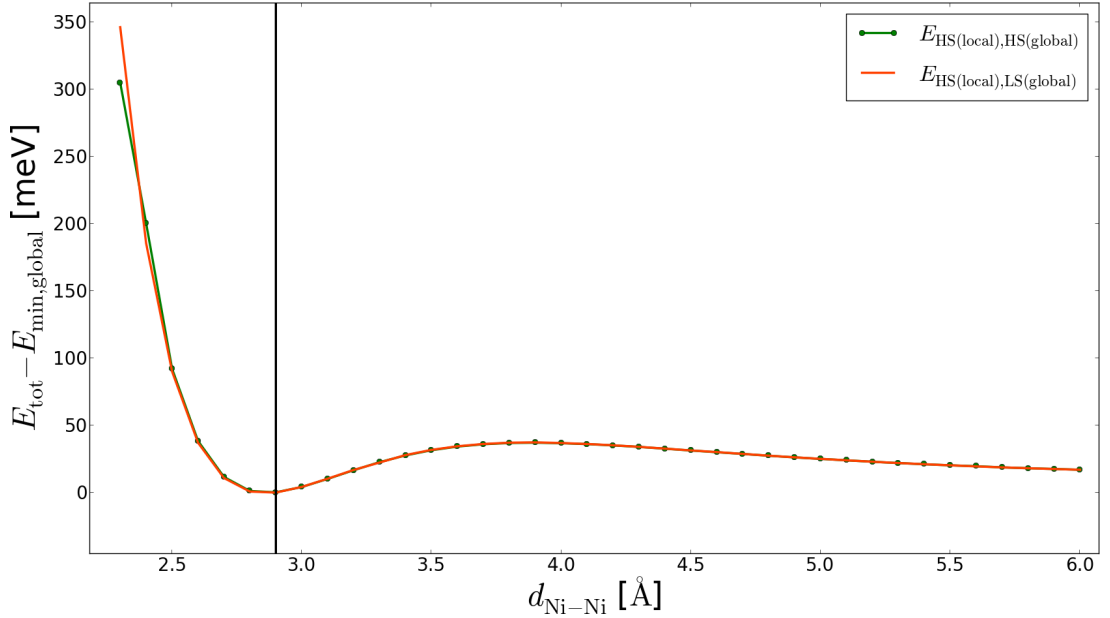


Figure 6.6.: Total energy difference of different magnetic ordering as a function of the Ni-Ni distance. For the model system derived from DUT-8(Ni)_{open,init}. To distinguish between the two local HS orderings, one line is solid while the other is displayed with dots. The black line denotes the minimum distance.

APPENDIX 9

Table 6.15.: Calculated energy differences and coupling constants for specific magnetic orders. In this case, J_{ij} can be evaluated e.g. like $J_{5.,6.} = (E_6. - E_5.) / (\langle \mathbf{S}_{\text{tot},5.}^2 \rangle)$, in analogy to equation (2.58). Models derived from DUT-8(Ni)_{open,init}. The system with FeCo shows a very different behavior. However, the calculations for the given model systems regarding the combination FeCo are computationally not very stable and should be viewed with caution.

System	ΔE_{QE} [meV]	ΔE_{FPLO} [meV]	J_{QE} [cm ⁻¹]	J_{FPLO} [cm ⁻¹]
NiNi $E_1. - E_2.$	-6.61	-6.75	—	—
FeFe $E_4. - E_3.$	-2.84	-3.54	-0.32	-0.39
FeCo $E_6. - E_5.$	-38.45	+25.60	-5.54	+3.69
FeCo $E_8. - E_7.$	—	—	—	—
FeCo $E_{10.} - E_9.$	+36.61	+6.91	+5.27	+0.99
FeNi $E_6. - E_5.$	-1.96	-0.49	-0.38	-0.09
FeNi $E_8. - E_7.$	-3.18	-1.69	-0.61	-0.32
FeNi $E_{10.} - E_9.$	-1.74	-0.38	-0.33	-0.07
FeCu $E_6. - E_5.$	+0.01	—	+0.003	—
FeCu $E_8. - E_7.$	-0.71	—	-0.19	—
FeCu $E_{10.} - E_9.$	-12.25	—	-3.29	—

Table 6.16.: Calculated energy differences for specific magnetic orders at certain arrangements of the magnetic atoms within the model (see section 3.5.3). Calculated with QE. Models derived from DUT-8(Ni)_{open,init}.

System	$E_{\text{XY-dabco-XY}}$ [Ry]	$E_{\text{XY-dabco-YX}}$ [Ry]	$E_{\text{YX-dabco-XY}}$ [Ry]	$\Delta E_{\text{geometries}}$ [meV]
FeCo	-2051.009159	-2051.011083	-2051.009096	+0.93
FeNi	-2098.333146	-2098.334922	-2098.329639	-0.87
FeCu	-2153.063004	-2153.055199	-2153.065612	-2.59

APPENDIX 10

For some geometries, the calculation of a specific magnetic ordering did not converged. In these cases, only the available value has been used. As already shown in table 3.9 in section 3.5.3, the energy differences between magnetic orderings of the same geometry are small. Thus, the displayed values should be valid.

Table 6.17.: All energies calculated with QE for the model system calculations as depicted in section 3.5.3. For model systems derived from DUT-8(Ni)_{closed,vc}.

System	E_{tot} [Ry]	E_{average} [Ry]	M_{tot} [μ_B]	M_{abs} [μ_B]
Ni \uparrow Ni \downarrow - Ni \downarrow Ni \uparrow	-1811.258288	-1811.258538	0.00	6.64
Ni \uparrow Ni \downarrow - Ni \uparrow Ni \downarrow	-1811.258788		0.00	6.62
Fe \uparrow Fe \uparrow - Fe \downarrow Fe \downarrow	-2385.578743	-2385.578637	0.00	16.64
Fe \uparrow Fe \uparrow - Fe \uparrow Fe \uparrow	-2385.578532		16.00	16.69
Fe \uparrow Co \uparrow - Fe \downarrow Co \downarrow	-2051.109481	-2051.109365	0.00	14.43
Fe \uparrow Co \uparrow - Fe \uparrow Co \uparrow	-2051.109249		14.00	14.45
Fe \uparrow Co \uparrow - Co \downarrow Fe \downarrow	-2051.111195	-2051.111032	0.00	14.42
Fe \uparrow Co \uparrow - Co \uparrow Fe \uparrow	-2051.110868		14.00	14.45
Co \uparrow Fe \uparrow - Fe \downarrow Co \downarrow	-2051.108752	-2051.108662	0.00	14.42
Co \uparrow Fe \uparrow - Fe \uparrow Co \uparrow	-2051.108572		14.00	14.42
Fe \uparrow Ni \uparrow - Fe \downarrow Ni \downarrow	-2098.457834	-2098.457712	0.00	12.45
Fe \uparrow Ni \uparrow - Fe \uparrow Ni \uparrow	-2098.457589		12.00	12.47
Fe \uparrow Ni \uparrow - Ni \downarrow Fe \downarrow	-2098.457265	-2098.457113	0.00	12.46
Fe \uparrow Ni \uparrow - Ni \uparrow Fe \uparrow	-2098.456962		12.00	12.48
Ni \uparrow Fe \uparrow - Fe \downarrow Ni \downarrow	-2098.454908	-2098.454815	0.00	12.45
Ni \uparrow Fe \uparrow - Fe \uparrow Ni \uparrow	-2098.454723		12.00	12.47
Fe \uparrow Cu \uparrow - Fe \downarrow Cu \downarrow	-2153.143931	-2153.143962	0.00	10.35
Fe \uparrow Cu \uparrow - Fe \uparrow Cu \uparrow	-2153.143995		10.00	10.35
Fe \uparrow Cu \uparrow - Cu \downarrow Fe \downarrow	-2153.140471	-2153.140394	0.00	10.36
Fe \uparrow Cu \uparrow - Cu \uparrow Fe \uparrow	-2153.140317		10.00	10.38
Cu \uparrow Fe \uparrow - Fe \downarrow Cu \downarrow	—	—	—	—
Cu \uparrow Fe \uparrow - Fe \uparrow Cu \uparrow	-2153.145650		10.00	10.36
Ni \uparrow Cu \uparrow - Ni \downarrow Cu \downarrow	-1865.955074	-1865.954956	0.00	6.33
Ni \uparrow Cu \uparrow - Ni \uparrow Cu \uparrow	-1865.954839		6.00	6.36
Ni \uparrow Cu \uparrow - Cu \downarrow Ni \downarrow	-1865.947300	-1865.947261	0.00	6.36
Ni \uparrow Cu \uparrow - Cu \uparrow Ni \uparrow	-1865.947222		6.00	6.37
Cu \uparrow Ni \uparrow - Ni \downarrow Cu \downarrow	-1865.962572	-1865.962280	0.00	6.30
Cu \uparrow Ni \uparrow - Ni \uparrow Cu \uparrow	-1865.961988		6.00	6.34

Table 6.18.: All energies calculated with FPLO for the model system calculations as depicted in section 3.5.3. For model systems derived from DUT-8(Ni)_{closed,vc}.

System	E_{tot} [Ha]	E_{average} [Ha]	M_{tot} [μ_B]	M_{abs} [μ_B]
Ni \uparrow Ni \downarrow - Ni \downarrow Ni \uparrow	-8055.030188	-8055.030317	0.00	6.39
Ni \uparrow Ni \downarrow - Ni \uparrow Ni \downarrow	-8055.030447		0.00	6.41
Fe \uparrow Fe \uparrow - Fe \downarrow Fe \downarrow	-7062.925357	—	0.00	15.98
Fe \uparrow Fe \uparrow - Fe \uparrow Fe \uparrow	—	—	—	—
Fe \uparrow Co \uparrow - Fe \downarrow Co \downarrow	-7304.255696	—	0.00	13.98
Fe \uparrow Co \uparrow - Fe \uparrow Co \uparrow	—	—	—	—
Fe \uparrow Co \uparrow - Co \downarrow Fe \downarrow	-7304.256445	-7304.256367	0.00	13.97
Fe \uparrow Co \uparrow - Co \uparrow Fe \uparrow	-7304.256288		14.00	14.00
Co \uparrow Fe \uparrow - Fe \downarrow Co \downarrow	-7304.255709	-7304.255675	0.00	14.00
Co \uparrow Fe \uparrow - Fe \uparrow Co \uparrow	-7304.255641		14.00	14.00
Fe \uparrow Ni \uparrow - Fe \downarrow Ni \downarrow	-7558.997512	-7558.997465	0.00	11.99
Fe \uparrow Ni \uparrow - Fe \uparrow Ni \uparrow	-7558.997419		12.00	12.00
Fe \uparrow Ni \uparrow - Ni \downarrow Fe \downarrow	-7558.996819	-7558.996760	0.00	11.99
Fe \uparrow Ni \uparrow - Ni \uparrow Fe \uparrow	-7558.996702		12.00	12.00
Ni \uparrow Fe \uparrow - Fe \downarrow Ni \downarrow	-7558.996515	-7558.996481	0.00	11.98
Ni \uparrow Fe \uparrow - Fe \uparrow Ni \uparrow	-7558.996448		12.00	12.00
Fe \uparrow Cu \uparrow - Fe \downarrow Cu \downarrow	-7827.353531	-7827.353495	0.09	9.99
Fe \uparrow Cu \uparrow - Fe \uparrow Cu \uparrow	-7827.353459		10.00	10.01
Fe \uparrow Cu \uparrow - Cu \downarrow Fe \downarrow	-7827.351362	-7827.351332	0.01	9.99
Fe \uparrow Cu \uparrow - Cu \uparrow Fe \uparrow	-7827.351303		10.00	10.01
Cu \uparrow Fe \uparrow - Fe \downarrow Cu \downarrow	-7827.354320	—	0.00	9.98
Cu \uparrow Fe \uparrow - Fe \uparrow Cu \uparrow	—	—	—	—
Ni \uparrow Cu \uparrow - Ni \downarrow Cu \downarrow	-8323.391002	-8323.390924	0.00	5.98
Ni \uparrow Cu \uparrow - Ni \uparrow Cu \uparrow	-8323.390847		6.00	6.01
Ni \uparrow Cu \uparrow - Cu \downarrow Ni \downarrow	-8323.387389	-8323.387363	0.00	5.98
Ni \uparrow Cu \uparrow - Cu \uparrow Ni \uparrow	-8323.387339		6.00	6.01
Cu \uparrow Ni \uparrow - Ni \downarrow Cu \downarrow	-8323.394463	-8323.394306	0.00	6.00
Cu \uparrow Ni \uparrow - Ni \uparrow Cu \uparrow	-8323.394149		6.00	6.01

APPENDIX 11

Table 6.19.: Results of relativistic Hartree-Fock-Slater calculations [72] for the determination of the $1/r$ behavior of σ for the respective orbitals of Xe. The occupation per orbital is additionally given.

Orbital	occupation	$1/r$
1s	2	58.18950
2s	2	13.64296
2p _{1/2}	2	13.64047
2p _{3/2}	4	12.53121
3s	2	4.89696
3p _{1/2}	2	4.81512
3p _{3/2}	4	4.54013
3d _{3/2}	4	4.40406
3d _{5/2}	6	4.33320
4s	2	1.99342
4p _{1/2}	2	1.88912
4p _{3/2}	4	1.79951
4d _{3/2}	4	1.56644
4d _{5/2}	6	1.54392
5s	2	0.73283
5p _{1/2}	2	0.61465
5p _{3/2}	4	0.57987

APPENDIX 12

As a first model system to gain an insight into the Xe-surface influence on the chemical shift, benzene was used, as it is the main component of the linkers in UiO-66 and UiO-67. Furthermore, the chemical shift behavior around benzene is well known [78]. For this purpose, the chemical shift in the volume around the molecule has been analyzed. This was done by placing one Xe atom at specific positions and evaluate its chemical shift. To do so, the Xe was moved along two paths. The first one starts above the middle of the molecule, at a Xe-C distance of 3.5 Å (according to the respective vdW radii ($r_{\text{vdW}}(\text{Xe}) = 2.16 \text{ \AA}$, $r_{\text{vdW}}(\text{C}) = 1.70 \text{ \AA}$). The minimum distance takes into account regions where the atoms get very close. The path ends above one of the H atoms (see figure 6.7). The Xe was moved in 0.1 Å steps along this path, while its height was shifted in 0.1 Å steps out of plane (z axis in figure 6.7) until $d_{\text{Xe-C}} = 5.5 \text{ \AA}$. The second path started again above the middle of the molecule, but ended in between two H atoms. The height was varied like in the first path. The total shift is given by $\delta_{\text{total}} = \sigma_{\text{ref}} - \frac{1}{3}\text{Tr}(\sigma_{ij})$.

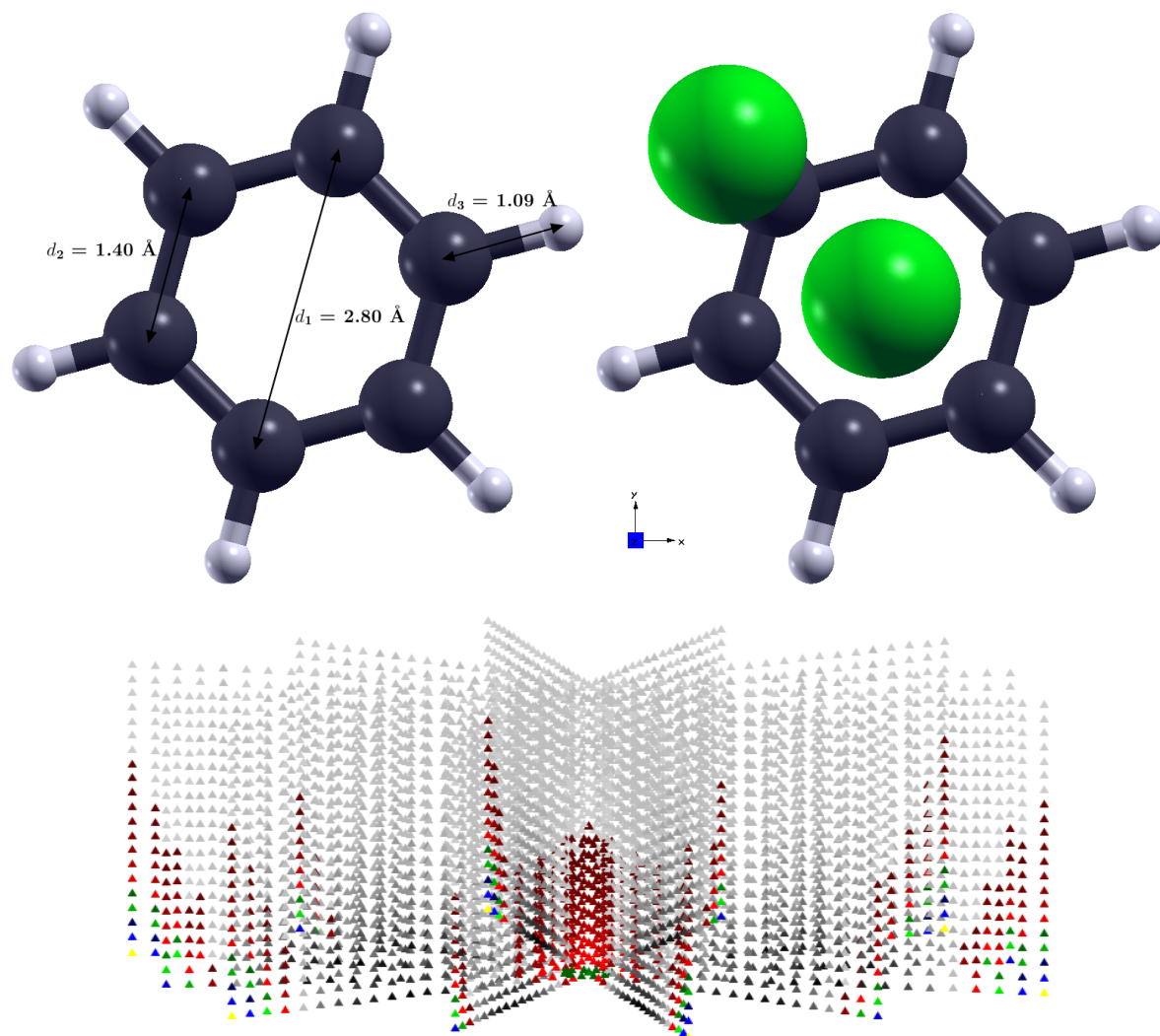


Figure 6.7.: The benzene model system to derive δ_S according to the influence of the molecule on the chemical shift of the Xe. On the left side, the distances within this model are drawn. On the right side, the initial and final position of the Xe atom (green) for the first path are given. The last figure shows the shift in the z direction, where colors indicate a deshielding region, while grey to black indicate a shielding region. A clear cone above the carbon ring can be seen, as known from the literature [78].

APPENDIX 13

Table 6.20.: Total energy differences for different positions of Xe in the pores ($T_{p,1}$, $T_{p,2}$ and O_p) for UiO-66 and UiO-67. The total energy at a specific position $E_{\text{Xe-site}}$ was subtracted by the global minimum for the respective MOF E_{min} , which refers to the energy of the MOF with Xe at its most favourable position. With that, the energy difference is given as $\Delta E = E_{\text{Xe-site}} - E_{\text{min}}$. The reference energies are $E_{\text{UiO-66}} \approx -4691.487979$ Ry and $E_{\text{UiO-67}} = -5383.602073$ Ry. The position 'to linker' describes a movement from the middle of the pore directly towards the linker while 'to pore' specifies a movement along the space diagonal, thus in between the SBU and the linker.

System	position	$\Delta E_{T_{p,1}}$ [meV]	$\Delta E_{T_{p,2}}$ [meV]	ΔE_{O_p} [meV]
UiO-66	middle	+73.19	+149.49	+205.07
	+1 Å to SBU	—	—	+180.46
	+2 Å to SBU	—	—	+83.56
	+2.5 Å to SBU	—	—	± 0.00
	+1 Å to linker	—	—	+181.51
	+2 Å to linker	—	—	+88.16
	+1 Å to pore	—	—	+183.04
	+2 Å to pore	—	—	+99.59
UiO-67	middle	+352.96	+404.11	+442.58
	+1 Å to SBU	+341.62	+396.75	+435.83
	+2 Å to SBU	+284.21	+352.34	+420.17
	+3 Å to SBU	+174.61	+273.47	+381.69
	+4 Å to SBU	± 0.0	+121.83	+317.41
	+5 Å to SBU	—	—	+194.79
	+1 Å to linker	+338.16	+392.85	+435.17
	+2 Å to linker	+266.25	+344.43	+416.85
	+3 Å to linker	—	+211.98	+382.27
	+4 Å to linker	—	—	+294.43
	+1 Å to pore	+343.64	+397.16	+433.31
	+2 Å to pore	+301.54	+366.11	+421.29
	+3 Å to pore	+244.84	+324.29	+392.99
	+4 Å to pore	—	—	+348.31
+5 Å to pore	—	—	+303.02	

APPENDIX 14

To evaluate the porosity within MOFs, one can use a hard sphere model, where the overlap of spheres has to be evaluated and consequently subtracted from the total volume of all spheres (atoms). The volume which is left can then be compared to the total volume of a unit cell, providing the porosity Φ as

$$\Phi = \frac{V_{\text{void}}}{V_{\text{total}}}, \quad (6.20)$$

with $V_{\text{void}} = V_{\text{total}} - V_{\text{occupied}}$ is the empty volume in the unit cell with a volume of V_{total} . Thus, one needs to evaluate the occupied volume, which is, as mentioned before, the sum of the volumes of all atoms $\sum V_{\text{atoms}}$ (approximated as hard spheres with their respective vdW radii) minus the overlap V_{overlap} , which can be calculated analytically following the derivation below. This simple approach gives very good results at essentially no computational cost (see table 6.21).

Table 6.21.: All relevant informations for the determination of the porosities of all considered MOFs based on the simple hard sphere approach. All volumes are given in \AA^3 and all porosities in % . The literature values for DUT-8(Ni) are taken from [26] and the ones for UiO-66/67 are taken from [80].

MOF	V_{total}	$\sum V_{\text{atoms}}$	V_{overlap}	V_{occupied}	V_{void}	Φ	Φ_{lit}
DUT-8(Ni) _{open,vc,orthogonal}	3149	1953	606	1347	1802	57	67
DUT-8(Ni) _{open,vc}	3151	1953	606	1346	1805	57	67
DUT-8(Ni) _{open,exp}	3190	1953	709	1244	1946	61	67
DUT-8(Ni) _{closed,vc}	604	976	303	673	-69	-11	0
DUT-8(Ni) _{closed,exp}	648	976	324	652	-4	-1	0
UiO-66	2308	1992	823	1169	1139	49	53
UiO-67	4972	2906	1308	1599	3374	68	68

Additionally, one can determine the inverse pore volume density with $\rho_{\text{pore}} = \frac{V_{\text{void/acc}}}{m_{\text{total}}}$, where the mass of the unit cell is m_{total} and the void or accessible volume is calculated for one unit cell (as was done in table 6.21 and 6.22). The results for this ansatz in comparison to the one in the end of this section can be found in table 6.24.

Furthermore, the pore dimensions can be evaluated from the given volumes. Considering that $V_{\text{O}_p} \approx 4V_{\text{T}_p}$, that the pore size can be approximated by a sphere which has the same volume as the respective pore and that there is one of each T_p and one O_p per primitive unit cell, the pore dimensions can be characterized as $d = 2r$ and $r = \sqrt[3]{\frac{3V_{\text{pore}}}{4\pi}}$. This leads to pore dimensions of $d_{\text{T,UiO-66}} = 7.13 \text{ \AA}$, $d_{\text{O,UiO-66}} = 11.32 \text{ \AA}$, $d_{\text{T,UiO-67}} = 10.24 \text{ \AA}$ and $d_{\text{O,UiO-67}} = 16.26 \text{ \AA}$, which is in good agreement with literature [29]. With that, the volumes of the pores are described accurately.

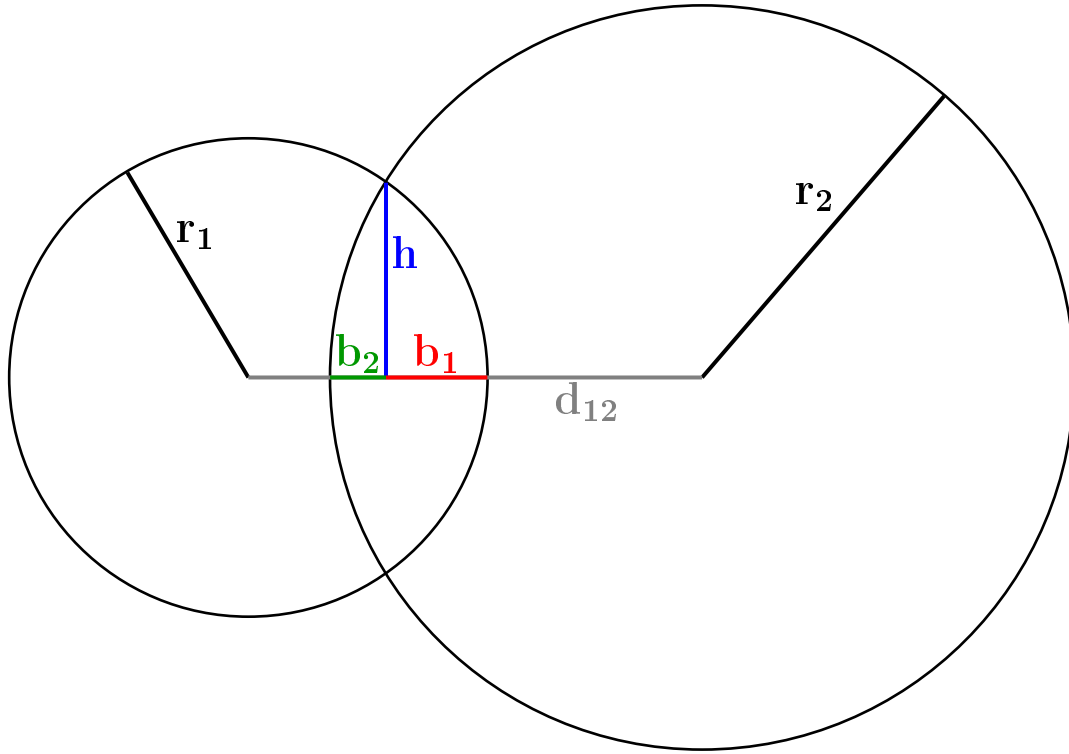


Figure 6.8.: Visualization of the overlap between two spheres. In the figure, $\mathbf{r}_{1,2}$ are the vdW radii of the atoms, \mathbf{d}_{12} is the distance between them, \mathbf{h} is the radius of the spherical caps (counts for both spheres), \mathbf{b}_1 and \mathbf{b}_2 are the heights of the spherical caps for sphere 1 and sphere 2, respectively.

To calculate h , b_1 and b_2 (see figure 6.8) the following equations are defined

$$\text{I: } b_1 + b_2 = r_1 + r_2 - d_{12}$$

$$\text{derived from } d_{12} = (d_{12} - r_2 + b_2) + (d_{12} - r_1 + b_1)$$

$$\text{II: } h^2 = r_2^2 - (d_{12} - r_1 + b_1)^2$$

$$\text{III: } h^2 = r_1^2 - (d_{12} - r_2 + b_2)^2$$

Putting I into II gives

$$h^2 = r_2^2 - (d_{12} - r_1 + b_1)^2$$

$$h^2 = r_2^2 - (d_{12} - r_1 + r_1 + r_2 - d_{12} - b_2)^2$$

$$h^2 = r_2^2 - r_2^2 + 2r_2b_2 - b_2^2$$

$$h = \sqrt{2r_2b_2 - b_2^2}, \quad (6.21)$$

while rearranging III leads to

$$\begin{aligned}
h^2 &= r_1^2 - (d_{12} - r_2 + b_2)^2 \\
h^2 &= r_1^2 - (d_{12} - r_2)^2 - 2(d_{12} - r_2)b_2 - b_2^2 \\
h &= \sqrt{r_1^2 - (d_{12} - r_2)^2 - 2(d_{12} - r_2)b_2 - b_2^2}.
\end{aligned} \tag{6.22}$$

Now b_2 can be obtained by (6.21) = (6.22)

$$\begin{aligned}
\sqrt{2r_2b_2 - b_2^2} &= \sqrt{r_1^2 - (d_{12} - r_2)^2 - 2(d_{12} - r_2)b_2 - b_2^2} \\
2r_2b_2 - b_2^2 &= r_1^2 - (d_{12} - r_2)^2 - 2(d_{12} - r_2)b_2 - b_2^2 \\
2d_{12}b_2 &= r_1^2 - (d_{12} - r_2)^2 = r_1^2 - d_{12}^2 + 2d_{12}r_2 - r_2^2 \\
b_2 &= \frac{r_1^2 - r_2^2 - d_{12}^2 + 2d_{12}r_2}{2d_{12}} = \frac{r_1^2 - (r_2 - d_{12})^2}{2d_{12}}.
\end{aligned} \tag{6.23}$$

This leads to b_1 by using I

$$\begin{aligned}
b_1 &= r_1 + r_2 - d_{12} - b_2 \\
b_1 &= r_1 + r_2 - d_{12} - \frac{r_1^2 - r_2^2 - d_{12}^2 + 2d_{12}r_2}{2d_{12}} \\
b_1 &= \frac{2d_{12}(r_1 + r_2 - d_{12}) - r_1^2 + r_2^2 + d_{12}^2 - 2d_{12}r_2}{2d_{12}} \\
b_1 &= \frac{2d_{12}r_1 + 2d_{12}r_2 - 2d_{12}^2 - r_1^2 + r_2^2 + d_{12}^2 - 2d_{12}r_2}{2d_{12}} \\
b_1 &= \frac{r_2^2 - (r_1 - d_{12})^2}{2d_{12}}.
\end{aligned} \tag{6.24}$$

As a last step, h can be gained by applying equation (6.23) to equation (6.21)

$$\begin{aligned}
h &= \sqrt{2r_2b_2 - b_2^2} \\
h &= \sqrt{2r_2 \frac{r_1^2 - (r_2 - d_{12})^2}{2d_{12}} - \left(\frac{r_1^2 - (r_2 - d_{12})^2}{2d_{12}} \right)^2} \\
h &= \sqrt{2r_2 \frac{r_1^2 - r_2^2 - d_{12}^2 + 2r_2d_{12}}{2d_{12}} - \underbrace{\left(\frac{r_1^4 - 2r_1^2(r_2 - d_{12})^2 + (r_2 - d_{12})^4}{4d_{12}^2} \right)}_{A/(4d_{12}^2)}} \\
h &= \sqrt{\frac{4r_1^2r_2d_{12} - 4r_2^3d_{12} - 4r_2d_{12}^3 + 8r_2^2d_{12}^2}{4d_{12}^2} - \left(\frac{A}{4d_{12}^2} \right)} \\
A &= r_1^4 - 2r_1^2r_2^2 + 4r_1^2r_2d_{12} - 2r_1^2d_{12}^2 + r_2^4 - 4r_2^3d_{12} + 6r_2^2d_{12}^2 - 4r_2d_{12}^3 + d_{12}^4 \\
h &= \sqrt{\frac{-r_1^4 - r_2^4 - d_{12}^4 + r_1^2(2r_2^2 + 2d_{12}^2) + 2d_{12}^2r_2^2}{4d_{12}^2}} \\
h &= \sqrt{\frac{r_2^2(2r_1^2 + 2d_{12}^2 - r_2^2) - (r_1^2 - d_{12}^2)^2}{4d_{12}^2}}. \tag{6.25}
\end{aligned}$$

The volume of a spherical cap needs to be derived. With figure 6.8, one can define

$$\begin{aligned} h^2 &= r^2 - (r - b)^2 = r^2 - r^2 + 2rb - b^2 \\ &= 2rb - b^2 \\ \rightarrow r &= \frac{1}{2} \left(\frac{h^2 + b^2}{b} \right). \end{aligned}$$

This leads to the volume of the spherical cap V_{cap} such as

$$\begin{aligned} V_{\text{cap}} &= \int_0^b \pi h^2 db' \\ &= \int_0^b \pi(2rb' - b'^2) db' \\ &= \pi \left[rb'^2 - \frac{1}{3}b'^3 \right]_0^b \\ &= \pi \left(rb^2 - \frac{1}{3}b^3 \right) \\ V_{\text{cap}} &= \frac{1}{3}\pi(3rb^2 - b^3). \end{aligned} \tag{6.26}$$

Alternatively, one can use the definition of r as given above to get

$$\begin{aligned} V_{\text{cap}} &= \frac{1}{3}\pi \left(3 \frac{1}{2} \left(\frac{h^2 + b^2}{b} \right) b^2 - b^3 \right) \\ &= \frac{1}{3}\pi \left(\frac{3}{2}h^2b + \frac{3}{2}b^3 - b^3 \right) \\ &= \frac{1}{3}\pi \left(\frac{3}{2}h^2b + \frac{1}{2}b^3 \right) \\ V_{\text{cap}} &= \frac{1}{6}b\pi(3h^2 + b^2). \end{aligned} \tag{6.27}$$

The volume of the cap of sphere 1 is

$$V_{1,\text{cap}} = \frac{b_1\pi}{6} (3h^2 + b_1^2)$$

$$\begin{aligned} &= \frac{\frac{r_2^2 - (r_1 - d_{12})^2}{2d_{12}}\pi}{6} \left(3 \frac{r_2^2(2r_1^2 + 2d_{12}^2 - r_2^2) - (r_1^2 - d_{12}^2)^2}{4d_{12}^2} + \left(\frac{r_2^2 - (r_1 - d_{12})^2}{2d_{12}} \right)^2 \right) \\ &= \frac{\frac{r_2^2 - (r_1 - d_{12})^2}{2d_{12}}\pi}{6} \left(3 \frac{2r_1^2r_2^2 + 2r_2^2d_{12}^2 - r_2^4 - r_1^4 + 2r_1^2d_{12}^2 - d_{12}^4}{4d_{12}^2} + \frac{r_2^4 - 2r_2^2(r_1 - d_{12})^2 + (r_1 - d_{12})^4}{4d_{12}^2} \right) \\ &= \frac{(r_2^2 - (r_1 - d_{12})^2)\pi}{48d_{12}^3} (4r_1^2r_2^2 + 4r_2^2d_{12}^2 - 2r_2^4 - 2r_1^4 + 12r_1^2d_{12}^2 + 4r_1(r_2^2d_{12} - r_1^2d_{12} - d_{12}^3)) \\ &= \frac{(r_2^2 - (r_1 - d_{12})^2)\pi}{24d_{12}^3} (-r_1^4 - r_2^4 - d_{12}^4 + 6r_1^2d_{12}^2 + r_2^2(2d_{12}^2 + 2r_1d_{12} + 2r_1^2) - 2r_1^3d_{12} - 2r_1d_{12}^3) \\ &= \frac{\pi}{24d_{12}^3} \times \\ &(-r_1^4r_2^2 - r_2^6 - r_2^2d_{12}^4 + 2r_2^4d_{12}^2 + 2r_2^4r_1d_{12} + 2r_1^2r_2^2 + 6r_1^2r_2^2d_{12}^2 - 2r_1^3r_2^2d_{12} - 2r_1r_2^2d_{12}^3 \\ &+ r_1^6 + r_1^2r_2^4 + r_1^2d_{12}^4 - 2r_1^2r_2^2d_{12}^2 - 2r_1^3r_2^2d_{12} - 2r_1^4r_2^2 - 6r_1^4d_{12}^2 + 2r_1^5d_{12} + 2r_1^3d_{12}^3 \\ &- 2r_1^5d_{12} - 2r_1r_2^4d_{12} - 2r_1d_{12}^5 + 4r_1r_2^2d_{12}^3 + 4r_1^2r_2^2d_{12}^2 + 4r_1^3r_2^2d_{12} + 12r_1^3d_{12}^3 - 4r_1^4d_{12}^2 - 4r_1^2d_{12}^4 \\ &+ r_1^4d_{12}^2 + r_2^4d_{12}^2 + d_{12}^6 - 2r_2^2d_{12}^4 - 2r_1r_2^2d_{12}^3 - 2r_1^2r_2^2d_{12}^2 - 6r_1^2d_{12}^4 + 2r_1^3d_{12}^3 + 2r_1d_{12}^5) \\ &= \frac{\pi \times (r_1^6 - r_2^6 + d_{12}^6 + r_1^4(-3r_2^2 - 9d_{12}^2) + 16r_1^3d_{12}^3 + r_1^2(3r_2^4 + 6r_2^2d_{12}^2 - 9d_{12}^4) + 3r_2^4d_{12}^2 - 3r_2^2d_{12}^4)}{24d_{12}^3}, \end{aligned}$$

while the one for sphere 2 can be calculated with

$$V_{2,\text{cap}} = \frac{b_2\pi}{6} (3h^2 + b_2^2),$$

revealing the same results as for $V_{1,\text{cap}}$, just with interchanged indices 1 and 2

$$= \frac{\pi \times (r_2^6 - r_1^6 + d_{12}^6 + r_2^4(-3r_1^2 - 9d_{12}^2) + 16r_2^3d_{12}^3 + r_2^2(3r_1^4 + 6r_1^2d_{12}^2 - 9d_{12}^4) + 3r_1^4d_{12}^2 - 3r_1^2d_{12}^4)}{24d_{12}^3}.$$

The total overlapping volume is the sum of those two volumes

$$\begin{aligned} V_{\text{total overlap}} &= \frac{\pi \times (2d_{12}^6 - 6r_1^4d_{12}^2 - 6r_2^4d_{12}^2 + 16d_{12}^3(r_1^3 + r_2^3) + 12r_1^2r_2^2d_{12}^2 - 12r_1^2d_{12}^4 - 12r_2^4d_{12}^4)}{24d_{12}^3} \\ &= \frac{\pi \times (d_{12}^4 - 3r_1^4 - 3r_2^4 + 8d_{12}(r_1^3 + r_2^3) + 6r_1^2r_2^2 - 6r_1^2d_{12}^2 - 6r_2^2d_{12}^2)}{12d_{12}} \\ &= \frac{\pi \times (d_{12}^4 - 6d_{12}^2(r_1^2 + r_2^2) + 8d_{12}(r_1^3 + r_2^3) - 3(r_1^2 - r_2^2)^2)}{12d_{12}}. \end{aligned} \quad (6.28)$$

Another approach is based on a grid which is placed inside the unit cell/ primitive cell. An evaluation for each grid point is carried out. Any grid point is either close to an atom (inside its vdW sphere) and can be considered as occupied. If no such occupation is found, the grid point is considered unoccupied. In analogy to equation (6.20), the porosity can be evaluated by the number of unoccupied points over the total number of grid points like

$$\Phi = \frac{N_{\text{unoccupied}}}{N_{\text{total}}}. \quad (6.29)$$

Using a sufficient amount of grid points should provide very accurate results using this ansatz. The results are summarized in table 6.22. Furthermore, by using this ansatz one gains insight into the actual void volume and thus the void porosity. This is not equivalent to the accessible volume and porosity, which is however given in the literature. Thus, one needs to be careful when comparing e.g. the values for DUT-8(Ni)_{closed}. However, one can derive the accessible volume. For this purpose, the grid points are evaluated such that around each grid point a sphere with a 'probe' radius is assumed²¹. If this sphere is in no contact with the vdW surface of the MOF, the point itself is unoccupied or rather accessible. This method gives rise to another quantity, the accessible porosity Φ_{acc} .

Table 6.22.: All relevant informations for the determination of the porosities of all considered MOFs based on a grid (grid). The approximate number of grid points per Å are given as well (grid_{red}). All porosities are given in %. The accessible values are based on a probe radius (r_{probe} , in Å). The accessible porosity Φ_{acc} together with the number of accessible grid points N_{acc} is given as well. The literature values for the porosities are 67 % for DUT-8(Ni)_{open} [26], 0 % for DUT-8(Ni)_{closed} [26], 53 % for UiO-66 [80] and 68 % for UiO-67 [80].

MOF	grid	grid _{red}	N_{total}	N_{occ}	N_{unocc}	N_{acc}	Φ	r_{probe}	Φ_{acc}
DUT-8(Ni) _{open,vc}	...×...×.
DUT-8(Ni) _{open,exp}	55×55×28	3×3×3	84700	25013	59687	53458	70	1.20	63
DUT-8(Ni) _{closed,vc}	70×82×128	10×10×10	734720	574095	160625	0	22	1.20	0
DUT-8(Ni) _{closed,exp}	70×82×128	10×10×10	734720	533025	201695	0	27	1.20	0
UiO-66	60×60×60	4×4×4	216000	88278	127722	110421	59	1.20	51
	60×60×60	4×4×4	216000	88278	127722	86471	59	2.16	40
UiO-67	71×71×71	4×4×4	357911	98948	258963	243141	72	1.20	68
	71×71×71	4×4×4	357911	98948	258963	225092	72	2.16	63

This ansatz has one major disadvantage. It requires much more time than the approach based on overlapping spheres, as can be seen in table 6.23.

It does however provide an accurate ansatz to evaluate the properties and distinguishes between void and accessible porosities. Thus, the derived values give a very good estimate about the porosities and related properties. For example, using the presented ansatz to evaluate the pore volumes, one finds the results as presented in table 6.24.

²¹ In table 6.22, $r_{\text{probe}} = 1.20$ Å corresponds to the vdW radius of H while $r_{\text{probe}} = 2.16$ Å refers to the vdW radius of Xe. The latter has been used for UiO-66 and UiO-67 to gain an insight into the accessible porosity of Xe. This could be important for future studies.

Table 6.23.: Time requirement for the evaluation of the porosity for all considered systems. With the overlapping sphere approach and the grid points ansatz.

MOF	t_{overlap} [s]	r_{probe} [Å]	t_{grid} [s]
DUT-8(Ni) _{open,vc,fix angles}	0.68	...	
DUT-8(Ni) _{open,vc}	0.66
DUT-8(Ni) _{open,exp}	0.65	1.20	617020
DUT-8(Ni) _{closed,vc}	0.17	1.20	3458
DUT-8(Ni) _{closed,exp}	0.17	1.20	3256
UiO-66	0.51	1.20 2.16	58329 115226
UiO-67	1.22	1.20 2.16	151277 838555

Table 6.24.: Evaluated pore volumes for the different ansatzes. A differentiation between void and accessible volume has been carried out for the grid point approach. A comparison to literature values (lit) is given as well.

MOF	$\rho_{\text{pore,overlap}}$ [cm ³ /g]	void/acc	r_{probe} [Å]	$\rho_{\text{pore,grid}}$ [cm ³ /g]	$\rho_{\text{pore,lit}}$ [cm ³ /g]
DUT-8(Ni) _{open,vc}	0.8258		
DUT-8(Ni) _{open,exp}	0.8907	void accessible	1.20 1.20	1.0289 0.9215	1.00 [26]
DUT-8(Ni) _{closed,vc}	—	void accessible	1.20 1.20	0.1209 0.0000	0.00 [26]
DUT-8(Ni) _{closed,exp}	—	void accessible	1.20 1.20	0.1627 0.0000	
UiO-66	0.4123	void accessible void accessible	1.20 1.20 2.16 2.16	0.4939 0.4270 0.4939 0.3344	0.52 [29]
UiO-67	0.9581	void accessible void accessible	1.20 1.20 2.16 2.16	1.0217 0.9593 1.0217 0.8880	0.95 [29]

BIBLIOGRAPHY

- [1] J. P. Perdew, K. Burke, and M. Ernzerhof. Generalized Gradient Approximation Made Simple. *Physical Review Letters*, **77**:3865–3868, 1996.
- [2] S. Grimme. Semiempirical GGA-type Density Functional Constructed with a Long-Range Dispersion Correction. *Journal of Computational Chemistry*, **27**(15):1787–1799, 2006.
- [3] P. Giannozzi, S. Baroni, N. Bonini, M. Calandra, R. Car, C. Cavazzoni, D. Ceresoli, G. L. Chiarotti, M. Cococcioni, I. Dabo, A. Dal Corso, S. de Gironcoli, S. Fabris, G. Fratesi, R. Gebauer, U. Gerstmann, C. Gougoussis, A. Kokalj, M. Lazzeri, L. Martin-Samos, N. Marzari, F. Mauri, R. Mazzarello, S. Paolini, A. Pasquarello, L. Paulatto, C. Sbraccia, S. Scandolo, G. Sclauzero, A. P. Seitsonen, A. Smogunov, P. Umari, and R. M. Wentzcovitch. QUANTUM ESPRESSO: a modular and open-source software project for quantum simulations of materials. *Journal of Physics: Condensed Matter*, **21**(39):395502 (19pp.), 2009.
- [4] K. Koepnik and H. Eschrig. Full-potential nonorthogonal local-orbital minimum-basis band-structure scheme. *Physical Review B*, **59**:1743–1757, 1999.
- [5] B. F. Hoskins and R. Robson. Infinite polymeric frameworks consisting of three dimensionally linked rod-like segments. *Journal of the American Chemical Society*, **111**(15):5962–5964, 1989.
- [6] H. K. Chae, D. Y. Siberio-Perez, J. Kim, Y. Go, M. Eddaoudi, A. J. Matzger, M. O’Keeffe, and O. M. Yaghi. A route to high surface area, porosity and inclusion of large molecules in crystals. *Nature*, **427**:523–527, 2003.
- [7] S. L. James. Metal-organic frameworks. *Chemical Society Review*, **32**:276–288, 2003.
- [8] H. Furukawa, N. Ko, Y. B. Go, N. Aratani, S. B. Choi, E. Choi, A. Ö. Yazaydin, R. Q. Snurr, M. O’Keeffe, and O. M. Yaghi. Ultra-high Porosity in Metal-Organic Frameworks. *Science*, **329**:424–428, 2010.
- [9] H. Deng, S. Grunder, K. E. Cordova, C. Valenta, H. Furukawa, M. Hmadeh, F. Gándara, A. C. Whalley, Z. Liu, S. Asahina, H. Kazumori, M. O’Keeffe, O. Terasaki, J. F. Stoddart, and O. M. Yaghi. Large-Pore Apertures in a Series of Metal-Organic Frameworks. *Science*, **336**(6084):1018–1023, 2012.
- [10] R. E. Morris and P. S. Wheatley. Gas storage in Porous Media. *Angewandte Chemie International Edition*, **47**:4966–4981, 2008.
- [11] J.-R. Li, R. J. Kuppler, and H.-C. Zhou. Selective gas adsorption and separation in metal-organic frameworks. *Chemical Society Reviews*, **38**:1477–1504, 2009.
- [12] K. Treppe, S. Schwalbe, and G. Seifert. Electronic and magnetic properties of DUT-8(Ni). *Physical Chemistry Chemical Physics*, **17**:17122 – 17129, 2015.
- [13] S. Schwalbe, K. Treppe, G. Seifert, and J. Kortus. Screening for high-spin metal organic frameworks (MOFs): density functional theory study on DUT-8(M₁,M₂) (with M_i = V,...,Cu). *Physical Chemistry Chemical Physics*, **18**:8075 – 8080, 2016.

- [14] A. Worsztynowicz, S. M. Kaczmarek, M. Bosacka, V. Mody, and R. S. Czer-nuszewicz. Structural and magnetic characterization of the Cr^{3+} and Ni^{2+} ion species in $\text{Ni}_2\text{CrV}_3\text{O}_{11}$. *Reviews on advanced material science*, **14**:24–32, 2007.
- [15] U. Kortz, Y. P. Jeannin, A. Teze, G. Herve, and S. Isber. A novel dimeric Ni-substituted β -Keggin silicotungstate: Structure and magnetic properties of $\text{K}_{12}[\beta\text{-SiNi}_2\text{W}_{10}\text{O}_{36}(\text{OH})_2(\text{H}_2\text{O})_2] \cdot 20 \text{H}_2\text{O}$. *Inorganic Chemistry*, **38**(16):3670–3675, 1999.
- [16] C. Martin. *Density functional studies of the electronic and magnetic properties of selected transition metal complexes*. PhD thesis, Technische Universität Freiberg, 2013.
- [17] O. Kahn. *Molecular magnetism*. Wiley, 1993.
- [18] A. K. Rajagopal and J. Callaway. Inhomogeneous Electron Gas. *Physical Review B*, **7**:1912–1919, 1973.
- [19] W. Bieger, G. Seifert, H. Eschrig, and G. Grossmann. LCAO $X\alpha$ calculations of nuclear magnetic shielding in molecules. *Chemical Physics Letters*, **115**:275–280, 1985.
- [20] T. Heine, C. Corminboeuf, and G. Seifert. The Magnetic Shielding Function of Molecules and Pi-Electron Delocalization. *Chemical Reviews*, **105**:3889–3910, 2005.
- [21] K. Trepte, J. Schaber, S. Schwalbe, F. Drache, I. Senkovska, S. Kaskel, J. Kortus, E. Brunner, and G. Seifert. The origin of the measured chemical shift of ^{129}Xe in UiO-66 and UiO-67 revealed by DFT investigations. *Physical Chemistry Chemical Physics*, **19**:10020–10027, 2017.
- [22] P. Hohenberg and W. Kohn. Inhomogeneous Electron Gas. *Physical Review*, **136**:B864–B871, 1964.
- [23] W. Kohn and L. J. Sham. Self-Consistent Equations Including Exchange and Correlation Effects. *Physical Review*, **140**:A1133–A1138, 1965.
- [24] N. Klein, C. Herzog, M. Sabo, I. Senkovska, J. Getzschmann, S. Paasch, M. R. Lohe, E. Brunner, and S. Kaskel. Monitoring adsorption-induced switching by ^{129}Xe NMR spectroscopy in a new metal-organic framework $\text{Ni}_2(2,6\text{-ndc})_2(\text{dabco})$. *Physical Chemistry Chemical Physics*, **12**:11778–11784, 2010.
- [25] H. C. Hoffmann, B. Assfour, F. Epperlein, N. Klein, S. Paasch, I. Senkovska, S. Kaskel, G. Seifert, and E. Brunner. High-Pressure in Situ ^{129}Xe NMR Spectroscopy and Computer Simulations of Breathing Transitions in the Metal-Organic Framework $\text{Ni}_2(2,6\text{-ndc})_2(\text{dabco})$ (DUT-8(Ni)). *Journal of the American Chemical Society*, **133**(22):8681–8690, 2011.
- [26] V. Bon, N. Klein, I. Senkovska, A. Heerwig, J. Getzschmann, D. Wallacher, I. Zizak, M. Brzhezinskaya, U. Mueller, and S. Kaskel. Exceptional adsorption-induced cluster and network deformation in the flexible metal-organic framework DUT-8(Ni) observed by in situ X-ray diffraction and EXAFS. *Physical Chemistry Chemical Physics*, **17**:17471–17479, 2015.

- [27] G. Férey and C. Serre. Large breathing effects in three-dimensional porous hybrid matter: facts, analyses, rules and consequences. *Chemical Society Reviews*, **38**:1380–1399, 2009.
- [28] J. H. Cavka, S. Jakobsen, U. Olsbye, N. Guillou, C. Lamberti, S. Bordiga, and K. P. Lillerud. A New Zirconium Inorganic Building Brick Forming Metal Organic Frameworks with Exceptional Stability. *Journal of the American Chemical Society*, **130**:13850–13851, 2008.
- [29] S. Chavan, J. G. Vitillo, D. Gianolio, O. Zavorotynska, B. Civalleri, S. Jakobsen, M. H. Nilsen, L. Valenzano, C. Lamberti, K. P. Lillerud, and S. Bordiga. H₂ storage in isostructural UiO-67 and UiO-66 MOFs. *Physical Chemistry Chemical Physics*, **14**:1614–1626, 2012.
- [30] Q. Yang, V. Guillerm, F. Ragon, A. D. Wiersum, P. L. Llewellyn, C. Zhong, T. Devic, C. Serre, and G. Maurin. CH₄ storage and CO₂ capture in highly porous zirconium oxide based metal-organic frameworks. *Chemical Communications*, **48**:9831–9833, 2012.
- [31] E. Schrödinger. Quantisierung als Eigenwertproblem. *Annalen der Physik*, **384**(4):361–376, 1926.
- [32] M. Born and R. Oppenheimer. Zur Quantentheorie der Molekeln. *Annalen der Physik*, **389**(20):457–484, 1927.
- [33] R. Martin. *Electronic structure - basic theory and practical methods*. Cambridge University Press, Cambridge, UK, 2004.
- [34] J. R. Yates, C. J. Pickard, and D. Ceresoli. First principles calculation of Solid-State NMR parameters. *Psi-k newsletter 102*, pages 42–63, 2010.
- [35] T. Fließbach. *Elektrodynamik, 4. Auflage*. Springer, 2012.
- [36] W. E. Lamb. Internal Diamagnetic Fields. *Physical Review*, **60**:817–819, 1941.
- [37] N. F. Ramsey. Magnetic Shielding of Nuclei in Molecules. *Physical Review*, **78**:699–703, 1950.
- [38] T. A. Keith and R. F. W. Bader. Properties of atoms in molecules: nuclear magnetic shielding. *Canadian Journal of Chemistry*, **74**(2):185–200, 1996.
- [39] J. P. Perdew and K. Burke. Comparison Shopping for a Gradient-Corrected Density Functional. *International Journal of Quantum Chemistry*, **57**:309–319, 1996.
- [40] O. K. Andersen. Linear methods in band theory. *Physical Review B*, **12**:3060–3083, 1975.
- [41] J. C. Slater. Atomic shielding constants. *Physical Review*, **36**:57–64, 1930.
- [42] S. F. Boys. Electronic wave functions. 1. a general method of calculation for the stationary states of any molecular system. *Proceedings of the Royal Society London A: Mathematical, Physical and Engineering Sciences*, **200**:542–554, 1950.

- [43] F. Bloch. Über die Quantenmechanik der Elektronen in Kristallgittern. *Zeitschrift für Physik*, **52**(7-8):555–600, 1929.
- [44] C. Herring. A New Method for Calculating Wave Functions in Crystals. *Physical Review*, **57**:1169–1177, 1940.
- [45] J. C. Slater. An Augmented Plane Wave Method for the Periodic Potential Problem. *Physical Review*, **92**:603–608, 1953.
- [46] J. C. Phillips and L. Kleinman. New Method for Calculating Wave Functions in Crystals and Molecules. *Physical Review*, **116**:287–294, 1959.
- [47] G. B. Bachelet, D. R. Hamann, and M. Schlüter. Pseudopotentials that work: From H to Pu. *Physical Review B*, **26**:4199–4228, 1982.
- [48] D. R. Hamann, M. Schlüter, and C. Chiang. Norm-Conserving Pseudopotentials. *Physical Review Letters*, **43**:1494–1497, 1979.
- [49] P. E. Blöchl. Projector augmented-wave method. *Physical Review B*, **50**:17953–17979, 1994.
- [50] C. J. Pickard and F. Mauri. All-electron response with pseudopotentials: NMR chemical shifts. *Physical Review B*, **63**:245101 (13 pp.), 2001.
- [51] R. Ditchfield. Molecular Orbital Theory of Magnetic Shielding and Magnetic Susceptibility. *The Journal of Chemical Physics*, **56**:5688–5691, 1972.
- [52] W. Kutzelnigg, U. Fleischer, and M. Schindler. *The IGLO-Method: Ab-initio Calculation and Interpretation of NMR Chemical Shifts and Magnetic Susceptibilities*, volume **213**, pp. 165–262. Springer Verlag, Berlin/Heidelberg, 1991.
- [53] W. Heisenberg. Mehrkörperproblem und Resonanz in der Quantenmechanik. *Zeitschrift für Physik*, **38**(6-7):411–426, 1926.
- [54] P. A. M. Dirac. On the Theory of Quantum Mechanics. *Proceedings of the Royal Society of London A: Mathematical, Physical and Engineering Sciences*, **112**(762):661–677, 1926.
- [55] J. H. Van Vleck. *The theory of electric and magnetic susceptibilities*. Oxford: Clarendon Press, 1932.
- [56] P. W. Anderson. Antiferromagnetism. Theory of Superexchange Interaction. *Physical Review*, **79**:350–356, 1950.
- [57] C. Zener. Interactions between the *d*-Shells in the Transition Metals. II. Ferromagnetic Compounds of Manganese with Perovskite Structure. *Physical Review*, **82**:403–405, 1951.
- [58] F. Hund. Zur Deutung einiger Erscheinungen in den Molekelspektren. *Zeitschrift für Physik*, **36**(9):657–674, 1926.
- [59] T. Ito and J. Fraissard. ^{129}Xe NMR study of xenon absorbed on Y zeolites. *Journal of Chemical Physics*, **76**:5225–5229, 1982.

- [60] I. Opahle, K. Koepernik, and H. Eschrig. Full-potential band-structure calculation of iron pyrite. *Physical Review B*, **60**:14035–14041, 1999.
- [61] J. M. Soler, E. Artacho, J. D. Gale, A. García, J. Junquera, P. Ordejón, and D. Sánchez-Portal. The Siesta method for ab initio order-N materials simulation. *Journal of Physics: Condensed Matter*, **14**:2745–2779, 2002.
- [62] A. Kokalj. XCrySDen—a new program for displaying crystalline structures and electron densities. *Journal of Molecular Graphics and Modelling*, **17**(3–4):176–179, 1999.
- [63] E. Kokot and R. L. Martin. Magnetic studies with Copper(II) Salts. VI. Variable singlet-triplet energies in amine-substituted Copper(II) Alkanoates. *Inorganic Chemistry*, **3**(9):1306–1312, 1964.
- [64] S. Devautour-Vinot, G. Maurin, C. Serre, P. Horcajada, D. P. da Cunha, V. Guillerm, E. de Souza Costa, F. Taulelle, and C. Martineau. Structure and Dynamics of the Functionalized MOF Type UiO-66(Zr): NMR and Dielectric Relaxation Spectroscopies Coupled with DFT Calculations. *Chemistry of Materials*, **24**:2168–2177, 2012.
- [65] M. C. Lawrence, C. Schneider, and M. J. Katz. Determining the structural stability of UiO-67 with respect to time: a solid-state NMR investigation. *Chemical Communications*, **52**:4971–4974, 2016.
- [66] M. A. M. Forgeron, R. E. Wasylshen, and G. H. Penner. Investigation of Magnetic Shielding in Xenon Difluoride Using Solid-State NMR Spectroscopy and Relativistic Density Functional Theory. *Journal of Physical Chemistry A*, **108**:4751–4758, 2004.
- [67] C. Chang, M. Pelissier, and P. Durand. Regular Two-Component Pauli-Like Effective Hamiltonians in Dirac Theory. *Physica Scripta*, **34**:394–404, 1986.
- [68] J.-L. Heully, I. Lindgren, E. Lindroth, and A.-M. Mårtensson-Pendrill. Comment on relativistic wave equations and negative-energy states. *Physical Review A*, **33**:4426–4429, 1986.
- [69] E. van Lenthe, E. J. Baerends, and J. G. Snijders. Relativistic regular two-component Hamiltonians. *Journal of Chemical Physics*, **99**:4597–4610, 1993.
- [70] S. Faas, J. G. Snijders, J. H. van Lenthe, E. van Lenthe, and E. J. Baerends. The ZORA formalism applied to the Dirac-Fock equation. *Chemical Physics Letters*, **246**:632–640, 1995.
- [71] T. Meersmann and E. Brunner. *Hyperpolarized Xenon-129 Magnetic Resonance: Concepts, Production, Techniques and Applications*. The Royal Society of Chemistry, Thomas Graham House, Science Park, Milton Road, Cambridge CB4 0WF, UK, 2015.
- [72] C. Lu, T. Carlson, F. Malik, T. Tucker, and C. Nestor. Relativistic Hartree-Fock-Slater eigenvalues, radial expectation values, and potentials for atoms, $2 \leq Z \leq 126$. *Atomic Data and Nuclear Data Tables*, **3**:1–131, 1971.
- [73] A. Bondi. van der Waals Volumes and Radii. *The Journal of Physical Chemistry*, **68**:441–451, 1964.

- [74] N. Metropolis and S. Ulam. The Monte Carlo method. *Journal of the American Statistical Association*, **44**:335–341, 1949.
- [75] N. Metropolis, A. W. Rosenbluth, M. N. Rosenbluth, A. H. Teller, and E. Teller. Equation of State Calculations by Fast Computing Machines. *Journal of Chemical Physics*, **21**:1087–1092, 1953.
- [76] W. K. Hastings. Monte Carlo Sampling Methods Using Markov Chains and Their Applications. *Biometrika*, **57**:97–109, 1970.
- [77] R. G. Della Valle and E. Venuti. Quasiharmonic lattice-dynamics and molecular-dynamics calculations for the Lennard-Jones solids. *Physical Review B*, **58**:206–212, 1998.
- [78] G. Merino, T. Heine, and G. Seifert. The Induced Magnetic Field in Cyclic Molecules. *Chemistry: A European Journal*, **10**:4367–4371, 2004.
- [79] S. Blundell. *Magnetism in Condensed Matter*. Oxford University Press, 2001.
- [80] H. Wu, T. Yildirim, and W. Zhou. Exceptional Mechanical Stability of Highly Porous Zirconium Metal-Organic Framework UiO-66 and Its Important Implications. *The Journal of Physical Chemistry Letters*, **4**:925–930, 2013.

ACKNOWLEDGEMENT

There are heaps of people who deserve to be thanked at this point. I hope I do not forget anyone. If I do, please do not feel neglected :)

- The first thanks goes to Prof. Gotthard Seifert, who enabled me to work on this thesis and supported me in everything I did. Additionally, I am very grateful for all the discussions we had.
- Further thanks goes to all the members of the theoretical chemistry group in Dresden for great discussions and brainstroms.
 - In specific, thanks goes to Igor Baburin, because he always had time to talk and the greateast ideas at hand, not only but mostly about symmetries.
 - Further, Jan-Ole Joswig for great support and the introduction of interesting teaching duties.
 - Additional thanks goes to Jens Kunstmann, because it was great to work with him. It taught me a lot.
 - Furthermore, thanks goes to Florian Günther, who had deep insights into physics and did not hesitate to share them.
 - Thanks goes to David Teich for heaps of useful discussions and ideas.
 - In addition, thanks goes to Tommy Lorenz, because he is quite brilliant.
 - Thanks goes to Knut Vietze for all the technical support and great discussions.
 - And Antje Völkel for all the organization.
- Of course, further thanks belongs to the group of theoretical physics in Freiberg for cooperation and much more.
 - First and foremost Prof. Jens Kortus, especially for enabling us to create a very fruitful cooperation between Freiberg and Dresden. Furthermore, the discussion we had in Freiberg were always very interesting. And additional thanks is given due to the fact that I had the pleasure to write my master thesis under his supervision.
 - Biggest thanks goes to Sebastian Schwalbe for everything we have done, discussed, analyzed, achieved, learned, thought about and simply everything else. This was awesome.
 - Another thanks goes to the supervisor of my master thesis, Claudia Martin, for the greatest support I could possibly imagine for the thesis and for everything I learned from her.
 - And Simon Liebing, just because.

- I'd like to thank Prof. Eike Brunner for an amazing cooperation with an experimental group. The discussions with him and his group were very insightful.
- Thanks goes to Volodymyr Bon (in the group of Prof. Kaskel) for providing the initial structures of DUT-8(Ni) as well as for interesting discussion regarding this structure.
- Further thanks goes to the ZIH in Dresden for computational time and an excellent support.

I think this is end the of the list of thanks within the scientific area. But there are way more people to thank.

- My mother Heike, who always believed in me and supported me in every respect.
- My father Volkmar, who always put a lot of interest into my work. The resulting discussions were very interesting.
- My brother Paul, who is one of the most important persons in my life.
- My sister Claudia, who is awesome!
- Additionally my siblings Johnatan, Charlotte, Rebekka and Franziska, who I had the pleasure to meet and get to know.
- My step father Friedrich, who always had an open mind and put lots of interest into my thesis.
- My best friend Robert, for everything we have been through and for everything there is to come.
- Annett und Wolfgang for being great friends and a 'secondary' family for me. That is highly appreciated.
- My friends Sebastian Borrman and Martin Polednia for being great.
- My grandmothers Marianne and Ilse for being the greatest grandmothers ever.
- The most special thanks goes to my grandfather Hans-Ullrich, for being my biggest idol in so many ways, especially in being a theoretical physicist.

Declaration according to Doctorate Regulations §5 para. 1 no. 5a)

I herewith declare that I have produced this paper without the prohibited assistance of third parties and without making use of aids other than those specified; notions taken over directly or indirectly from other sources have been identified as such. This paper has not previously been presented in identical or similar form to any other German or foreign examination board.

Declaration according to Doctorate Regulations §5 para. 1 no. 5b)

This dissertation has been produced at the Technische Universität Dresden (Faculty of Mathematics and Natural Sciences, Institute for Physical Chemistry, Chair of Theoretical Chemistry) under the supervision of Prof. Dr. rer. nat. habil. Gotthard Seifert.

Erklärung gemäß Promotionsordnung § 5 Absatz (1) Punkt 5 a)

Hiermit versichere ich, dass ich die vorliegende Arbeit ohne unzulässige Hilfe Dritter und ohne Benutzung anderer als der angegebenen Hilfsmittel angefertigt habe; die aus fremden Quellen direkt oder indirekt übernommenen Gedanken sind als solche kenntlich gemacht. Die Arbeit wurde bisher weder im Inland noch im Ausland noch im Ausland in gleicher oder ähnlicher Form einer anderen Prüfungsbehörde vorgelegt.

Erklärung gemäß Promotionsordnung § 5 Absatz (1) Punkt 5 b)

Die Dissertation wurde an der Technischen Universität Dresden (Fakultät für Mathematik und Naturwissenschaften, Institut für Physikalische Chemie, Professur für Theoretische Chemie) unter Anleitung von Prof. Dr. rer. nat. habil. Gotthard Seifert angefertigt.

Dresden,